

---

# Application of the chiral forces to electroweak processes

---

Vitalii Urbanevych

Ph.D. thesis written under the supervision of dr. hab Roman Skibiński  
at the Jagiellonian University, Faculty of Physics, Astronomy  
and Applied Computer Science, Kraków,  
Thursday 4<sup>th</sup> May, 2023



---

# CONTENTS

|          |   |           |
|----------|---|-----------|
| <b>1</b> | <b>Introduction</b>   | <b>1</b>  |
| <b>2</b> | <b>Formalism &amp; numerical methods</b>                        | <b>9</b>  |
| 2.1      | Deuteron bound state . . . . .                                  | 9         |
| 2.2      | 2N scattering state . . . . .                                   | 12        |
| 2.2.1    | The Lippmann-Schwinger equation . . . . .                       | 12        |
| 2.3      | 3N bound state . . . . .  | 15        |
| 2.4      | 3N scattering state . . . . .                                   | 16        |
| 2.5      | Photodisintegration transition amplitude for Nd state . . . . . | 17        |
| 2.6      | Nuclear electromagnetic current . . . . .                       | 18        |
| 2.7      | Theoretical uncertainties . . . . .                             | 18        |
| <b>3</b> | <b>Results</b>  | <b>22</b> |
| 3.1      | Deuteron photodisintegration . . . . .                          | 22        |
| 3.1.1    | Cross section . . . . .   | 22        |
| 3.1.2    | Polarisation observables . . . . .                              | 29        |
| 3.2      | Helium photodisintegration . . . . .                            | 46        |
| 3.2.1    | 3N photodisintegration . . . . .                                | 46        |
| 3.2.2    | D-p photodisintegration . . . . .                               | 54        |
| 3.3      | Triton photodisintegration . . . . .                            | 55        |
| 3.4      | Pion absorption from the lowest atomic orbital . . . . .        | 59        |
| 3.4.1    | Pion absorption in $^3\text{He}$ . . . . .                      | 59        |
| 3.4.2    | $\pi^- + ^3\text{H} \rightarrow n + n + n$ . . . . .            | 70        |
|          | <b>Bibliography</b>   | <b>76</b> |

## **Abstract**

Lorem ipsum dolor sit amet, consectetur adipiscing elit, sed do eiusmod tempor incididunt ut labore et dolore magna aliqua. Ut enim ad minim veniam, quis nostrud exercitation ullamco laboris nisi ut aliquip ex ea commodo consequat. Duis aute irure dolor in reprehenderit in voluptate velit esse cillum dolore eu fugiat nulla pariatur. Excepteur sint occaecat cupidatat non proident, sunt in culpa qui officia deserunt mollit anim id est laborum.

---

# CHAPTER 1

---

## INTRODUCTION

### Why we study few nucleon systems

The study of light nuclei and their reactions has been serving as an easy way to investigate particles in nuclei and the forces between them for decades. A convenient way to proceed may be to study the interaction of a nucleus with other nuclei, particles, or electromagnetic probes such as electrons, photons, muons, pions, neutrinos, and hyperons. In most cases, the study of elastic or inelastic scattering is possible. This can be done either theoretically or by performing relevant experiments to test if the theory works. It should be taken into account that nuclear interactions may be caused by different fundamental forces and therefore described in different ways, including strong, weak, or electromagnetic interactions. This depends on the type of particle being scattered and the target of the reaction. Of course gravitational force also is in the game but due to the weakness can be omitted in the nuclear physics.

In the past many experimental efforts have been undertaken and experimentalists have been interested in electromagnetic reactions in light nuclei for decades. There are experimental data from the second half of 20th century (e.g. [1–4]) which are still useful for comparing theoretical predictions with experimental measurements. There are several facilities that provide sources of gamma rays (both low- and high-energy) and other particles that have been operating for decades and still enable experiments to be conducted. Let us mention here some facilities as TUNL with HI $\gamma$ S [5, 6], MAMI [7], NIKHEF [8] and others.

To accurately describe nuclear reactions, multiple components of the Hamiltonian must be considered. The most important are nucleon interactions and nuclear currents. First of all, various nuclear forces may act on the particles.

The strong nuclear force acts inside the nuclei and, among others, bound neutrons and protons together. The description of strong interactions is extremely difficult as it deals not only with the nucleons themselves, but also with their constituents: quarks and gluons. Quantum chromodynamics (QCD) is a modern theory describing strong interactions, but, at the moment, it is not applicable at low energies ( $Q^2 \lesssim 1\text{GeV}^2$ ). In such situation various approaches are emerging. The most advanced are the chiral effective theory and lattice calculation [9–11]. In this work we will use results of the first approach.

Study of three- (and more) nucleon systems showed that the strong 2N force is not

enough to describe the system, and a 3N force was introduced. The first applications of such a force showed that it brings a sufficient contribution and cannot be ignored [12]. The contribution of the 3NF can be examined by comparing binding energies of light nuclei calculated with and without this part with respect to experimental values.

For example, the binding energy for  ${}^3\text{H}$  calculated with the Argonne V18 (AV18) potential without 3NF amounts to  $E_b({}^3\text{H}) = -7.628 \text{ MeV}$  [13]. There are different models that might add a 3NF contribution to AV18 (or other potentials). Using the Tucson-Melbourne (TM) model [14] results in  $E_b({}^3\text{H}) = -8.478 \text{ MeV}$ , and Urbana IX [15] 3NF provides us with  $E_b({}^3\text{H}) = -8.484 \text{ MeV}$ . Looking at the experimental value  $E_b({}^3\text{H}) = -8.482 \text{ MeV}$ , it is clear that the 3NF contribution makes the prediction much closer to the measurement. Nevertheless, parameters of the UrbanaIX 3NF in this case were fitted to the experimental value for  ${}^3\text{H}$ , so there is no surprise in good agreement.

One can check the binding energy for other atoms, which were not used for fitting. The 2NF binding energy for  ${}^3\text{He}$  (calculated with AV18) is  $E_b({}^3\text{He}) = -6.917 \text{ MeV}$ . TM contribution makes it  $E_b({}^3\text{He}) = -7.706 \text{ MeV}$ , Urbana IX gives  $E_b({}^3\text{He}) = -7.739 \text{ MeV}$ , while the experimental value is  $E_b({}^3\text{He}) = -7.718 \text{ MeV}$ . Once more, we can see the importance of 3NF contribution on the  $\alpha$ -particle's ( ${}^4\text{He}$ ) binding energy: pure AV18 gives  $E_b({}^4\text{He}) = -24.25 \text{ MeV}$ , AV18 + TM gives  $-28.84 \text{ MeV}$ , AV18 + Urbana IX gives  $-28.50 \text{ MeV}$ , and the experimental value is  $-28.30 \text{ MeV}$ .

Whereas the first applications included only early simplified "realistic" 3N potential, the latter investigations, based on more advanced models, fully confirmed this statements [16, 17]. Within new models the four-nucleon (4N) bound state was constructed to compare description of  ${}^3\text{He}$  [18].

Electromagnetic force appears between charged particles like protons, electrons or pions. Also, the force is transferred between charged particles and a photon, so in photon- and electron- scatterings on the nuclei an electromagnetic force is necessary component of a description.

Arenh"ovel's study [19] used different theoretical models, including a nonrelativistic potential model, a relativistic impulse approximation, and a relativistic meson-exchange model, to describe the deuteron photodisintegration process. These models were used to calculate the differential cross section, which describes the probability of the process occurring at different scattering angles and photon energies.

The calculated cross sections were then compared to experimental data, and it was found that the relativistic meson-exchange model provided the best agreement with the data. This model includes the exchange of virtual mesons between the interacting particles, which accounts for the strong and electromagnetic forces between them.

Overall, Arenh"ovel's study demonstrated the importance of including both strong and electromagnetic forces in a description of the deuteron photodisintegration process, and highlighted the need for accurate theoretical models to interpret experimental data.

The weak force is of great importance in the study of nuclear processes. One of the main roles of the weak force is to mediate beta decay, which is a process in which a neutron in a nucleus is converted into a proton, emitting an electron and an antineutrino. This process plays a crucial role in the formation of elements in the universe, as it allows for the conversion of neutron-rich isotopes into more stable, proton-rich isotopes. Additionally, the weak force plays a role in neutrino interactions with matter, which are of great interest in both astrophysics and particle physics. In nuclear physics, weak interactions can also play a role in the decay of unstable nuclei, the production of neutrinos in nuclear reactions, and the scattering of neutrinos off nuclei. The study of weak interactions is

therefore an essential component of the overall understanding of nuclear physics and the behavior of matter on the subatomic scale.

## Models of strong interaction used in the thesis

In order to model the nuclear potential, physicists often use phenomenological or semi-phenomenological approaches. It allows them to combine theoretical knowledge about processes and experimental findings.

Among many of such models, the Argonne V18 (AV18) [17] force is one of most advanced and therefore is used in current thesis. In order to construct nucleon-nucleon (NN) force, authors combine one-pion-exchange parts with phenomenological one and supplement them by electromagnetic corrections. Free parameters were fitted to the Nijmegen partial-wave analysis of  $pp$  and  $np$  data [20]. Authors showed, that AV18 potential delivers good results in the description of nucleon scattering data ( $\chi^2/data = 1.08$  for around 4000  $pp$  and  $np$  scattering datasets) as well as deuteron properties (estimated binding energy is 2.2247(35) MeV vs experimental 2.224 575(9) MeV).

Weinberg's idea of using chiral symmetry to describe nuclear interactions at low energies was first introduced in his papers published in 1990 and 1991 [21, 22]. In these papers, Weinberg argued that the low-energy dynamics of nucleons could be described using a chiral Lagrangian, which is the most general Lagrangian consistent with chiral symmetry and its spontaneous breaking. This Lagrangian is expressed in terms of nucleon and pion fields, which are the degrees of freedom that become relevant at low energies.

The chiral Lagrangian is the starting point for the development of the Chiral Effective Field Theory ( $\chi$ EFT), which has become one of the most advanced approaches to low-energy nuclear physics. The use of  $\chi$ EFT allows for the calculation of nuclear properties and reactions in a model-independent way, making it possible to quantify the uncertainties associated with the calculation. One of the key features of  $\chi$ EFT is that it allows for the construction of a nuclear potential, which can then be used in relevant formalisms, e.g. to solve the Schrödinger equation and to obtain bound state properties. The accuracy of the potential can be systematically improved by including higher-order terms in the chiral expansion, which leads to a better description of experimental data.

In the  $\chi$ EFT there are two natural scales: so-called soft scale  $Q \sim M_\pi$  - the mass of pion and the hard scale -  $\Lambda_\chi \sim 0.7 \text{ GeV}$  - the chiral symmetry breaking scale. The ratio between these two scales  $Q/\Lambda_\chi$  is being used as an expansion parameter in  $\chi$ EFT with power  $\nu$ :  $(Q/\Lambda_\chi)^\nu$ .<sup>1</sup>

Possibility of deriving nuclear potential is an important feature of  $\chi$ EFT. The potential, as occurs in an Lagrangian, is a perturbation expression of the same parameter  $Q/\Lambda_\chi$ . Considering so-called irreducible diagrams (which cannot be split by cutting nucleon lines), Weinberg [21, 22] came to the expression for the powers  $\nu_W$  of such diagrams

$$\nu_W = 4 - A - 2C + 2L + \sum_i \Delta_i, \quad (1.1)$$

where  $i$  specifies a vertex number and

$$\Delta_i \equiv d_i + \frac{n_i}{2} - 2. \quad (1.2)$$

---

<sup>1</sup>Note that exact values of some parameters are still under discussion [23]. We follow here approach described by E.Epelbaum and collaborators, see e.g. [24]

In Eq. (1.1)  $C$  is a number of pieces which are connected,  $L$  - the number of loops in the graph and  $A$  is a number of nucleons in the diagram. In Eq. (1.2)  $n_i$  is a number of nucleon field operators and  $d_i$  - the number of insertions (or derivatives) of  $M_\pi$ .

The further analysis of Eq. (1.1) revealed some problems which occur for particular values of parameters in the equation, namely negative values of  $\nu_W$  are possible while the order has to take integer values from 0 to infinity. In order to deal with that, Eq. (1.1) was slightly modified adding  $3A - 6$  to it [11, 25]:

$$\nu = \nu_W + 3A - 6 = -2 + 2A - 2C + 2L + \sum_i \Delta_i \quad (1.3)$$

That convention is widely used and we will also stick to it. In  $\chi$ EFT the first order, "leading order" (LO,  $\nu = 0$ ) is followed by next-to-leading order (NLO,  $\nu = 2$ )<sup>2</sup>, next-to-next-to-leading order (next-to-next-to-leading order (N<sup>2</sup>LO),  $\nu = 3$ ) and so on. At each chiral order, new interaction diagrams complete the potential. There are also two diagrams at leading order (LO). One is a diagram which consists of 2 contact terms and the other one is one-pion exchange, see Fig. 1.1. Both diagrams reflect only 2NF. The same is for diagrams at next-to-leading order (NLO), where more contact terms occur together with two-pion exchange topologies. Each subsequent order includes more and more sophisticated diagrams describing nucleons interaction via multiple pion exchanges and various contact vertices. 3NF appears for the first time at N<sup>2</sup>LO while 4NF contributions are occurring from next-to-next-to-next-to-leading order (N<sup>3</sup>LO). This scheme establishes for the first time a systematic way to include all the forces from the simplest diagrams at LO and gradually adding more and more terms. It is also beneficial in the way that one can obtain results using chiral potential at different orders and track which one gives large or small contribution to the final prediction. At the moment, next-to-next-to-next-to-next-to-leading order (N<sup>4</sup>LO) is the highest order at which 2N interaction has been derived. Nevertheless leading F-wave contact interactions from N<sup>5</sup>LO have been combined with N<sup>4</sup>LO force leading to the N<sup>4</sup>LO<sup>+</sup> potential, which is currently regarded as a best available potential on the market. The progression of the chiral orders is reflected in a  $\chi^2/datum$ . Leading order results in  $\chi^2/datum = 73$  (with neutron-proton data with  $E_{lab} = 0 - 100\text{MeV}$ ). Each subsequent order has better and better results: NLO gives  $\chi^2/datum = 2.2$ , N<sup>2</sup>LO -  $\chi^2/datum = 2.2$  and the final N<sup>4</sup>LO<sup>+</sup> leads to  $\chi^2/datum = 1.08$  [24]. Similar progress is observed for wider energy range, e.g for  $E_{lab} = 0 - 300\text{MeV}$   $\chi^2/datum$  is 75, 14, 4.2, 2.01, 1.16 and 1.06 at LO, NLO, N<sup>2</sup>LO, N<sup>3</sup>LO, N<sup>4</sup>LO and N<sup>4</sup>LO<sup>+</sup>, respectively. The proton-proton data description has similar trend, so  $\chi^2/datum$  is 1380, 91, 41, 3.43, 1.67, 1.00 for the same energy bin and chiral orders. At N<sup>4</sup>LO<sup>+</sup>  $\chi^2/datum$  for proton-proton data stands similar value (close to 1) as for neutron-proton, but the convergence comes a bit later and leading order has way worse description. In my work I will use chiral potentials from LO to N<sup>4</sup>LO<sup>+</sup>.

The Argonne V18 potential [17], mentioned earlier, has 18 free parameters, while  $\chi$ EFT NN potential at N<sup>4</sup>LO [11] has only three low-energy constants (LECs) fitted to deuteron properties. The reduction of the number of free parameters of the  $\chi$ EFT-based potentials has not only a theoretical but also a practical advantage in the studies of the many-body nuclear systems.

The general scheme outlined above was developed mainly by the Bochum-Bonn and Moscow-Idaho groups. Both groups have similar approaches and were independently and

---

<sup>2</sup>The contributions to the potential at order  $\nu = 1$  completely vanish due to parity and time-reversal invariance, so the next-to-leading order stands for the second order of expansion.

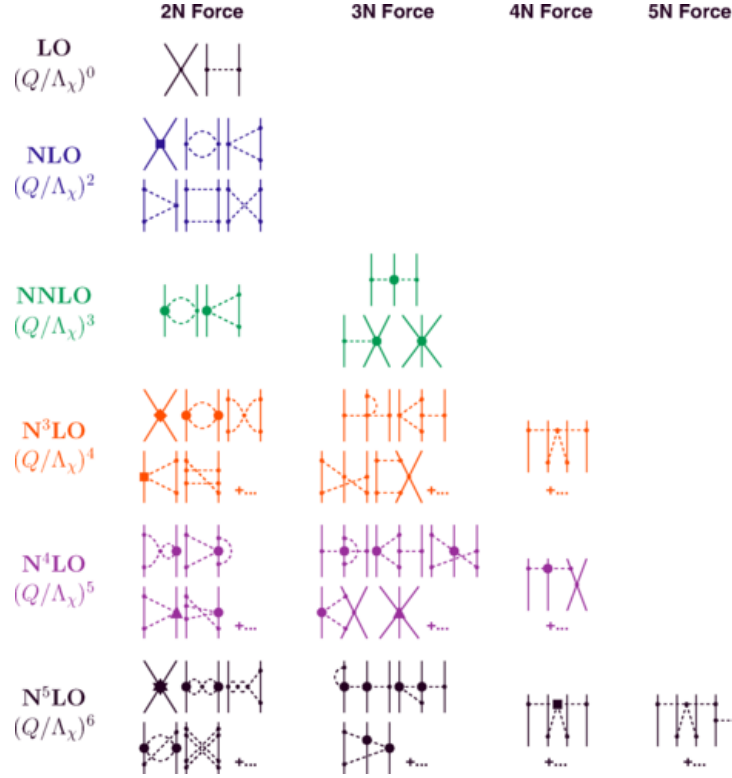


Figure 1.1: *Make own diagrams, e.g. with JaxoDraw or PyFeyn [26]*

almost simultaneously developing their models. In 1998 Epelbaum and collaborators from the Bochum-Bonn group presented a first version of their NN chiral potential [27, 28]. Developing a more and more sophisticated versions with higher chiral orders, authors presented N<sup>3</sup>LO potential in 2005 [29] which included a 3NF contributions. They were further developing their chiral model, taking into account more Feynmann diagrams coming to a higher chiral orders. At some moment Bochum-Bonn goup faced with a problem of potential regularisation [?]. *Solving it was an important point and autors...* An important point was when authors started using a semi-local regularisation in the coordinate space. The correspondant potential is called the SCS potential (semi-local regularisation in the coordinate space) [30]. Later similar regularisation, but done in momentum space was introduced, resulting in the most advanced chiral potential at the moment up to N<sup>4</sup>LO<sup>+</sup> chiral order [24]: the semilocal momentum-space regularized potential (SMS). It is developed up to N<sup>4</sup>LO<sup>+</sup> at the moment.

On the other side of the planet, in Idaho, Machleidt and his group from Moscow(Idaho) were also developing a chiral interaction. Their results from 2003 [31], following with later investigations [26, 32, 33] were introducing very similar model to the one from the Bochum-Bonn group with minor technical differences.

There are a number of another approaches within  $\chi$ EFT utilized. The group of M.Piarulli is using quite similar approach, including the same chiral potentials with minor differences [34, 35].

There are several other approaches within the framework of  $\chi$ EFT that have been utilized in nuclear physics. One of them is the work of Ekström et al. who developed a chiral effective theory for nuclear forces and currents that includes both nucleon and pion degrees of freedom [?]. Their approach is based on a power counting scheme that separates



long-range and short-range contributions and allows for systematic improvements in the calculations. Another approach is the pionless effective field theory, which neglects the pion degrees of freedom and focuses on the interactions between nucleons only [?].

Another important approach is the lattice effective field theory (LEFT), which is based on lattice QCD simulations of the strong interaction. Meissner and collaborators have developed a chiral effective theory for nuclear forces based on the results of lattice QCD calculations [?]. This approach has the advantage of being able to calculate the nuclear force directly from first principles, without the need for phenomenological input. However, it is limited to small systems and low energies due to the computational resources required for lattice QCD calculations.

**Machleidt, Ekström, pion-less EFT, Lattice EFT(Meissner), Girlanda, Piarulli**

Technically, the chiral potential may be derived both in coordinate and momentum spaces. Nevertheless in both cases it requires regularisation which cuts low coordinate values in order to avoid infinities or high momentum values. The SMS potential is being regularized semilocally. It means that local or nonlocal regularisations are being applied for different parts of the potential. In [29, 31] the non-local regularizer was applied to both short- and long-range parts of the potential where in the next [26, 30] potential it affected only a short range part. This regularisation is applied directly to the potential matrix elements in the coordinate space:

$$V_\pi(\vec{r}) \rightarrow V_{\pi,R}(\vec{r}) = V_\pi(\vec{r}) (1 - \exp(-r^2/R^2)) , \quad (1.4)$$

or in the momentum space

$$V_\pi(\vec{p}', \vec{p}) \rightarrow V_\Lambda(\vec{p}', \vec{p}) = V_\pi(\vec{p}', \vec{p}) \exp [-(p'/\Lambda)^{2n} - (p/\Lambda)^{2n}] , \quad (1.5)$$

where the cutoff  $R$  was chosen in the range of  $R = 0.8, \dots, 1.2$  fm,  $\Lambda = \frac{2}{R}$  and  $n$  being adjusted with respect to the considered chiral order. For specific case of SMS force  $\Lambda = 400 - 550$  MeV and  $n = 3$ .

The other way of regularisation, the local one, is applied to the propagator operator, already during the derivation of potential. Namely, the Gaussian form factor  $F(\vec{l}^2)$  is being used to reduce pions with higher momenta:

$$\int_{-\infty}^{\infty} \frac{\rho(\mu^2)}{\vec{l}^2 + \mu^2} d\mu^2 \rightarrow \frac{F(\vec{l}^2)}{\vec{l}^2 + \mu^2} \quad (1.6)$$

with

$$F(\vec{l}^2) = e^{-\frac{\vec{l}^2 + M_\pi^2}{\Lambda^2}} , \quad (1.7)$$

$M_\pi$  is an effective pion mass and  $\Lambda$  - a cutoff parameter and  $l$  is a four-momentum of the exchanged pion. The form factor (1.7), being used together with Feynman propagator, ensures that long-range part of the forces has no singularities.

The cut-off parameter  $\Lambda$  is not fixed and usually calculations are being performed with different values. The comparison of such results may reveal stronger or weaker dependance and in a perfect case, which is expected at  $\nu \gg 1$ , one will come up with such a potential, where the cut will not affect results at all. One of aims of my thesis is to test how big cut-off dependency of predictions is observed for the best currently available forces (SCS and SMS). To inspect the potential cutoff dependancy, in Fig. 1.2 I show values of the matrix elements for  $2N \langle p|V|p' \rangle$  potential  ${}^3S_1 - {}^3D_1$  as a function on the

momentum  $|\vec{p}|$  with fixed value  $|\vec{p}'|=0.054 \text{ fm}^{-1}$ .<sup>3</sup>

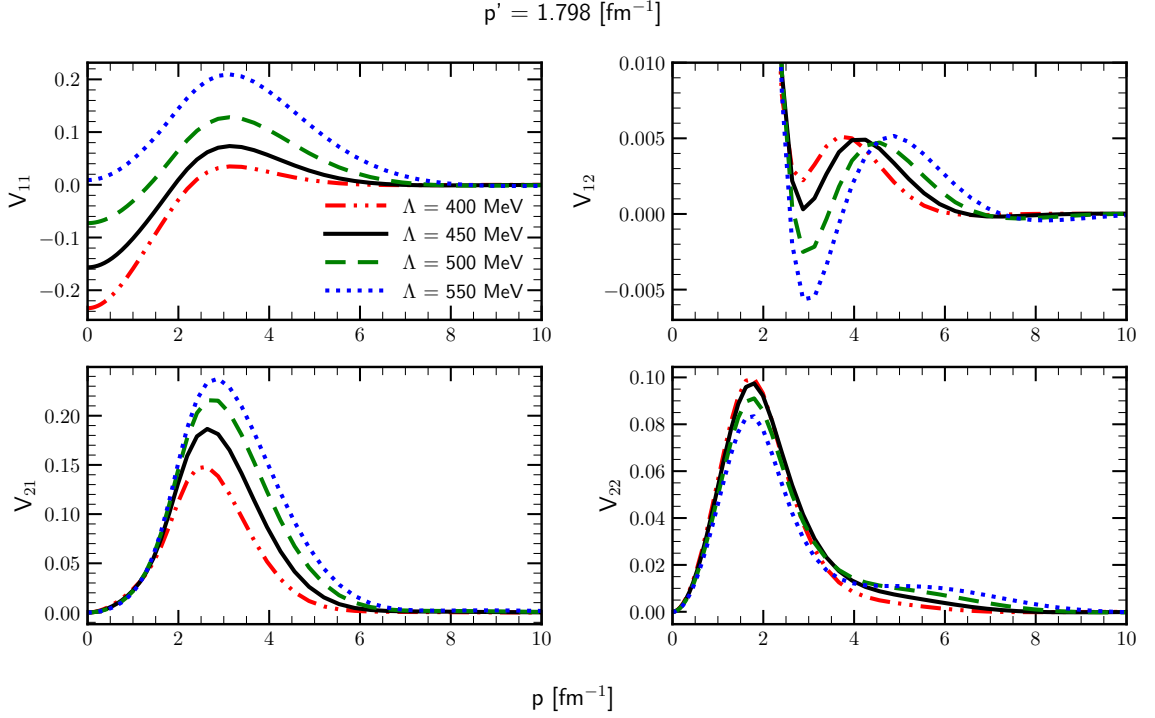


Figure 1.2: Potential components in case of coupled partial waves  $3S_1 - 3D_1$  as a function on the momentum  $p$  with fixed value of the momentum  $p' = 1.798 \text{ fm}^{-1}$ . *correct labels*

Yet another regularisation function is used by R. Machleidt, D.R. Entem and A. Nogga, when regulating matrix elements of the potential in momentum space with non-local regulator only. That is a main reason of the observed differences between predictions based on Epelbaum's and Machleidt's models.

## Currents

There are several types of nuclear currents used for studying scattering processes. One of the most common types is the one-body current, which describes the motion of individual nucleons within the nucleus. This type of current can be further divided into two categories: the convection current and the spin current. The convection current is associated with the motion of the center of mass of the nucleus, while the spin current is associated with the intrinsic spin of the nucleons.

Another important type of nuclear current is the two-body current, which describes the interaction between two nucleons within the nucleus. The two-body current is typically associated with meson exchange between the nucleons, and it plays a crucial role in scattering processes at low energies.

A third type of nuclear current is the three-body current, which describes the interaction between three nucleons within the nucleus. This type of current is particularly important for studying scattering processes involving light nuclei, such as helium-3 or tritium.

<sup>3</sup>Please note, that relatively strong dependancy of specific matrix element of the potential is not always leading to a strong dependancy of observables, as observables comprise *unclear from correction*

The use of nuclear currents in scattering experiments is essential for understanding the structure of the nucleus and the interactions between its constituent nucleons. Advances in theoretical and experimental techniques have allowed for more precise measurements of these currents and have provided insights into the fundamental properties of the nucleus.

The central element of the formalism is the nuclear part, denoted by  $\mathcal{N}^\lambda$ , which is given by the matrix element of the nuclear weak-current operator  $j_w^\lambda$  between the initial and final nuclear states. The single nucleon current operator, which is derived based on symmetry requirements is [36]:

$$\begin{aligned} & \left\langle \frac{1}{2}m' \left| \langle \mathbf{p}' | j_w^\lambda(1) | \mathbf{p} \rangle \right| \frac{1}{2}m \right\rangle \\ &= \bar{u}(\mathbf{p}', m') \left[ (g_1^V - 2Mg_2^V) \gamma^\lambda + g_2^V (p + p')^\lambda \right. \\ & \quad \left. + g_1^A \gamma^\lambda \gamma^5 + g_2^A (p - p')^\lambda \gamma^5 \right] \tau_- u(\mathbf{p}, m), \end{aligned} \quad (1.8)$$

which contains weak form factors  $g_1^V, g_2^V, g_1^A$ , and  $g_2^A$ , that are functions of the momentum-transfer squared  $(p' - p)^2$ . The difference between the proton mass  $M_p$  and neutron mass  $M_n$  is negligible so we can introduce the average "nucleon mass"  $M \equiv \frac{1}{2}(M_p + M_n)$ . The isospin lowering operator is  $\tau_- = (\tau_x - i\tau_y)/2$  in the isospin formalism. The nonrelativistic reduction of Eq. (1.8) results in the following forms of the time and space components of  $j_w^\lambda(1)$  The zero-component is

$$\langle \mathbf{p}' | j_{\text{NR}}^0(1) | \mathbf{p} \rangle = \left( g_1^V + g_1^A \frac{\boldsymbol{\sigma} \cdot (\mathbf{p} + \mathbf{p}')}{2M} \right) \tau_- \quad (1.9)$$

and space (vector) component

$$\begin{aligned} \langle \mathbf{p}' | \mathbf{j}_{\text{NR}}(1) | \mathbf{p} \rangle = & \left[ g_1^V \frac{\mathbf{p} + \mathbf{p}'}{2M} - \frac{1}{2M} (g_1^V - 2Mg_2^V) i\boldsymbol{\sigma} \times (\mathbf{p} - \mathbf{p}') \right. \\ & \left. + g_1^A \boldsymbol{\sigma} + g_2^A (\mathbf{p} - \mathbf{p}') \frac{\boldsymbol{\sigma} \cdot (\mathbf{p} - \mathbf{p}')}{2M} \right] \tau_- \end{aligned} \quad (1.10)$$

where  $\boldsymbol{\sigma}$  is a vector of Pauli spin operators. Here we have kept only terms up to  $1/M$ .

The two-nucleon current contribution is partially taken into account via Siegert approach [37, 38]. In order to do that we break down the single nucleon current matrix elements into multipole components and apply common formulas [38] to represent some of the electric multipoles using the Coulomb multipoles, which arise from the single nucleon charge density operator. This is acceptable because, in low-energy situations, contributions from many nucleons to the nuclear charge density are typically insignificant. We then obtain the rest of the electric multipoles and all of the magnetic multipoles exclusively from the single nucleon current operators.

---

# CHAPTER 2

---

## FORMALISM & NUMERICAL METHODS

Despite the deuteron problem was solved long time ago, I will describe it briefly in order to introduce the notation and formalism. With that, for more complex 3N case only slight extension will be needed.

In order to calculate any observable for the deuteron photodisintegration, one has to find a nuclear matrix elements:

$$N^\mu = \langle \Psi_{final} | J^\mu | \Psi_{initial} \rangle, \quad (2.1)$$

with two-nucleon wave function of the initial state  $\Psi_{initial} = \Psi_{deuteron}$ ; two-nucleon wave function of the final scattering state  $\Psi_{final}$  and a four-vector current operator  $J^\mu$  which acts between initial and final two-nucleon states. In following I describe how to get that quantities.

### 2.1 Deuteron bound state

Let's find a deuteron bound state wave function  $|\phi_d\rangle$ . The time-independent Schrödinger equation for two particles expresses as:

$$(H_0 + V) |\phi_d\rangle = E_d |\phi_d\rangle, \quad (2.2)$$

with a kinetic energy  $H_0$  and potential  $V$ . The kinetic energy  $H_0$  can be represented in terms of relative and total momenta of the particles:

$$H_0 = \frac{\vec{p}_1^2}{2m_1} + \frac{\vec{p}_2^2}{2m_2} = \frac{\vec{p}^2}{2\mu} + \frac{\vec{P}^2}{2M}, \quad (2.3)$$

where relative and total momenta are defined as follows:

$$\vec{p} = \frac{(m_1 \vec{p}_1 - m_2 \vec{p}_2)}{m_1 + m_2} \quad (2.4)$$

$$\vec{P} = \vec{p}_1 + \vec{p}_2 \quad (2.5)$$

$M = m_1 + m_2$  is a total mass,  $\mu = \frac{m_1 m_2}{M}$  is a relative mass of two nucleons and  $\vec{p}_i$  is a momentum of i-th particle.

Potential  $V$  is assumed to depend on the relative degrees of freedom only, so Eq. (2.2) may be decomposed into two separated equations:

$$\frac{\vec{p}^2}{2\mu} \langle \vec{p} | \Psi_{int} \rangle + \langle \vec{p} | V | \Psi_{int} \rangle = (E_d - E) \langle \vec{p} | \Psi_{int} \rangle \quad (2.6)$$

$$\frac{\vec{P}^2}{2M} \langle \mathcal{P} | \Psi \rangle = E \langle \mathcal{P} | \Psi \rangle, \quad (2.7)$$

with  $\langle \vec{p}, \vec{\mathcal{P}} | H_0 | \phi_d \rangle = \frac{\vec{p}^2}{2\mu} \langle \vec{p} | \Psi_{int} \rangle + \frac{\vec{P}^2}{2M} \langle \mathcal{P} | \Psi \rangle$ . So  $\Psi$  is a component of total wave function, which reflects a deuteron as a single object with momentum  $\vec{\mathcal{P}}$  while  $\Psi_{int}$  is an internal wave function describing interaction between nucleons. Basis state  $|\vec{p}\rangle$  obeys a completeness equation:

$$\int d^3\vec{p} |\vec{p}\rangle \langle \vec{p}| = \mathbb{1} \quad (2.8)$$

Eq.(2.6) is basically a Schrödinger equation for one particle with mass  $\mu$  in potential  $V$  and Eq.(2.7) can be regarded as a Schrödinger equation for particle with mass  $M$  in a free motion. Assuming that deuteron is at rest ( $E_{c.m.} = 0$ ) we can stick to the Eq.(2.6) only. Using completeness relation 2.8 we get:

$$\frac{\vec{p}^2}{2\mu} \langle \vec{p} | \Psi_{int} \rangle + \int d\vec{p}' \langle \vec{p} | V | \vec{p}' \rangle \langle \vec{p}' | \Psi_{int} \rangle = E_d \langle \vec{p} | \Psi_{int} \rangle \quad (2.9)$$

Working in 3 dimensional space is difficult (especially numerically) so I follow a standard path and introduce the partial-wave decomposed representation (PWD) of the momentum state, adding spin and isospin degrees of freedom in the following form:

$$|p\alpha\rangle \equiv |p(ls)jm_j\rangle |tm_t\rangle, \quad (2.10)$$

where quantum numbers  $l, s, j, t$  are orbital angular momentum, total spin, total angular momentum and total isospin respectively.  $m_j$  and  $m_t$  are total angular momentum and isospin projections, respectively.

States  $|p(ls)jm_j\rangle$  can be further decomposed to the main basis states than it is in (2.10), separating spin part as

$$|p(ls)jm_j\rangle = \sum_{m_l} c(ls j; m_l, m_j - m_l, m_j) |plm_l\rangle |s m_j - m_l\rangle. \quad (2.11)$$

Spin(isospin) states can be further represented via single-nucleon spin(isospin) states:

$$|sm_s\rangle = \sum_{m_1} c(\frac{1}{2} \frac{1}{2} s; m_1, m_s - m_1, m_s) \left| \frac{1}{2} m_1 \right\rangle \left| \frac{1}{2} m_s - m_1 \right\rangle, \quad (2.12)$$

$$|tm_t\rangle = \sum_{\nu_1} c(\frac{1}{2} \frac{1}{2} t; \nu_1, m_t - \nu_1, m_t) \left| \frac{1}{2} \nu_1 \right\rangle \left| \frac{1}{2} m_t - \nu_1 \right\rangle. \quad (2.13)$$

In Eqs.(2.11) -(2.13),  $c(\dots)$  are Clebsh-Gordon coefficients. Nucleons are spin  $\frac{1}{2}$  particles, and also we treat proton and neutron as the same particle in different isospin states, so that isospin  $\nu_1 = \frac{1}{2}$  stands for proton and  $\nu_1 = -\frac{1}{2}$  for neutron.

The states  $|plm_l\rangle$  from Eq.(2.11) are orthogonal

$$\langle p'l'm'_l | plm_l \rangle = \frac{\delta(p-p')}{p^2} \delta_{ll'} \delta_{m_l m'_l} \quad (2.14)$$

and also satisfy the completeness relation:

$$\sum_{l=0}^{\infty} \sum_{m_l=-l}^l \int dp p^2 | plm_l \rangle \langle plm_l | = \mathbb{1} \quad (2.15)$$

Projection of  $\langle \vec{p}' |$  states to  $| plm_l \rangle$  leads to

$$\langle \vec{p}' | plm_l \rangle = \frac{\delta(|\vec{p}'| - p)}{p^2} Y_{lm_l}(\hat{p}'), \quad (2.16)$$

where  $Y_{lm_l}(\hat{p}')$  is a spherical harmonic and 'hat' denotes a unit vector  $\hat{X}$  in direction of  $\vec{X}$ . So for the momentum vector:

$$\vec{p} \equiv |\vec{p}| \hat{p} \equiv p \hat{p}. \quad (2.17)$$

Nucleons are fermions so exchanging them leads to antisymmetry of the wave function. In PWD it results in additional requirement on allowed quantum numbers which is:

$$(-1)^{l+s+t} = -1. \quad (2.18)$$

In general, nuclear NN force conserves spin, parity and charge so

$$\langle p' \alpha' | V | p \alpha \rangle = \delta_{jj'} \delta_{mm'} \delta_{tt'} \delta_{m_t m'_t} \delta_{ss'} V_{ll'}^{s j t m_t}(p', p) \quad (2.19)$$

which introduces restrictions for particular sets of quantum numbers. Strong interaction allows for change of the orbital angular momenta  $l = j \pm 1$ ,  $l' = j' \pm 1$ . The channels, where  $l \neq l'$  are coupled and for the deuteron bound state one can find only one possible PWD state combination: two coupled channels which are commonly denoted as  $^3S_1$  and  $^3D_1$  (the naming stands for  $^{2s+1}l_j$ ). They correspond to  $l = 0$  and  $l = 2$  respectively (with  $s = j = 1$  and  $t = m_t = 0$ ). We will call wave functions for these channels as  $\phi_l(p)$  with  $l = 0, 2$ , such that:

$$\phi_l(p) = \langle p(ls)jm_j | \langle tm_t | \Psi_{int} \rangle = \langle p(l1)1m_d | \langle 00 | \Psi_{int} \rangle; l = 0, 2. \quad (2.20)$$

In that new basis Eq.(2.9) takes a form of two coupled equations:

$$\frac{\vec{p}^2}{2\mu} \phi_l(p) + \sum_{l'=0,2} \int dp' p'^2 \langle p(l1)1m_d | \langle 00 | V | 00 \rangle | p'(l'1)1m_d \rangle \phi_{l'}(p') = E_d \phi_l(p), \quad (2.21)$$

for  $l = 0, 2$ . In case one does not have a matrix elements for the potential  $\langle plm_l | V | p'l'm'_l \rangle$  in analytical form, but only numerical values for some grid of points, there is still one complication in the Eq.(2.21) - integration, which has to be discretized. In order to get rid of the integral I use a Gaussian quadrature method of numerical integration [39]. It allows to replace an integral by the weighted sum:  $\int_a^b f(x) dx = \sum_{i=1}^n \omega_i f(x_i)$  In current work I used  $N = 72$  points in the interval from 0 to  $50 \text{ fm}^{-1}$ . Using this method, Eq.(2.21) becomes

$$\frac{p_i^2}{2\mu}\phi_l(p_i) + \sum_{l'=0,2} \sum_{j=0}^{N_P} \omega_j p_j^2 \langle p_i(l1)1m_d | \langle 00|V|00\rangle |p_j(l'1)1m_d\rangle \phi_{l'}(p_j) = E_d \phi_l(p_i). \quad (2.22)$$

In practical computations, the same grid points  $p_i$  and  $p_j$  are used in order to optimize computational time. I solve this equation as an eigenvalue problem  $M\Psi = E_d\Psi$  and in that way find simultaneously wave function values in grid of  $p$  points and binding energy  $E_d$ . The binding energy  $E_d$  calculated with potentials of different chiral orders is presented in Fig. 2.1.

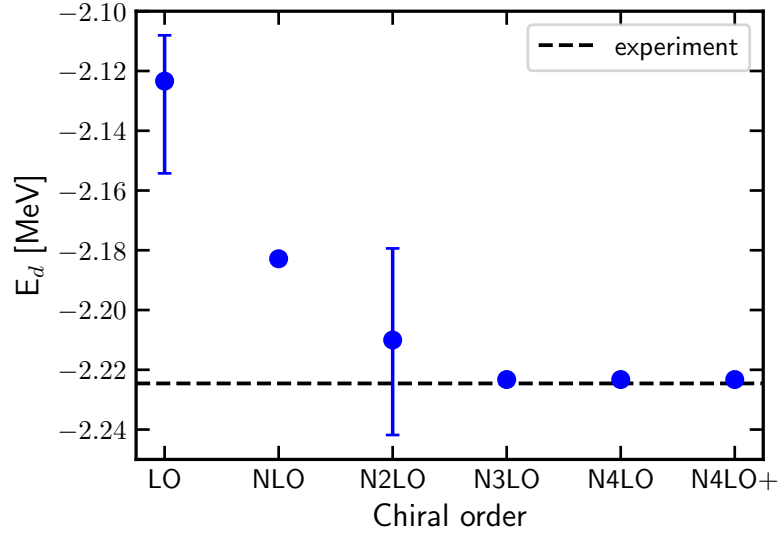


Figure 2.1: Deuteron binding energy calculated using the chiral SMS potential at different chiral orders as a mean value over all cutoffs. Error bands represent a spread the calculated binding energy with respect to the cutoff parameter  $\Lambda$  (minimal and maximal values). Experimental data is taken from [40]

An example of such wave functions is demonstrated in Fig. 2.2. The left pane demonstrate a wave function for  $l = 0$  -  $^3S_1$  while the right one - for  $l = 2$  -  $^3D_1$ . Both plots consist of the curves for different cutoff values and using the chiral SMS potential at N<sup>4</sup>LO<sup>+</sup>. The small deviation between lines show that cutoff dependency is rather weak at this stage and further discrepancies connected to the value of  $\Lambda$  may appear in other components.

## 2.2 2N scattering state

### 2.2.1 The Lippmann-Schwinger equation

Let us start from the time-independent formulation of the scattering process. In such a case Hamiltonian is:

$$H = H_0 + V, \quad (2.23)$$



Figure 2.2: Wave function  $\phi_l$  for  $l=0$  ( ${}^3S_1$  partial wave)(left) and  $l=2$  ( ${}^3D_1$ ) (right). Each curve shows results obtained with different values of the cutoff parameter  $\Lambda$ , results have been obtained using the chiral SMS potential at  $N^4LO^+$ .

where again  $H_0$  is a kinetic energy operator  $H_0 = \frac{\vec{p}^2}{2m}$  and  $V$  is a nucleon-nucleon interaction. For a free particle motion,  $V$  will be absent and we will denote a corresponding energy eigenstate as a free particle state  $|\vec{p}_0\rangle$ . The scattering state  $|\psi\rangle$  fulfills similar Schrödinger equation as  $|\vec{p}_0\rangle$ , with the same energy eigenvalue, but with potential presented:

$$\begin{cases} H_0 |\vec{p}\rangle &= E |\vec{p}\rangle \\ (H_0 + V) |\psi\rangle &= E |\psi\rangle \end{cases} \quad (2.24)$$

We are interested in solution for Eq. (2.24), so that  $|\psi\rangle \rightarrow |\vec{p}\rangle$  as  $V \rightarrow 0$  and both  $|\psi\rangle$  and  $|\vec{p}\rangle$  have the same energy eigenvalues  $E$ . As we have scattering process, the energy spectra for both operators  $H_0$  and  $H_0 + V$  are continuous.

From Eq. (2.24) follows that

$$|\psi\rangle = \frac{1}{E - H_0} V |\psi\rangle + |\vec{p}\rangle, \quad (2.25)$$

which guarantees that application of the operator  $(E - H_0)$  to the (2.25) results in the second equation from the set (2.24).

In order to deal with a singular operator  $\frac{1}{E - H_0}$  in Eq. (2.25), the well-known technique is to make such an operator complex by adding small imaginary number to the denominator so Eq.(2.25) becomes

$$|\psi\rangle = G_0(E \pm i\epsilon) V |\psi\rangle + |\vec{p}\rangle, \quad (2.26)$$

where  $G_0$  is a free propagator:

$$G_0(z) = \frac{1}{z - H_0}. \quad (2.27)$$

Solution with  $G_0(E - i\epsilon)$  corresponds to the incoming spherical wave, while  $G_0(E + i\epsilon)$  - to the outgoing one. Since we are interested in the final scattering state, only the (+) sign survives.



Eq. (2.26) is known as the Lippmann-Schwinger equation (LSE). Defining the transition operator  $t$ :

$$t |\vec{p}\rangle = V |\psi\rangle \quad (2.28)$$

we can rewrite it as

$$|\psi\rangle = (1 + G_0(E + i\epsilon)t) |\vec{p}\rangle \quad (2.29)$$

With substitution of Eq. (2.26) into Eq. (2.28) we can find an explicit form of the  $t$  operator:

$$\begin{aligned} t |\vec{p}\rangle &= VG_0(E + i\epsilon)V |\psi\rangle + V |\vec{p}\rangle = \\ &= VG_0(E + i\epsilon)t |\vec{p}\rangle + V |\vec{p}\rangle \end{aligned} \quad (2.30)$$

Getting rid off the initial state  $|\vec{p}\rangle$  in the Eq. (2.30) we can get the LSE for the transition operator in the iterative form:

$$\begin{aligned} t &= V + VG_0t = \\ &= V + VG_0V + VG_0VG_0V + \dots, \end{aligned} \quad (2.31)$$

which constitutes an infinite series of subsequent NN interactions and free propagators of nucleons.

In the partial-wave representation, the LSE Eq. (2.30) expresses as:

$$\begin{aligned} \langle p'(l's')j'm_{j'} | \langle t'm_{t'} | t(E) | tm_t \rangle | p(ls)jm_j \rangle &= \langle p'(l's')j'm_{j'} | \langle t'm_{t'} | V | tm_t \rangle | p(ls)jm_j \rangle + \\ &+ \sum_{\alpha''} \int_0^\infty dp'' p''^2 \langle p'(l's')j'm_{j'} | \langle t'm_{t'} | V | t''m_{t''} \rangle | p''(l''s'')j''m_{j''} \rangle \\ &\times \frac{1}{E + i\epsilon - p''^2/m} \langle p''(l''s'')j''m_{j''} | \langle t''m_{t''} | t(E) | tm_t \rangle | p(ls)jm_j \rangle, \end{aligned} \quad (2.32)$$

which after using symmetries of potential matrix elements (2.19) reduces to

$$\begin{aligned} \langle p'(l's')jt | t(E) | p(ls)jt \rangle &= \langle p'(l's')jt | V | p(ls)jt \rangle + \\ &+ \sum_{l''} \int_0^\infty dp'' p''^2 \langle p'(l's')jt | V | p''(l''s)jt \rangle \\ &\times \frac{1}{E + i\epsilon - p''^2/m} \langle p''(l''s)jt | t(E) | p(ls)jt \rangle. \end{aligned} \quad (2.33)$$

I solve Eq. (2.33) numerically, which again requires discretisation and therefor leads to set of linear equations. Finally, using Eq. (2.29) and denoting the momentum state of two nucleons with spin projections  $m_p$  and  $m_n$  as  $\langle \phi m_p m_n |$ , we can write Eq. (2.1) as

$$N^\mu = \langle \phi m_p m_n | (1 + G_0(E + i\epsilon)t) \frac{1}{e} J^\mu(0) | \Psi_i \vec{P}_i \rangle \quad (2.34)$$

## 2.3 3N bound state

The 3N bound state is described by the Schrödinger equation for 3N system and its total wave function obeys the following equation:

$$|\Psi\rangle = G_0(E + i\epsilon) \sum_{j=1}^3 (V_j + V_4^j) |\Psi\rangle, \quad (2.35)$$

where  $G_0$  is a free propagator from Eq. (2.27),  $V_j$  - is a two-body potential acting between nucleons  $k$  and  $l$  ( $j, k, l$  - numerate nucleons,  $j, k, l \in 1, 2, 3$  and  $j \neq k \neq l$ ) and  $V_4^j$  is a component of three-body potential  $V_4 = \sum_{j=1}^3 V_4^j$  symmetrical under exchange of nucleons  $k$  and  $l$ ,  $E$  - is a binding energy.

Eq. (2.35) can be split into 3 independent equations for so-called Faddeev components  $|\psi_j\rangle$

$$|\Psi\rangle = \sum_{j=1}^3 |\psi_j\rangle, \quad (2.36)$$

which fulfills separately

$$|\psi_j\rangle = G_0(E + i\epsilon)(V_j + V_4^j) |\Psi\rangle. \quad (2.37)$$

Next, I introduce a permutation operator  $P$ , which is a combination of operators  $P_{jk}$ :

$$P = P_{12}P_{23} + P_{13}P_{32}. \quad (2.38)$$

The operator component  $P_{jk}$  acting on the state interchange the momenta and quantum numbers of the nucleons  $j$  and  $k$ .

Using definitions 2.38 and 2.36, one can rewrite Eq. (2.37) as:

$$|\psi_j\rangle = G_0(E + i\epsilon)t_j P |\psi_j\rangle + (1 + G_0(E + i\epsilon)t_j)G_0(E + i\epsilon)V_4^j(1 + P) |\psi_j\rangle, \quad (2.39)$$

where  $t_j$  is a two-body t-operator which obeys Eq. (2.30) for corresponding two-body potential  $V_j$ .

The partial wave representation of the Eq. (2.39) is obtained using following states:

$$|p, q, \alpha_{J, M_J}\rangle = \left| p, q, (ls)j, (\lambda, \frac{1}{2})I(jI)JM; (t\frac{1}{2})TM_T \right\rangle_1, \quad (2.40)$$

where index 1 states the choice of the Jakobi momenta, such that  $p$  is a relative momentum of the nucleons 2 and 3. Values  $l, s$  and  $j$  are quantum numbers in the two-body subsystem consisted of nucleons 2 and 3.  $\lambda$  is the orbital angular momentum of the first particle which spin is  $\frac{1}{2}$  and total angular momentum  $I$ .  $J$  and  $M_J$  are the total angular momentum of the 3N system and its projection on the z-axis respectively.  $y$  is a total isospin of the 2-3 subsystem whereas  $T$  and  $MT$  are the total isospin of the 3N system and its projection on the z-axis.

Using states defined in Eq. (2.40), we can write a partial-wave representation of the

Eq. (2.39):

$$\begin{aligned}
 \langle p, q, \alpha_{J,M_J} | \psi_i \rangle = & \frac{1}{E - \frac{p^2}{m} - \frac{3q^2}{4m} + i\epsilon} [ \\
 & \sum_{\alpha', \alpha''} \int_0^\infty dq'' q''^2 \int_{-1}^1 dx t_{\alpha, \alpha'}^+ \left( p, \pi_1(q, q'', x), E - \frac{3q}{4m} \right) \\
 & * \frac{\tilde{G}_{\alpha', \alpha''}(q', q'', x)}{\pi_1' \pi_2'''} \left\langle \pi_2, q'', \alpha_{J'', M_{J''}} | \psi_i \right\rangle \\
 & + \sum_{\alpha''} \int_0^\infty dp'' p''^2 \int_0^\infty dq'' q''^2 V_{\alpha, \alpha''}^4(p, q, p'', q'') \left\langle p'', q'', \alpha_{J'', M_{J''}} | \psi_i \right\rangle \\
 & + \sum_{\alpha', \alpha''} \int_0^\infty dq' q'^2 \int_0^\infty dq'' q''^2 \int_{-1}^1 dx V_{\alpha, \alpha'}^4(p, q, \pi_1(q', q'', x), q') \\
 & + \frac{\tilde{G}_{\alpha', \alpha''}(q', q'', x)}{\pi_1' \pi_2'''} \left\langle \pi_2, q'', \alpha_{J'', M_{J''}} | \psi_i \right\rangle \\
 & + \sum_{\alpha', \alpha''} \int_0^\infty dp' p'^2 \int_0^\infty dp'' p''^2 \int_0^\infty dq'' q''^2 t_{\alpha, \alpha'}^+ \left( p, p', E - \frac{3q^2}{4m} \right) \frac{1}{E - \frac{p'^2}{m} - \frac{3q^2}{4m} + i\epsilon} \\
 & * V_{\alpha', \alpha''}^4(p', q, p'', q'') \left\langle p'', q'', \alpha_{J'', M_{J''}} | \psi_i \right\rangle \\
 & + \sum_{\alpha', \alpha'', \alpha'''} \int_0^\infty dp' p'^2 \int_0^\infty dq'' q''^2 \int_0^\infty dq' q'^2 \int_{-1}^1 dx t_{\alpha, \alpha'}^+ \left( p, p', E - \frac{3q^2}{4m} \right) \\
 & * \frac{1}{E - \frac{p'^2}{m} - \frac{3q^2}{4m} + i\epsilon} V_{\alpha', \alpha'''}^4(p', q, \pi_1(q', q'', x), q') \\
 & * \frac{\tilde{G}_{\alpha''', \alpha''}(q', q'', x)}{\pi_1''' \pi_2'''} \left\langle \pi_2, q'', \alpha_{J'', M_{J''}} | \psi_i \right\rangle \Big],
 \end{aligned} \tag{2.41}$$

where

$$V_{\alpha, \alpha'}^4(p, q, p', q') \equiv \left\langle p, q, \alpha_{J, M_J} \left| V_4^{(1)} \right| p', q', \alpha_{J', M_{J'}} \right\rangle \tag{2.42}$$

## 2.4 3N scattering state

As in Sec. 2.5, one can write an equation for the 3-nucleon scattering state:

$$|\Psi^{(-)}\rangle^{3N} = \frac{1}{\sqrt{3}} \left| \Psi_j^{(-)} \right\rangle^{3N} \tag{2.43}$$

with a set of corresponding equations for  $\left| \Psi_j^{(-)} \right\rangle^{3N}$

$$\left| \Psi_j^{(-)} \right\rangle^{3N} \equiv \lim_{\epsilon \rightarrow 0} i\epsilon G(E_{3N} - i\epsilon) \left| \Phi_j^{3N} \right\rangle \quad (2.44)$$

$$\left| \Phi_j^{3N} \right\rangle \equiv \frac{1}{\sqrt{2}} (1 - P_{kl}) |\vec{p}(kl) \vec{q}(j)\rangle \quad (2.45)$$

$$E_{3N} = \frac{|\vec{p}|^2}{m} + \frac{3|\vec{q}|^2}{4m}, \quad (2.46)$$

Taking into account antisymmetrized Faddeev components

$$\left| F_i^0 \right\rangle \equiv G_0 \left( V_i + V_4^{(i)} \right) (1 + P) \left| \Psi_i^{(-)} \right\rangle^{3N} \quad (2.47)$$

we can obtain a 3N scattering wave function as:

$$\begin{aligned} \left| \Psi^{(-)} \right\rangle^{3N} &= \frac{1}{\sqrt{3}} \left( \sum_{i=1}^3 \left| \Phi_i^{3N} \right\rangle + G_0 (V_1 + V_2 + V_3 + V_4) \sum_{i=1}^3 \left| \Psi_i^{(-)} \right\rangle^{3N} \right) \\ &= \frac{1}{\sqrt{3}} \left( \sum_{i=1}^3 \left| \Phi_i^{3N} \right\rangle + \sum_{i=1}^3 \left| F_i^0 \right\rangle \right) \\ &= \frac{1}{\sqrt{3}} (1 + P) \left( \left| \Phi_1^{3N} \right\rangle + \left| F_1^0 \right\rangle \right). \end{aligned} \quad (2.48)$$

In this case nuclear matrix element is:

$$\begin{aligned} N_\mu^{3N} &= \frac{1}{\sqrt{3}} \langle \Phi_1^{3N} | (1 + P) j_\mu | \Psi_i \rangle + \frac{1}{\sqrt{3}} \langle \Phi_1^{3N} | t_1^+ G_0^+ (1 + P) j_\mu | \Psi_i \rangle \\ &\quad + \frac{1}{\sqrt{3}} \langle \Phi_1^{3N} | t_1^+ G_0^+ P | U_\mu \rangle + \frac{1}{\sqrt{3}} \langle \Phi_1^{3N} | P | U_\mu \rangle. \end{aligned} \quad (2.49)$$

## 2.5 Photodisintegration transition amplitude for Nd state

Analogously to the bound state, one can express a nucleon-deuteron scattering state using a permutation operator Eq. (2.38).

$$\left| \Psi^{(-)} \right\rangle^{Nd} = \frac{1}{\sqrt{3}} (1 + P) \left| \Psi_1^{(-)} \right\rangle^{Nd} \quad (2.50)$$

Further a scattering state  $\left| \Psi_1^{(-)} \right\rangle^{Nd}$  can be expressed in terms of asymptotic state  $\left| \Phi_1^{Nd} \right\rangle$ , in which particles 2 and 3 form a deuteron and the third particle (nucleon 1) propagates freely with a relative momentum  $\vec{q}_0$  with respect to the deuteron:

$$\left| \Psi_1^{(-)} \right\rangle^{Nd} \equiv \lim_{\epsilon \rightarrow 0} i\epsilon G(E_{Nd} - i\epsilon) \left| \Phi_1^{Nd} \right\rangle \quad (2.51)$$

$$\left| \Phi_1^{Nd} \right\rangle \equiv \left| \Phi_{d(2,3)} \right\rangle |\vec{q}_0\rangle, \quad (2.52)$$

where  $\left| \Phi_{d(2,3)} \right\rangle$  is a deuteron wave function and  $|\vec{q}_0\rangle$  - a free particle state.  $E_{Nd}$  is a total

energy of the 3N system:

$$E_{Nd} = E_d + \frac{3|\vec{q}_0|^2}{4m}, \quad (2.53)$$

where  $E_d$  is the deuteron binding energy and  $m$  denotes nucleon mass.

The full propagator  $G(E_{Nd})$  in this case takes a form:

$$G(z) = \frac{1}{z - (H_0 + \sum_{i=1}^4 V_i)} \quad (2.54)$$

## 2.6 Nuclear electromagnetic current

The electromagnetic current operator for a few-nucleon system has both one- and many-body contributions, which can be denoted as  $j_\mu^1$ ,  $j_\mu^2$ , and  $j_\mu^3$ , respectively. The leading one-body contribution,  $j_\mu^1$ , represents the photon's interaction with a single nucleon. The many-body contributions are known as meson exchange currents (MEC), which arise due to the meson-exchange picture of the nucleon-nucleon (NN) interaction. The photon can couple to mesons exchanged between two nucleons, leading to two-body contributions to the nuclear current.

The necessity of introducing the MEC arises from the continuity equation, which requires the inclusion of two-body interactions in the Hamiltonian. The momentum and isospin-dependent terms in  $V$  require the introduction of two-body MEC. Similarly, the inclusion of the three-body force into the Hamiltonian requires the existence of three-body contributions to the nuclear current. However, the effects of the three-body MEC are likely negligible in the low-energy region. Therefore, we will only consider one- and two-body currents.

The nuclear one-body current is constructed based on the electromagnetic current for a Dirac particle. To account for the extended structure of nucleons, form factors are introduced. Since we use nonrelativistic wave functions, we need to use nonrelativistic currents.

## 2.7 Theoretical uncertainties

### Truncation error

As it was mentioned above, each subsequent order of the chiral expansion provides us with more and more sophisticated potential which is expected to increase accuracy of data description. Starting from the leading order (LO) and coming next to N2LO, N3LO etc., we take into account more topologies (equivalents of Feynmann diagrams) and in result potential is expected to provide us with more precise predictions for the regarded process and observables. However, the chiral expansion (as any expansion) in principle can be continued up to the infinity, improving the resulting series. In practice we are limited to a finite, rather small, order and we would like to find out the uncertainty appearing from cutting off remaining part of the expansion. That type of theoretical uncertainty is called a truncation error. Various methods to estimate its value have been proposed [41–45]. Typically predictions at lower orders serve as input information to get truncation error at given order. It is worth adding that Bayesian analysis is also used for truncation error estimation

We use the method proposed in [43] which was shown to be equivalent to Bayesian approach. Let's regard some prediction  $X^i(p)$  for observable  $x$  which is calculated at  $i$ -s order of chiral expansion with expansion parameter  $Q$  ( $i = 0, 2, 3, \dots$ )<sup>1</sup>. Here  $p$  specifies a momentum scale of the current reaction in the center of mass frame (in the case of photodisintegration it would be a photon's momentum).

If we define a difference between observable at each subsequent orders as:

$$\Delta X^{(2)} = |X^{(2)} - X^{(0)}|, \Delta X^{(i>2)} = |X^{(i)} - X^{(i-1)}|, \quad (2.55)$$

then chiral expansion for  $X$  can be written as:

$$X = X^{(0)} + \Delta X^{(2)} + \Delta X^{(3)} + \dots + \Delta X^{(i)}. \quad (2.56)$$

The truncation error at  $i$ -th order,  $\delta X^{(i)}$ , is estimated using actual and expected values of the observable at higher orders as following:

$$\delta X^{(0)} = Q^2 |X^{(0)}|, \quad (2.57)$$

$$\delta X^{(i)} = \max_{2 \leq j \leq i} (Q^{i+1} |X^{(0)}|, Q^{i+1-j} |\Delta X^{(j)}|). \quad (2.58)$$

Additionally, following the [43] I use also the actual high-order predictions (if known) in order to specify uncertainties so that:

$$\delta X^{(i)} \geq \max_{j,k} (|X^{j \geq i} - X^{k \geq i}|) \quad (2.59)$$

and to be conservative I use additional restriction:

$$\delta X^{(i)} \geq Q \delta X^{(i-1)}. \quad (2.60)$$

All the conditions above assume that we use the whole available information at hand. In [46] [?????](#) it was shown that such method is equivalent to Bayesian approach of [46].

## Cutoff dependency

Another theoretical uncertainty comes from the choice of the cutoff parameter's value of regulator described in chapter [?????? put link](#).

The free parameters of SMS potential have been obtained from data for four values of the cutoff parameter  $\Lambda$ : 400, 450, 500 and 550 MeV [24]. Using each of these values, one obtains different predictions which of course can further differ from actual (experimental) value. Therefore the choice of  $\Lambda$  value may affect a quality of the prediction.

To study that I also use the same four values of the  $\Lambda$  parameter, obtaining in that way four predictions each time. That is exemplified in Fig. 2.3 for the deuteron photodisintegration cross section for the photon's energy  $E_\gamma = 30$  MeV, 100 MeV and 140 MeV. The SMS model at  $N^4\text{LO}^+$  is used. Each subfigure shows a predictions for the total cross section as a function of the cutoff parameter, normalized to the maximum value among all cross sections obtained with various  $\Lambda$ . As we can see, for that observable there is almost linear dependance with positive linearity coefficient value: with higher  $\Lambda$  the cross section value increases as well. Note that with higher photon's energy, the cutoff

<sup>1</sup>We do not have a first order of expansion because this term in chiral expansion is always vanished and NLO corresponds to the quadratic term (number 2)

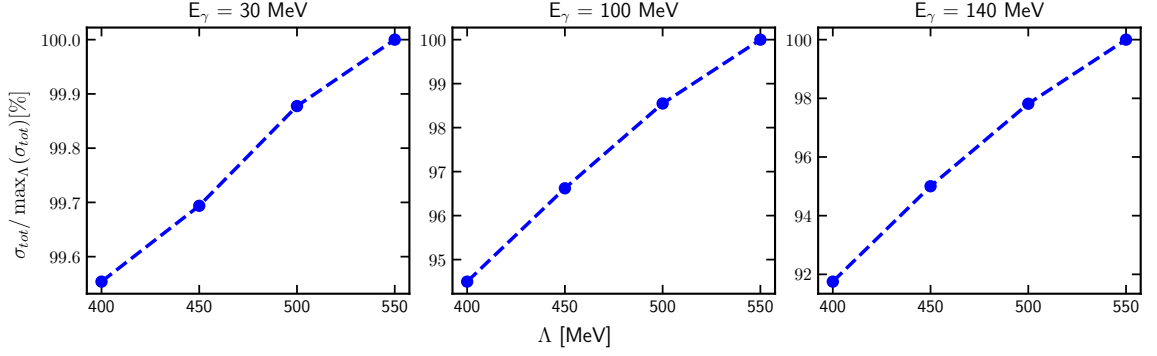


Figure 2.3: Total cross section of the deuteron photodisintegration process (normalized to the maximal cross section among all  $\Lambda$ ) as a dependence on the cutoff parameter  $\Lambda$  for three photon energy  $E_\gamma$  values: 30, 100 and 140 MeV.

dependence becomes stronger: for  $E_\gamma = 30$  MeV the maximal difference between predictions is around 0.5 % while for 140 MeV it increases to more than 8 %. This results are generally within our expectations that our model works better at smaller energies and is less sensitive to the  $\Lambda$  value. Let us remind that  $\Lambda$  governs the behavior of the potential at small internucleon distances and only higher energy transfer probes that distances.

## Other theoretical uncertainties

There are obviously more sources of theoretical uncertainties. Our model has a number of either intrinsic limitations in precision or some simplifications which may be improved with further developments of the model.

**Nuclear currents** At the moment, our model is limited to a single nucleon current, which may not be sufficient to accurately describe the processes under consideration. This limitation will be further discussed and confirmed in Chapter 3. To address this issue, we utilize the Siegert theorem, which enables us to incorporate some contributions from the two-nucleon current, although it is not yet complete. It is worth noting that the incorporation of the two-nucleon current can significantly affect the predicted observables, as it includes additional physical effects that are not accounted for in the single nucleon current. Therefore, the ongoing development of a complete two-nucleon current in our model is of great importance to improve the accuracy of our predictions.

**Nonrelativistic approach** All the results presented here does not include relativistic corrections. At the lower energies the relativistic contribution might not be crucial, but at the region with higher energy we may see a lack of precision. This well be also confirmed and discussed regarding the total cross section for the deuteron photodisintegration Fig. 3.2.

**Uncertainties in the potential free parameters** ????

**Uncertainties from the numerical method** All the results include numerical calculations, so we can come up with a lot of places were numerical methods with limited precision come into the scene. Our approach is based on the partial wave decomposition

which supposes that limited number of partial waves are included (usually for 2N scattering we use  $j^{max} = 4$  which corresponds to 18 partial waves). For 3N calculations we use  $J^{max} = 5$  which corresponds to 40 partial waves. In addition, we with some grid of points which is used for the calculation of potential, wave function, numerical integration etc. The choice of grid affect a final results' precision. Usually, we use a grid *of ... values* which was proven to make resulting uncertainty small.

**Model choice** We focus on the SMS potential, but using another model of interaction leads to different predictions. That difference is also a theoretical uncertainty thus we use predictions obtained with AV18 model in order to compare these predictions. The AV18 model is a widely used and well-established model of nuclear interaction, which has been extensively tested and benchmarked against experimental data. By comparing the predictions obtained from the SMS potential with those obtained from the AV18 model, we can assess the robustness of our results and determine the extent to which they depend on the choice of the interaction model. This comparison also helps to identify the strengths and weaknesses of each model and provides insights into the underlying physics of nuclear interactions.

**Machine precision** Finally, it should be noted that every computer calculation includes limited numerical machine precision which can be noticeable for complex calculations. We perform our calculations via CPU machine, where the particular choice of the processor and memory card may lead to numerical uncertainty. However, we have found that this uncertainty is much smaller than the uncertainties discussed above, and its impact on our results is negligible. We have taken great care to ensure that our calculations are performed using appropriate numerical methods and sufficient computational resources to minimize any numerical errors that may arise.



---

# CHAPTER 3

---

## RESULTS

In this chapter I will show results of my calculations. I start from the deuteron photodisintegration process (Section 3.1), presenting predictions and discussing the cross (subsection 3.1.1) and polarization observables (subsection 3.1.2). Next, in Section 3.2 I will present my predictions of the observables for  $^3\text{He}$  photodisintegration. ... Finally in Section 3.4 I will discuss results of the calculations for pion absorption from the lowest atomic orbital.

### 3.1 Deuteron photodisintegration

#### 3.1.1 Cross section

In this section I will show the results of my calculation starting from the deuteron photodisintegration process. One of the most studying observable is obviously the cross section. There is a number of papers which present measurement results for both differential and total cross section [1, 47–54] and it seems interesting to compare our predictions with experimental results.

In Fig. 3.1 and Fig. 3.2 I present predictions for the total cross section  $\sigma_{tot}$  [ $\mu\text{b}$ ] which I obtained using the chiral SMS potential at the  $\text{N}^4\text{LO}^+$  order and with the cutoff parameter  $\Lambda = 450\text{ MeV}$ . From Fig. 3.1, we see that at low photon energies (below 50 MeV) predictions which include 2N contributions to the electromagnetic current via the Siegert approach, describe experimental results quite well. We can suppose that the difference with experimental data may come from the statistical uncertainty of the data itself, as my predictions are often in between the data from different experiments. Moreover, even at such low energies the 1N current is clearly not enough to describe cross section - dashed pink line has much lower values and the difference becomes even larger with increasing photon energies. At 5 MeV the difference between 1N predictions and 1N + Siegert is  $297.54\ \mu\text{b}$  (10.8%), increasing energy to 10 MeV it is  $304.28\ \mu\text{b}$  (20.4%) and at 20 MeV it is  $229.50\ \mu\text{b}$  (39.2%). From Fig. 3.1 we see that the gap between these predictions continues increasing even more with larger energies. This tells us that Siegert approach works quite well as no additional 2N contributions are taken into account. The cross section predictions corrected via Siegert 2N contribution reproduce experimental data to some extend.

Here and later the relative difference between set of predictions  $(x_1, x_2, \dots, x_N)$  is calculated using the formula:

$$\Delta = \frac{\max(x) - \min(x)}{\frac{1}{N} \sum_{i=1}^N x_i} \cdot 100\%, \quad (3.1)$$

so in the specific case of comparison the data with 1N current and "1N + Siegert" we calculate relative difference as  $\Delta = \frac{|\sigma^{1N+Siegert} - \sigma^{1N}|}{0.5(\sigma^{1N+Siegert} + \sigma^{1N})}$ .

While my main goal is to describe deuteron photodisintegration at low energies, where predictions seem to be well describing experimental data at  $E_\gamma \lesssim 50$  MeV, it is also interesting to check how present theory works at higher energies. At the higher energies (above  $E_\gamma = 50$  MeV, Fig. 3.2) we can notice that the discrepancy with experimental data is not only quantitative, but also qualitative. This starts already above  $E_\gamma = 50$  MeV and is especially pronounced at peak around 300 MeV seen in the experimental data from [51] which is not reflected in predictions. The reason of such discrepancy is most likely coming from the relativistic effects which we do not take into account within this work. It is also confirmed by the calculations in [19] where authors discuss different potentials applying to the deuteron photodisintegration. Despite authors use a much simpler potentials that used in this thesis, their predictions obtained with including some relativistic effects show, that such a peak appears in predictions.

The higher energies region is presented in order to investigate how far the predictions are from experimental results and what should be improved in the future (e.g. include relativistic part).

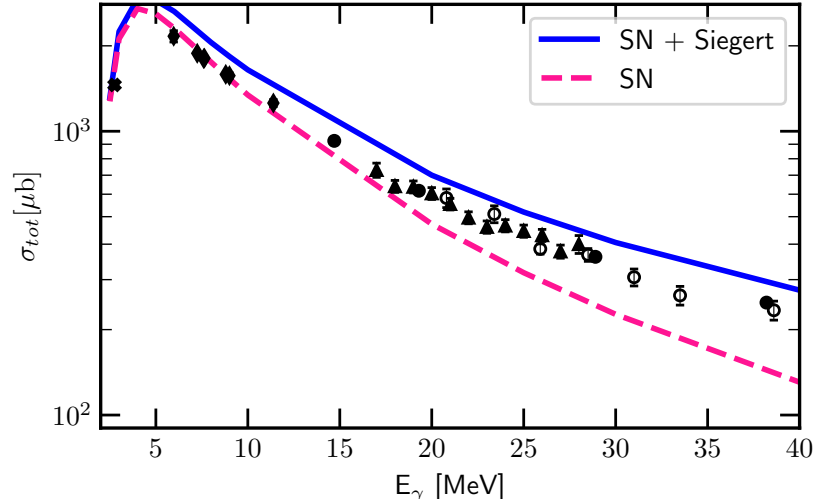


Figure 3.1: Total cross section  $\sigma_{tot}$  for the deuteron photodisintegration process as a function of the photon energy  $E_\gamma$ . Solid blue line presents results obtained with SN+Siegert and dashed pink line - predictions based on the SN current. In both cases the SMS  $N^4LO^+$   $\Lambda = 450$  MeV force is used. The experimental data are from [51] (black filled circles), [47] (empty circles), [1] (triangles), [49] (bold cross "X") and [50] (diamonds).

In Fig. 3.3 I present the total cross-section for the deuteron photodisintegration at three photon energy values: 30, 100 and 140 MeV as a function of the chiral order. Error bands show truncation errors calculated using Eq. 2.57 - 2.60. One can see that truncation

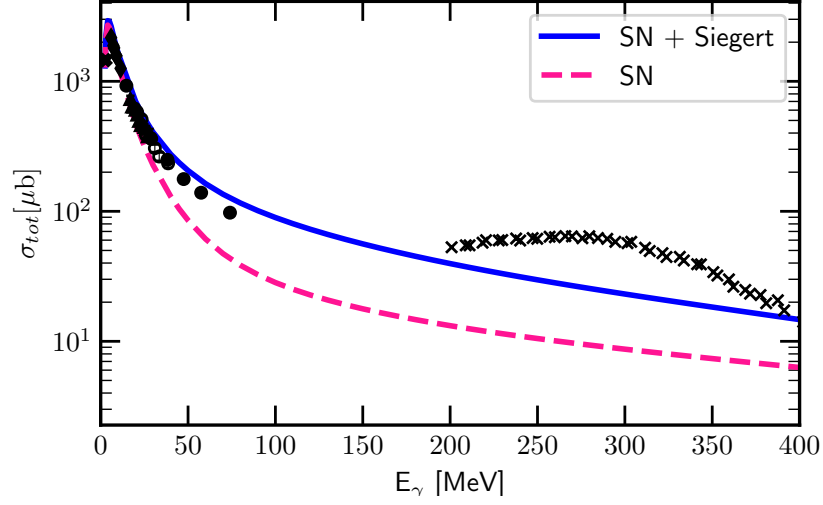


Figure 3.2: The same as in Fig. 3.2 but for the energy range 2.5 - 400 MeV. The experimental data are the same plus data above  $E_\gamma = 200$  MeV from [48] (crosses).

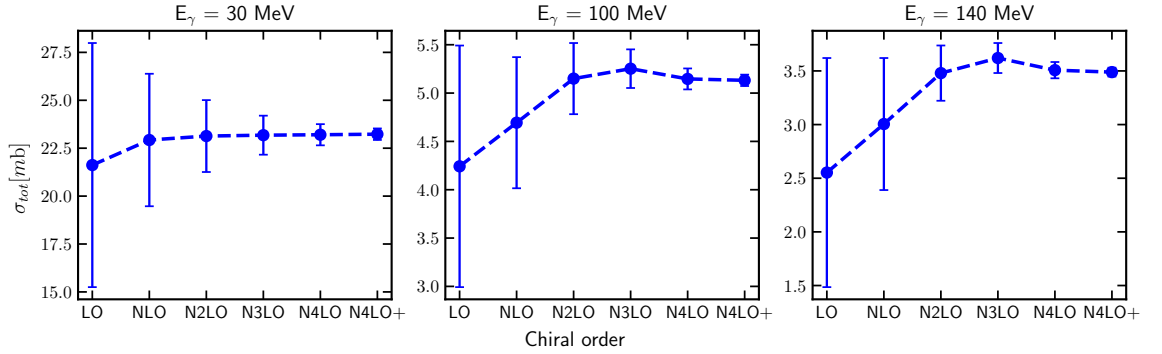


Figure 3.3: Total cross section of the deuteron photodisintegration process as a dependence on the chiral order for three photon energy  $E_\gamma$  values: 30, 100 and 140 MeV. Error bands show an estimated truncation error at each order.

errors are being reduced with each consecutive chiral order. At LO it is the biggest: 29.46 % at  $E_\gamma = 30$  MeV, 29.46 % at  $E_\gamma = 100$  MeV and 41.82 % at  $E_\gamma = 140$  MeV. At N4LO+ it is hardly visible at presented scale and amounts up to 1.3 % for each energy. For each energy the prediction is within the uncertainty range of lower orders. We see that at lower energy  $\sigma_{tot}$  already at NLO reaches value which remains practically unchanged at higher orders. Contrary, at two higher energies, contributions from higher orders are necessary to obtain stable predictions

Figures 3.4 and 3.5 show my predictions for the differential cross section  $\frac{d\sigma}{d\Omega}$ . In both figures the top, middle and bottom row shows predictions at  $E_\gamma = 30$ , 100 and 140 MeV, respectively. with 2N current's contributions taken into account via Siegert theorem. If not stated otherwise I use the SMS N<sup>4</sup>LO<sup>+</sup> potential. The left column of Fig. 3.4 shows the predictions obtained at different chiral orders (from LO to N<sup>4</sup>LO<sup>+</sup>) and with  $\Lambda = 450$  MeV. Looking at the best predictions (N<sup>4</sup>LO<sup>+</sup>,  $\Lambda = 450$  MeV) for each energy, I conclude that the higher photon energy is, the larger is difference between the theoretical

predictions and experimental data. At  $E_\gamma = 30$  MeV (top panel) my predictions almost perfectly match the data and the difference is almost always within the experimental uncertainties. Moving to  $E_\gamma = 100$  MeV (middle row) the description of the data is deteriorating: theoretical predictions still match the data qualitatively, but the gap for proton emission angle  $\theta_p$  in range ( $60^\circ < \theta_p < 130^\circ$ ) is up to 32 % (of the predicted value) and relative difference is up to 7 % (calculated with Eq. (3.1)). At the highest energy (bottom figure), it is even hard to say about good qualitative description: the general trend of the angular dependence is presented, but the predictions are far from the experimental points. We observe improvements introduced by each subsequent chiral order, but stabilization shows that some ingredients are missing.

Obtained results at each energy confirm the convergence of the predictions with respect to the chiral order. We see that the cross section at LO is far from both experimental data and the best potential's predictions ( $N^4LO^+$ ) and the higher photon energy, the larger is this difference. With each subsequent chiral order, the curves are more closer to each other and the difference between  $N^4LO$  and  $N^4LO^+$  is hardly visible at scale used in Fig. 3.3. The relative difference between these two predictions at  $E_\gamma = 30$  MeV around the point of maximum ( $\theta_p = 80^\circ$ ) is 0.05 % which is  $0.02 \frac{\mu b}{sr}$ ; at 100 MeV and  $\theta_p = 107^\circ$  it is 0.79 % ( $0.025 \frac{\mu b}{sr}$ ); and at 140 MeV (same angle) it is 1.8 % ( $0.043 \frac{\mu b}{sr}$ ). Having such a small differences between predictions from two highest chiral orders, I can conclude that predictions are converged and using NN potential at subsequent chiral orders would rather not bring large contribution to the cross section values. The difference with experimental data is rather systematic and is independent on the chiral order. The relative difference between experimental data and predictions obtained with  $N^4LO^+$  and  $\Lambda = 450$  MeV at 30 MeV is less than 13 % and absolute difference is  $< 3.07 \frac{\mu b}{sr}$ . At 100 MeV discrepancy is larger and relative difference reaches 46% with absolute difference up to  $1.39 \frac{\mu b}{sr}$ . Coming to 140 MeV the relative difference increases up to 48.6 % and absolute -  $1.93 \frac{\mu b}{sr}$ . What may be helpful for a better data description is a 2N current and relativistic correction, mentioned earlier.

Predictions obtained with the AV18 potential (dashed-dotted purple line in the Fig. 3.4 left) are very similar to these from the SMS force at lower energies (relative difference at  $E_\gamma = 30$  MeV is 0.06 % at the point of maximum -  $\theta_p = 80^\circ$ ) and with increasing energy to 140 MeV it grows to 3.1 % at the same angle. It can be connected with our potential's quality loss, but AV18 can be struggling with high energies as well. Then other components of Hamiltonian become important at that energies.

In the right column of the Fig. 3.4 I compare predictions based on various assumptions on nuclear current and dynamical mechanism. I again use SMS  $N^4LO^+$ ,  $\Lambda = 450$  MeV force. At the lowest energy predictions with plane-wave component only (without rescattering part) has relatively small deviation from the full predictions, but the difference increases at larger energies. With  $E_\gamma = 30$  MeV the relative difference is 10 % ( $4.03 \frac{\mu b}{sr}$ ) at  $\theta_p = 80^\circ$ . Difference at 100 MeV and the same angle is 4 % ( $0.21 \frac{\mu b}{sr}$ ) and at 140 MeV it is 7 % ( $0.21 \frac{\mu b}{sr}$ ). In contrast, predictions without two-body current component (1NC) have much larger gap with full prediction: the difference is 46.5 % ( $13.67 \frac{\mu b}{sr}$ ) at 30 MeV, 78.6 % ( $2.88 \frac{\mu b}{sr}$ ) at 100 MeV and 77.8 % ( $1.68 \frac{\mu b}{sr}$ ) at 140 MeV at the same  $\theta_p = 80^\circ$ . Obviously 2NC contributions are extremely important in this case, the difference connected with 2NC contributions is much higher than theoretical errors or even rescattering contribution. For other scattering angles, especially  $\theta_p = 0^\circ$  or  $\theta_p = 180^\circ$ , the role of two-body current or FSI is even more pronounced.

The Fig. 3.5 (left) presents theoretical truncation uncertainties. That confirms our

expectations that for the regarded photo reaction chiral order  $N^4LO^+$  is able to produce converged predictions: the black band is hardly visible for the  $E_\gamma = 30$  MeV (the relative error for  $N^4LO^+$  at  $80^\circ$  is only 0.12 %) and is also quite narrow for larger energies (at 140 MeV the error at the same angle is 1.46 %). At the lower chiral orders, this band is obviously much wider: at  $N^2LO$  it is 1.25 % at  $E_\gamma = 30$  MeV and 15.0 % at  $E_\gamma = 140$  MeV.

Finally, Fig. 3.5 (right) presents a cutoff dependence of the differential cross section. The ideal case is when the dependency is so weak that the choice of the parameter  $\Lambda$  would not make significant changes. In practice the choice of this parameter can be important as it makes a noticeable difference in prediction at higher energies. Namely, while on the top of Fig. 3.5 ( $E_\gamma = 30$  MeV) the cutoff dependence is so tiny, that, in fact, all the lines (for different  $\Lambda$  values) overlap each other and we cannot distinguish them with the naked eye: the relative difference at maximum is 0.08 %. This is approximately  $\frac{2}{3}$  smaller than truncation error discussed above. However, with increasing photon energy up to 100 MeV and 140 MeV (middle and bottom rows of the right column of Fig. 3.5) the spread becomes bigger: the uncertainty related to the  $\Lambda$ -dependence is 3.35 % at 100 MeV and 5.66 % at 140 MeV (the same  $\theta_p$ ). Thus at two higher energies the cut-off dependence becomes more important than truncation errors. That shows, that proper choice of the  $\Lambda$  is important. However, if I restrict myself to  $\Lambda = 450$  MeV and 500 MeV, the dependence drops to 1.98 % at  $E_\gamma = 140$  MeV.

On the Fig. 2.3 we saw that the total cross section for the same energies has the cutoff spread around 4.5 % for 100 MeV and 8 % for 140 MeV. For  $E_\gamma = 30$  MeV it is below 1 %.

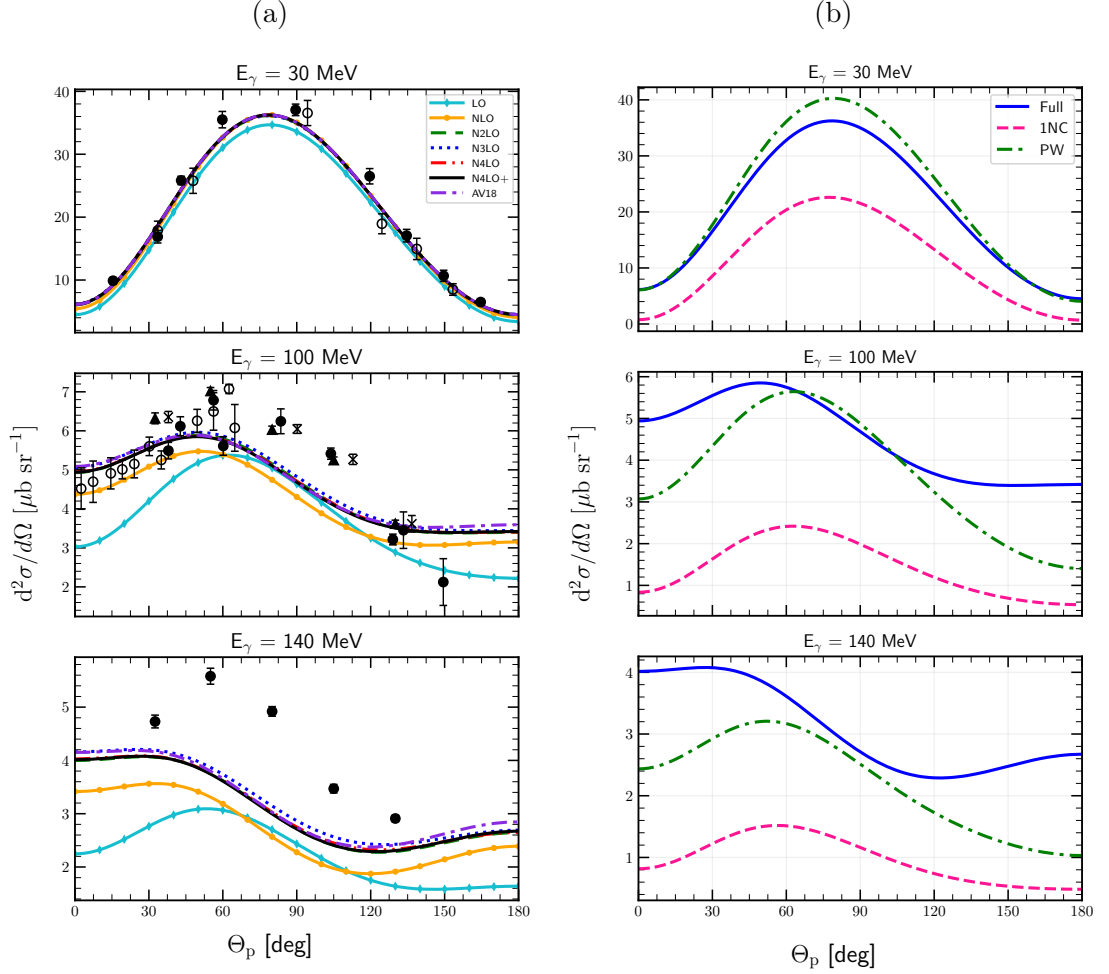


Figure 3.4: Differential cross section  $\frac{d^2\sigma}{d\Omega}$  as a function of the outgoing proton momentum polar angle  $\theta_p$  in the center of mass frame for the photon energy 30 MeV (top), 100 MeV (middle) and 140 MeV (bottom). **(a)** Results obtained using the SMS potential at different chiral orders (from LO to  $N^4\text{LO}^+$ ) with the cutoff parameter  $\Lambda = 450$  MeV and 2NC contributions taking via the Siegert theorem. For the sake of comparison, predictions obtained with the AV18 potential are shown by dashed-dotted purple line. Data points (filled and empty circles) are from [53] for  $E_\gamma = 30$  and 100 MeV and [54] for  $E_\gamma = 140$  MeV. **(b)** Predictions obtained with the chiral  $N^4\text{LO}^+$  potential and  $\Lambda = 450$  MeV with various models of nuclear current(1N and 2N) and scattering state. The blue solid curve is plane-wave plus rescattering parts, 1NC + Siegert(the same as  $N^4\text{LO}^+$  line in (a)). The pink dashed curve shows predictions obtained with the single-nucleon current only (without applying the Siegert theorem) and the green dashed-dotted curve represents predictions with the full current(1N + Siegert) but plane-wave part only.

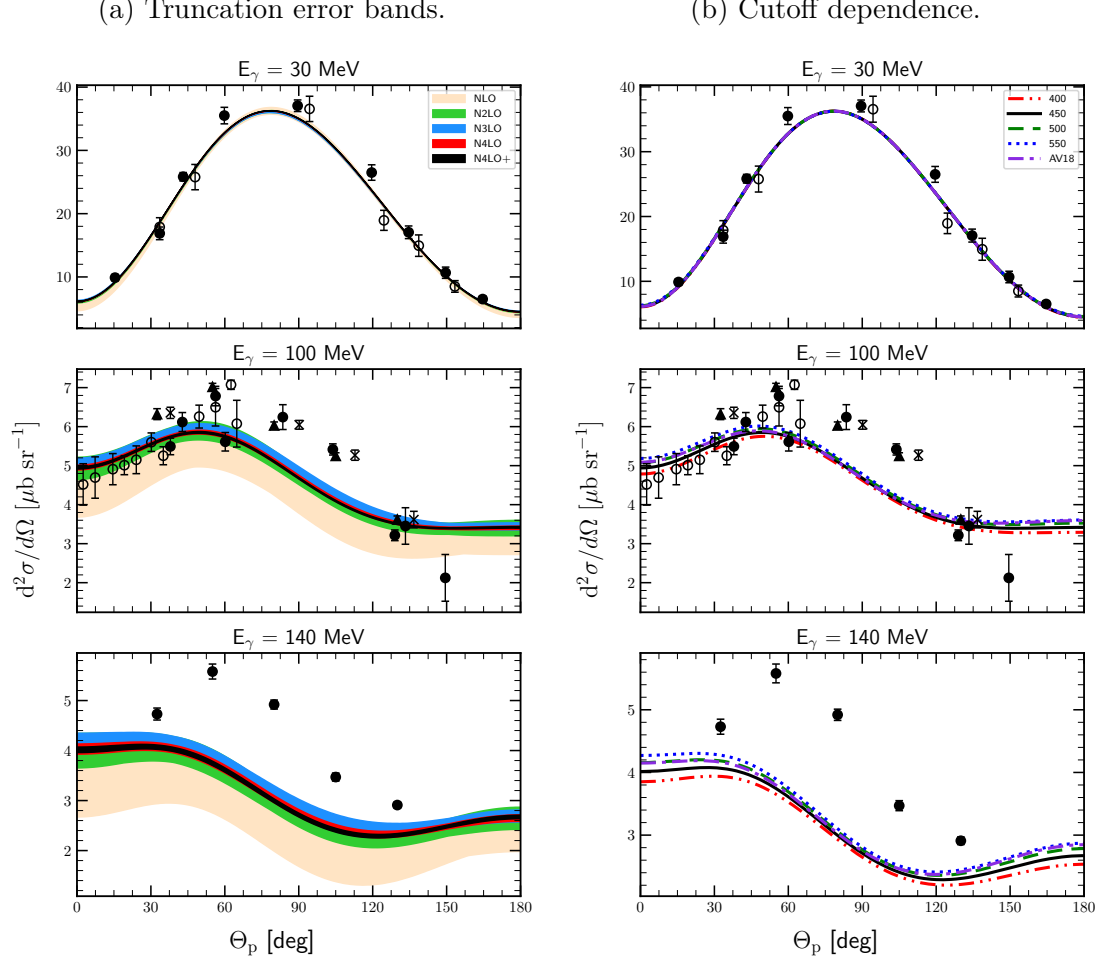


Figure 3.5: Theoretical uncertainties for the differential cross section  $\frac{d^2\sigma}{d\Omega}$  as a function of the outgoing proton's momentum polar angle  $\theta_p$  in the center of mass frame for the photon energy is 30 MeV (top row), 100 MeV (middle row) and 140 MeV (bottom row). **(a)** The truncation error bands for each energy in a corresponding row. Results are obtained using the SMS potential at different chiral orders (from NLO to  $N^4\text{LO}^+$ ) with the cutoff parameter  $\Lambda = 450$  MeV and 2NC contributions taking via the Siegert approach. **(b)** Predictions obtained using different values of the cutoff parameter  $\Lambda$ . The double-dotted-dashed red curve, the solid black line, the dashed green line and the dotted blue line represent predictions obtained with  $\Lambda = 400, 450, 500$  and  $550$  MeV respectively and the chiral potential  $N^4\text{LO}^+$ . Data points are the same as in Fig. 3.4a



### 3.1.2 Polarisation observables

In this subsection I will present my predictions for selected polarisation observables. I start with deuteron vector  $iT_{11}$  and tensor  $T_{20}$ ,  $T_{21}$  and  $T_{22}$  analyzing power, which are defined as [19]:

$$iT_{11}(\theta) = -2 \frac{\text{Im } V_{11}}{V_{00}}, \quad (3.2)$$

$$T_{2i}(\theta) = \frac{(2 - \delta_{i0}) \text{Re } V_{2i}}{V_{00}}, i = 0, 1, 2, \quad (3.3)$$

where  $V_{ij}$  is *??? all derivation?*.

in the Figures 3.6 (a, b) and 3.7(a,b) I show my predictions at  $E_\gamma = 30$  MeV, for the  $T_{20}$ ,  $T_{21}$ ,  $T_{22}$  and  $iT_{11}$  respectively as functions of the outgoing proton angle  $\theta_p$  in the centre of the mass (CM) frame. Each of them is organized in the similar way: the top panel shows a dependence of the predictions on the chiral order of the potential. The middle subfigure is showing a correspondent truncation error for each of the predictions from a top row (excepting LO, because its uncertainty is too large and will make the readability worse). The last (bottom) panel shows the cutoff dependence at the chiral order  $N^4\text{LO}^+$ .

All the analyzing powers presented here show excellent convergence upon a chiral order as it is hard to distinguish the predictions from each subsequent order starting from the  $N^2\text{LO}$ . The relative width of  $N^4\text{LO}^+$  truncation band for  $T_{20}$ ,  $T_{21}$  and  $T_{22}$  are 0.06 %, 0.05 % and 0.19 % respectively (at  $\theta_p = 90^\circ$ ,  $60^\circ$  and  $90^\circ$  respectively). The slowest convergence is observed for  $iT_{11}$  (Fig. 3.7b) where we can recognize  $N^2\text{LO}$  band. Still at  $N^4\text{LO}^+$  it has only a 0.2 % width truncation band at  $\theta_p = 20^\circ$  (maximum point). The cutoff dependency for all regarded observables is weak and predictions for each value of the  $\Lambda$  are hardly separable with the naked eye. The relative spread of the predictions based on various  $\Lambda$  at the same angles as above are 0.87 %, 0.94 %, 3.42 % and 0.68 % for  $T_{20}$ ,  $T_{21}$ ,  $T_{22}$  and  $iT_{11}$ , respectively.

Predictions for the photon energy  $E_\gamma = 100$  MeV (Figs. 3.8 and 3.9) preserve similar trends for each observable. Generally, predictions are being converged starting even from the  $N^2\text{LO}$  while for  $iT_{11}$  we can see that truncation error's bands are noticeably wide even at  $N^4\text{LO}$  and  $N^4\text{LO}^+$ . Cutoff dependence at this energy is a bit stronger compared to those at  $E_\gamma = 30$  MeV, especially for  $T_{22}$  and  $iT_{11}$  analyzing powers (Fig. 3.7), where one can see slightly stronger discrepancy at the stationary points.

Looking at the predictions for the deuteron tensor analyzing powers, we can conclude that cutoff dependence is generally weak and the choice of  $\Lambda$  does not affect predictions much even at that higher energy: the relative spread among all cutoffs for  $T_{20}$  is 1.54 % around the point of maximum ( $\theta_p = 90^\circ$ ). For other components of the tensor analyzing power spread is: 0.14 % at  $\theta_p = 60^\circ$  for  $T_{21}$ ; 3.68 % at  $\theta_p = 90^\circ$  for  $T_{22}$ ; and for  $iT_{11}$ : 4.91 % at  $\theta_p = 75^\circ$ . We see again that  $iT_{11}$  has much larger spread in the maximum and is more sensitive to the cutoff choice.

Turning our attraction to the chiral order convergence, we can observe that predictions are mostly converged after  $N^2\text{LO}$  or  $N^3\text{LO}$ . The relative width of  $N^4\text{LO}^+$  truncation band for  $T_{20}$ ,  $T_{21}$  and  $T_{22}$  are 0.7 %, 0.7 % and 0.04 % respectively (at the same angles as used above). Another case is  $iT_{11}$ , for which this width is much larger: 6.8 % at  $\theta_p = 20^\circ$ . The truncation uncertainty for all analyzing powers is much lower than one, connected to the



choice of cutoff parameter. Although,  $iT_{11}$  seems to be more sensitive both to the choice of the cutoff parameter and to the chiral order than other regarded observables. But even for  $iT_{11}$  cutoff spread is almost twice larger than truncation error's band. Standing out of other tensor components,  $iT_{11}$  can be useful for the investigation of the cutoff dependence of the model. Of course, we can repeat once more that our model is less accurate at higher energies which is reflected in a stronger cutoff dependence and slower chiral convergence. However we conclude that even at these energies tensor analyzing powers are converged with respect to the chiral order.

Comparison of the predictions obtained using the chiral  $N^4LO^+$  potential  $\Lambda = 450$  MeV with ones obtained taking AV18 potential show a very good agreement: the relative difference at  $E_\gamma = 30$  MeV is below 6 % for regarded tensor analyzing powers at specified angles. And at  $E_\gamma = 100$  MeV it is even better: the difference does not exceed 4 %.

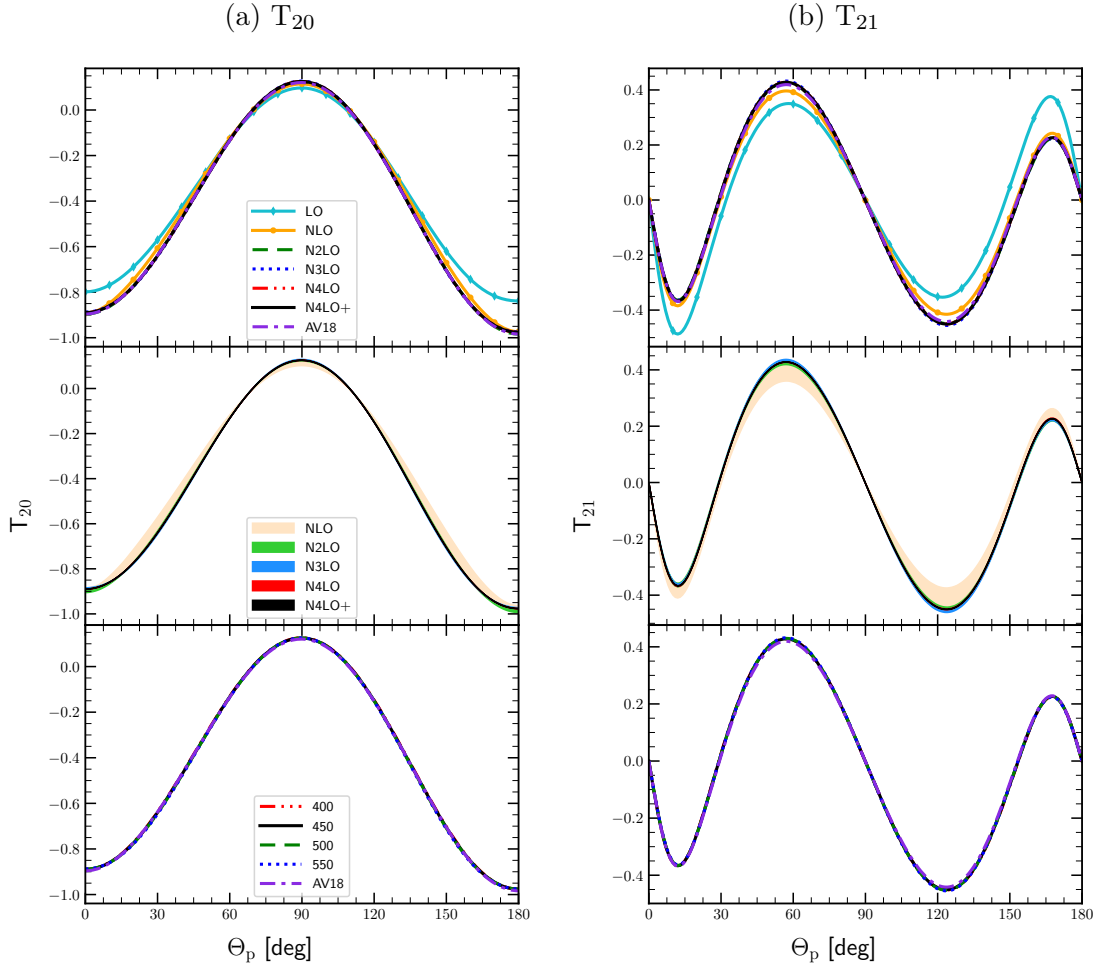


Figure 3.6: Tensor analyzing powers  $T_{20}$  (a) and  $T_{21}$  (b) as a function of the outgoing proton angle  $\theta_p$  in CM frame for the photon energy  $E_\gamma = 30$  MeV. Top row presents results obtained using potential with different chiral orders (from LO to  $N^4LO^+$ ) with cutoff parameter  $\Lambda = 450$  MeV. The middle row shows truncation errors for each chiral order starting from NLO and the bottom row presents a cutoff dependency at  $N^4LO^+$ . For the sake of comparison, predictions obtained with the AV18 potential are given as well.

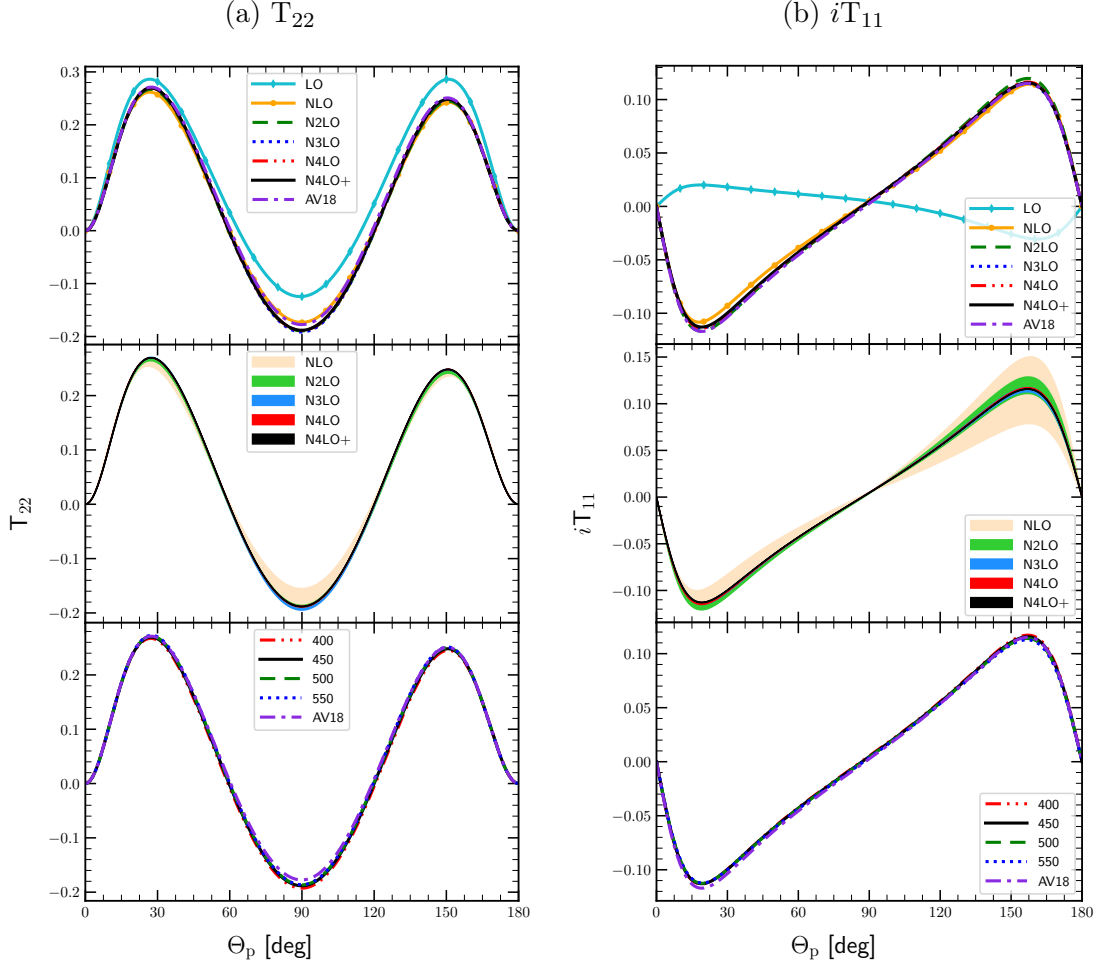


Figure 3.7: The same as in Fig. 3.6 but for the deuteron tensor analyzing power  $T_{22}$  (subfigure (a)) and the deuteron vector analyzing power  $iT_{11}$  (subfigure (b)).

In Fig. 3.10 together with our most advanced "Full" predictions at  $E_\gamma = 30$  MeV ( $N^4LO^+$ ,  $\Lambda = 450$  MeV, the Siegert theorem), I show predictions obtained with 1NC only and the Siegert predictions with plane-wave contribution without rescattering part. In the case of deuteron's tensor analyzing power components, the contribution of rescattering part is important for  $T_{20}$ ,  $T_{21}$  and  $T_{22}$  (the relative difference is up to 20 % in extremum points). and crucial for  $iT_{11}$  where the PW part equals to zero. The 2NC component taken into account via Siegert theorem has a dominant contribution here. We see that 1NC predictions are absolutely away from the "Full" predictions and in case of  $iT_{11}$  does not even reflect complete prediction qualitatively.

Fig. 3.11 presents similar results but for  $E_\gamma = 100$  MeV and it is interesting that difference between Full and 1NC prediction becomes smaller and it is especially visible for  $T_{22}$ . At this energy the relative difference between "Full" and 1NC predictions at  $\theta_p = 90^\circ$  is 43.6 % comparing to 122.8 % at  $E_\gamma = 30$  MeV. Similarly, the difference for  $T_{20}$  at  $E_\gamma = 30$  MeV ( $\theta_p = 90^\circ$ ) is 91.4 % and at  $E_\gamma = 100$  MeV it drops to 28.8 %. This trend is noticeable looking also on results presented below.

In the next figures, I will compare my predictions with experimental data. I will keep a similar way as it was done in [52] where due to experimental conditions results are given not at single photon energy, but for a specific ranges of  $E_\gamma$ . In the Figures

3.12 - 3.18 I show an angular dependence of the  $T_{2i}$  ( $i = 0, 1, 2$ ) for a specific energy bands: 25–45 MeV, 45–70 MeV, 70–100 MeV, and 230–330 MeV. Solid blue line shows an average value of the observable in the specified energy intervals: obtained at  $N^4\text{LO}^+$  with  $\Lambda = 450$  MeV, while the pink dashed line is a prediction obtained with a same setup but without using a contributions from Siegert approach (single nucleon current only). Bands for each of prediction specify the spread of predictions due to the energy band.

One clearly sees that the data description is better for the predictions with Siegert contributions and SN current alone is not able to describe experiment properly. With increasing energy (above 100 MeV), the difference between predicted values and experimental data becomes larger (especially for  $T_{22}$ ), which shows a necessity of improving theoretical model before applying it to higher energies. Nevertheless, even with approximations used, the data description remains reasonable. We that quite often and in particular in Fig. 3.17 and Fig. 3.18 the data description is worse for smaller angles. Especially for the tensor analyzing power  $T_{22}$  the group of data point lying closer to  $\theta_p = 30^\circ$  are farther from the theoretical prediction than second group. In Fig. 3.18 the description of data points for  $T_{20}$  seem to be better with SN current (dashed line), but in this case it is only accidental match as we do not observe similar trend for any other angular span or for different observable.

In the Figure 3.19 the energy dependence of  $T_{20}$  and  $T_{22}$  is presented for the energy range 0–400 MeV. Beside my predictions I also demonstrate the experimental data from [52] and [55] as well as theoretical calculations from [56]. For  $T_{20}$  all models are able to describe experimental data well even for high energies. On the other hand,  $T_{22}$  is not described so well: for the energies below 140 MeV the predictions are within uncertainties of experimental data, but further the difference with the data increases. Above 140 MeV my "Full" predictions do not reflect the qualitative nature of the data. Namely, I observe that data points start ascending which is not represented in my predictions. Theoretical predictions from [56] (brown dashed curve) are also not able to describe data quantitatively for  $T_{22}$ , but increasing of  $T_{22}$  towards data is present. The calculation predictions in [56] are obtained with a one-body current using the Bonn OBEPR NN potential with the major part of meson exchange currents (MEC) included implicitly via the Siegert operators plus explicit pion exchange currents (MEC), isobar configurations (IC) and the leading order relativistic corrections (RC). So authors use a different potential, but probably the main difference of predictions is coming from the RC included there.

Similar picture is seen in the Figures 3.20 and 3.21 where I show an energy dependence of the mean of deuteron analyzing powers over specific angular ranges (following the data from [52]). In Fig. 3.20 we see that only predictions for  $T_{20}$  are able to reflect the experimental results, while for  $T_{21}$  and  $T_{22}$  predictions are reasonable (quantitative-wise) only for lower energies and difference with data becomes larger when energy increases. Predictions for  $T_{21}$  and  $T_{22}$  once more confirm an insufficiency of SN and an importance of 2-nucleon current contributions. The description is better for larger angles Fig. 3.21: at lower energies (below 140 MeV) the correspondance to experimental data is good for all three observables, but above that threshold, all predictions (especially for  $T_{22}$ ) move away from the measurements data.

In the Fig. 3.22 I demonstrate predictions for the photon asymmetry  $\Sigma_\gamma$  for the deuteron photodisintegration with  $E_\gamma = 20$  MeV (a) and 60 MeV (b) together with experimental data of [57–60]. Both (a) and (b) figures are organized similarly to the figures I showed above for the tensor analyzing powers (e.g. Fig. 3.7). That is the top panel is aimed to demonstrate predictions obtained with the chiral SMS potential at different or-

ders of the chiral expansion, the middle one is showing a truncation errors and the bottom one shows the cutoff dependence. For that observable we see a good convergence with respect to the chiral order. For both regarded energies predictions at different orders are very close to each other except the LO and NLO curves. Nevertheless, at  $E_\gamma = 60$  MeV the truncation error bands reveal some uncertainty connected with the chiral order and it is expected that even some higher chiral orders would still contribute to the predictions at this energy. The relative width of the truncation band are 0.26 %, 5.04 %, 5.05 %, 5.73 % and 14.96 % for  $N^4\text{LO}^+$ ,  $N^4\text{LO}$ ,  $N^3\text{LO}$ ,  $N^2\text{LO}$  and NLO respectively and at  $\theta_p = 90^\circ$ .

The cutoff dependence is also much stronger at 60 MeV. One clearly sees that predictions are different for various values of the  $\Lambda$ . The relative difference between predictions to the cutoff parameter at 20 MeV is 0.26 % while at the photon energy 60 MeV it is 4.41 % (both calculated at  $\theta_p = 90^\circ$ ).

Regarding the correspondence to experimental data, we observe that for the lower energy predictions are almost perfectly overlapping with experimental points within the error bars. For far data point our predictions are outside data error bars, but they are still within  $3\sigma$  range. For 60 MeV, experimental data points are systematically below theoretical curves, especially in the middle of angles range. It seems that some systematic uncertainty is presented in predictions and ad hoc multiplication by some factor (around 0.8) could help predictions be more similar to experimental data. But, of course, the observed discrepancy points to simplified character of the model used here.

In the Fig. 3.23 I present a dependence of the photon asymmetry  $\Sigma_\gamma$  on the photon energy at a fixed value of the outgoing proton polar direction  $\theta_p = 90^\circ$  (following the data given at [61] and [58]). It is noticeable that with increasing energy, the predictions are above the experimental data and the discrepancy grows with energy. This trend was also observed in the angular dependence of the asymmetry at 60 MeV so I conclude that within our framework,  $\Sigma_\gamma$  is sensitive to the initial photon energy and some theoretical contributions are missing in order to get satisfactory predictions at higher energies. From the Fig. 3.23 we can say that large discrepancy with data starts already above  $E_\gamma = 35$  MeV. <sup>1</sup>

The proton polarization is demonstrated in Fig. 3.24 for the photon energy 30 MeV(a) and 100 MeV(b). In this case even higher energy such as 100 MeV does not reveal neither slower convergence with respect to the chiral order nor stronger cutoff dependence. Figures for both energies show that only next-to-leading order brings relatively high contribution while taking into account other subsequent orders does not change predictions significantly. In the case of cutoff dependence, we see that curves for each value of  $\Lambda$  are very close to each other. The relative difference of the predictions with respect to the cutoff parameter is 4.04 % at the minimum point  $\theta_p = 130^\circ$  of  $E_\gamma = 30$  MeV and 5.62 % at  $\theta_p = 160^\circ$  and  $E_\gamma = 100$  MeV. The dependence is slightly stronger for higher energy, but both values are comparable.

Predictions for the neutron polarization at the energies 2.75 MeV and 100 MeV are shown in the Fig. 3.25. The choice of energy is conditioned by the availability of experimental data, which were taken in 1965 at Livermore [62] and in 1986 at TRIUMF facility [63]. In the case of  $E_\gamma = 2.75$  MeV (Fig. 3.25a), we see that predictions reflect the behavior of experimental data points qualitatively, having more or less a constant offset of the values. Similar offset was obtained also in [19], where various approaches were presented. Authors compare different models which have a very similar theoretical results

---

<sup>1</sup>It is worth to note that data of [58] are above these from [61] (however still inside  $3\sigma$  experimental error bands) and remain in agreement with my predictions even at  $E_\gamma = 60$  MeV.

eventhough different potentials are used with and without relativistic correction. One of the theoretical predictions is included even in the experimental papers [62] and authors state that there might be systematic error in the calibration of the analyzing power of the neutron polarimeter which could affect experimental results precision. Interesting is that predictions clearly show symmetrical form of the curve, while in the experimental data have some deviations from symmetrical form. It can be a sign that some problem with data can be in this case (taking into account also that experiment had been done in 1965) as well as approximations in theoretical models. Even in [62] authors make a plot of theoretical curve multiplied by the factor 0.879 wich is almost perfectly overlaps with experimental data afterwards.

At the energy  $E_\gamma = 100$  MeV (Fig. 3.25b), the difference with experimental data does not look like a systematic shift and deviations look like random. For most of data points, predicted values are within error bars and only some of points (e.g. around  $50^\circ$ ) have prediction in distance more than one standard deviation. Nevertheless, these data points look like being out of general trend and may be a result of unprecise measurement.

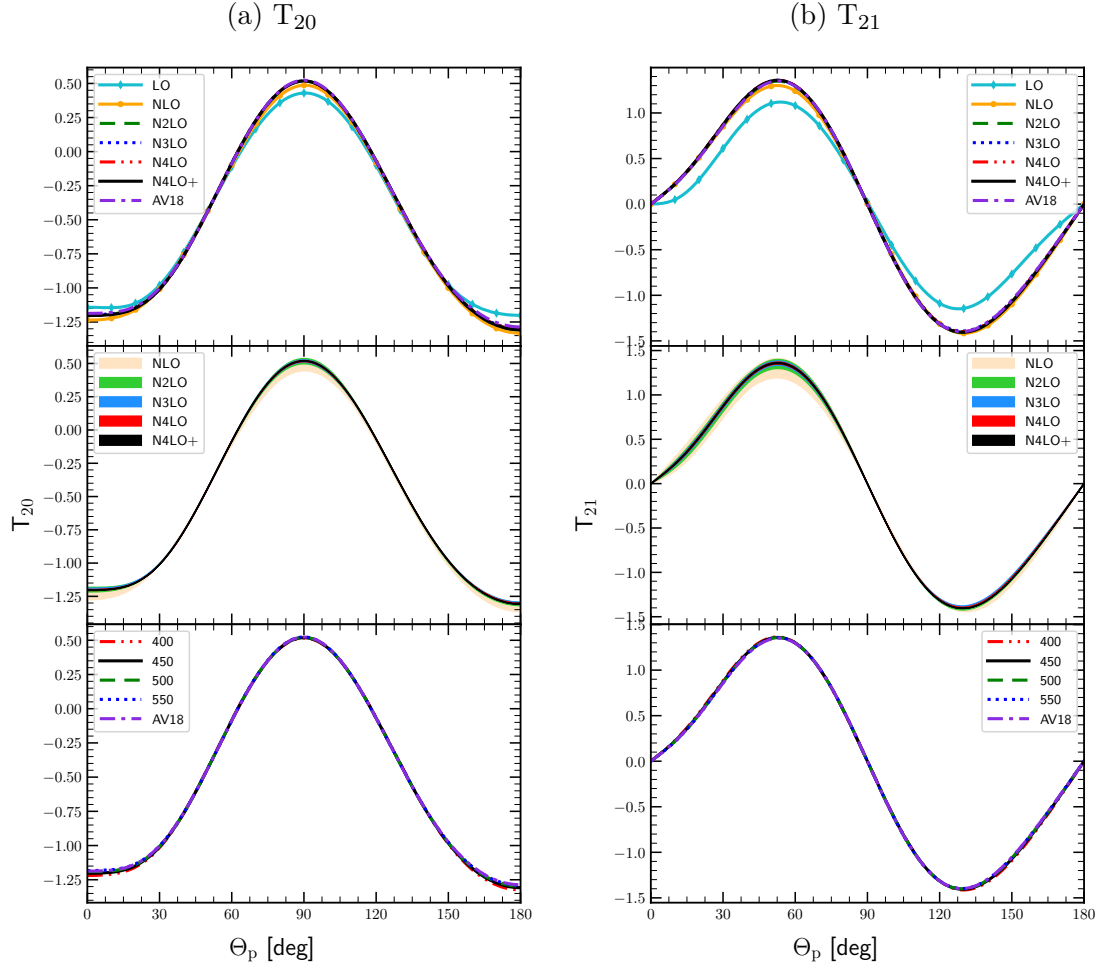


Figure 3.8: The deuteron tensor analyzing powers  $T_{20}$  (a) and  $T_{21}$  (b) as a function of the outgoing proton angle  $\theta_p$  in the center of mass frame for the photon energy  $E_\gamma = 100$  MeV. Top row presents results obtained using potential with different chiral orders (from LO to  $N^4\text{LO}^+$ ) with cutoff parameter  $\Lambda = 450$  MeV. The middle row shows truncation errors for each chiral order starting from NLO and the bottom row presents a cutoff dependency at  $N^4\text{LO}^+$ . For the sake of comparison, predictions obtained with the AV18 potential are given as well.

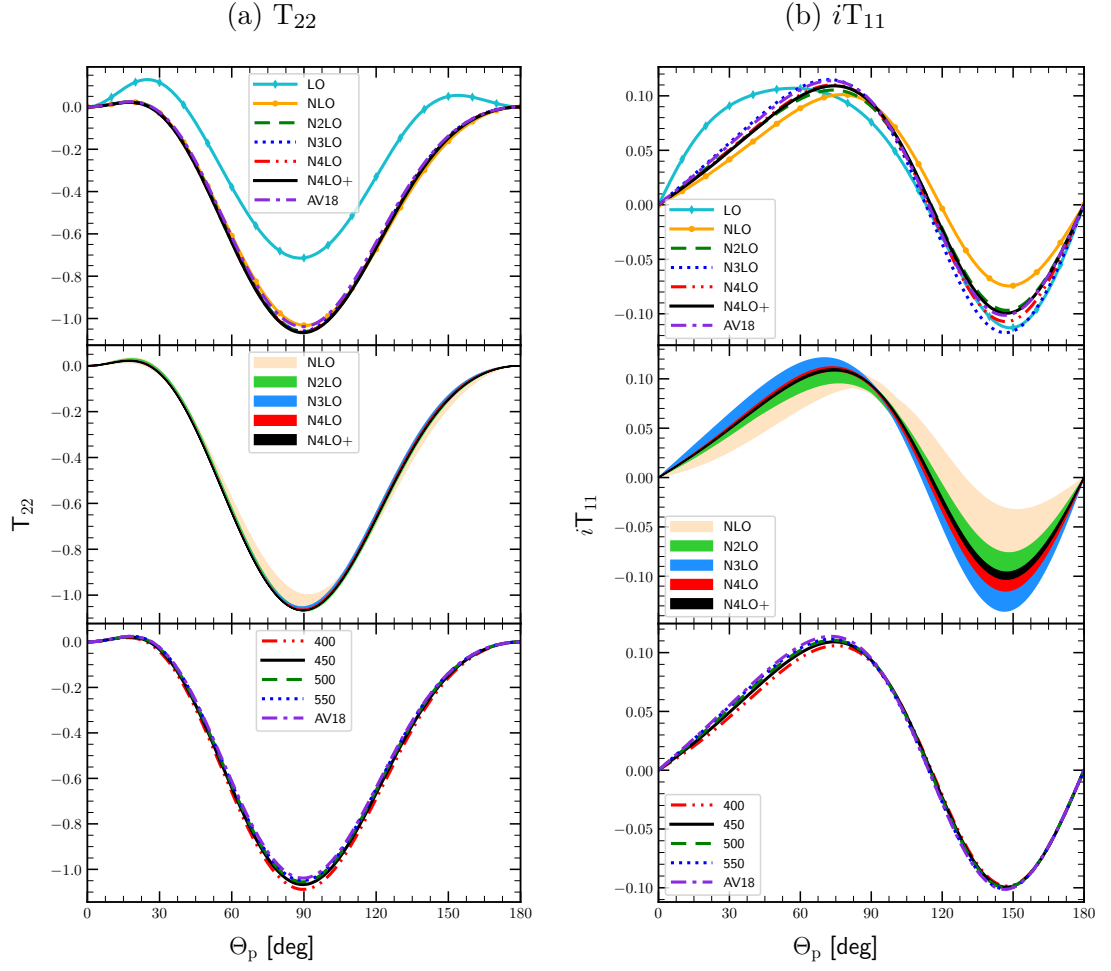


Figure 3.9: The same as in Fig. 3.8 but for the deuteron tensor analyzing power  $T_{22}$  (subfigures (a)) and deuteron vector analyzing power  $iT_{11}$  (subfigures (b)).

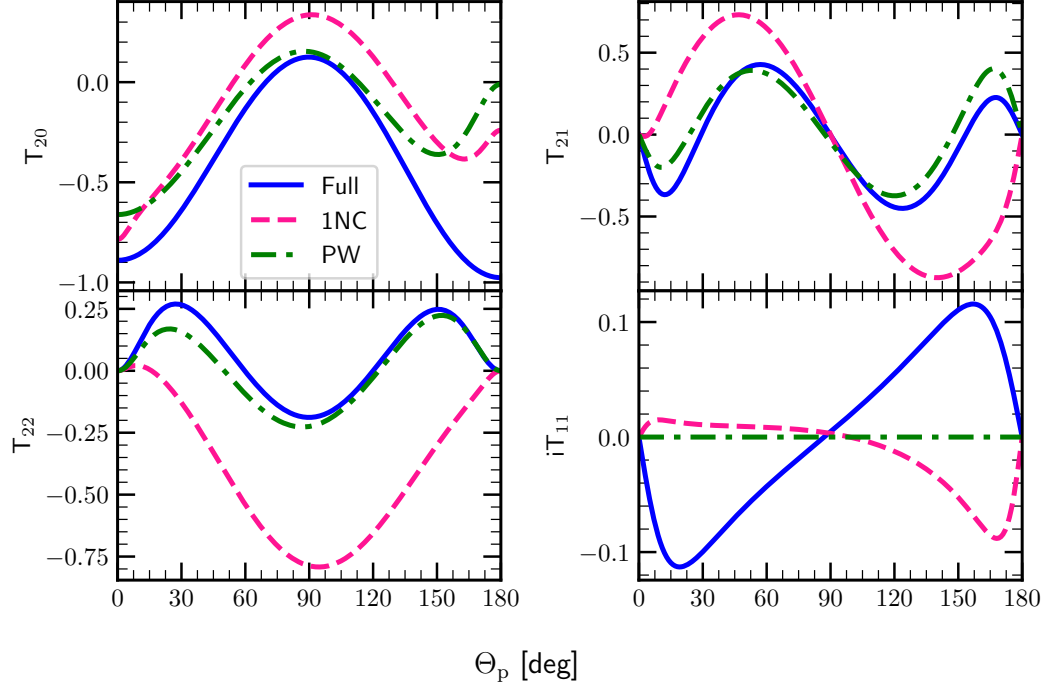


Figure 3.10: The deuteron tensor analyzing powers  $T_{20}$ ,  $T_{21}$ ,  $T_{22}$  and the vector analyzing power  $iT_{11}$  as a function of the outgoing proton angle  $\theta_p$  in the CM frame at  $E_\gamma = 30$  MeV. Similarly to Fig. 3.4b predictions obtained with chiral  $N^4\text{LO}^+$  potential and  $\Lambda = 450$  MeV are presented for three models. Blue solid line is the most complete prediction we have (plane-wave plus rescattering parts, 1NC + Siegert), pink dashed line shows predictions obtained with single-nucleon current only (without Siegert contributions) and green dashed-dotted line is a prediction in which we neglect the rescattering part and stick to the plane-wave part only.



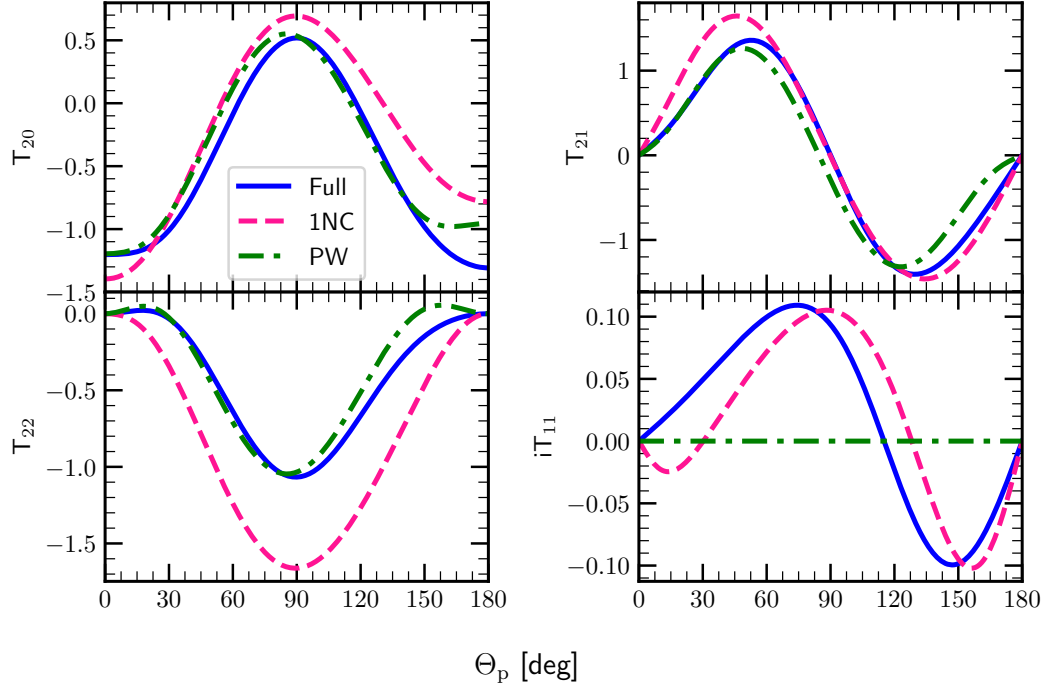
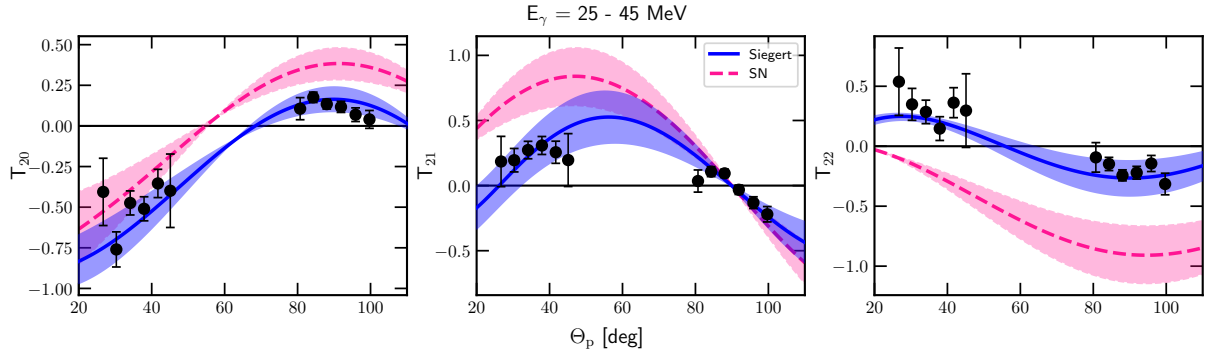

 Figure 3.11: The same as in Fig. 3.10 but for  $E_\gamma = 100$  MeV


Figure 3.12: Tensor analyzing powers  $T_{20}$ ,  $T_{21}$  and  $T_{22}$  as a function of the outgoing proton angle  $\theta_p$  in the CM frame. Solid blue line is a mean value of my predictions obtained at energy values from 25 to 45 MeV with the SMS potential at  $N^4\text{LO}^+$  chiral order and with  $\Lambda = 450$  MeV and with SN current used together with the Siegert approach. Pink dashed line is similar prediction but with SN only. The corresponding bands show the limits of predictions in the regarded energy region. Filled circles are experimental data from [52] for the same energy span.

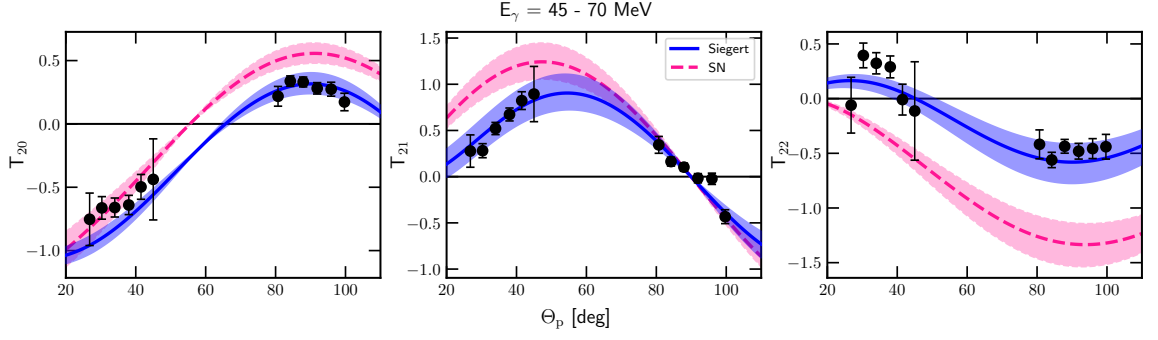


Figure 3.13: The same as in Fig. 3.12 but for energy bin 45 – 70 MeV.

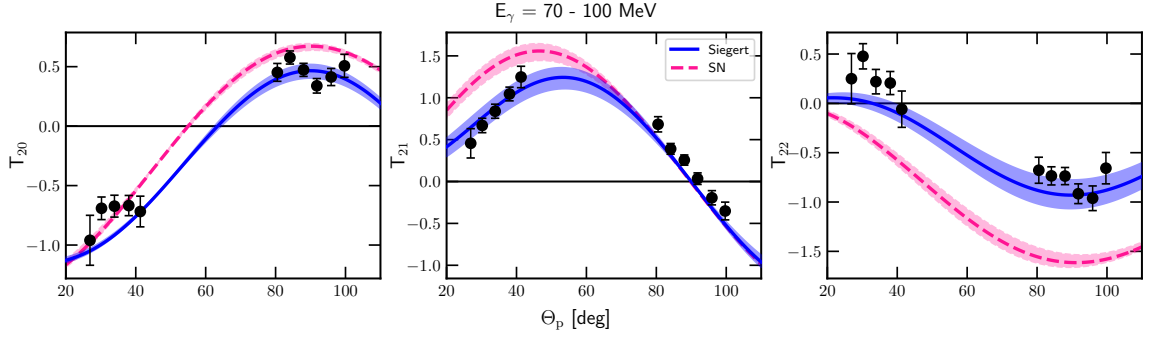


Figure 3.14: The same as in Fig. 3.12 but for energy bin 70 – 100 MeV.

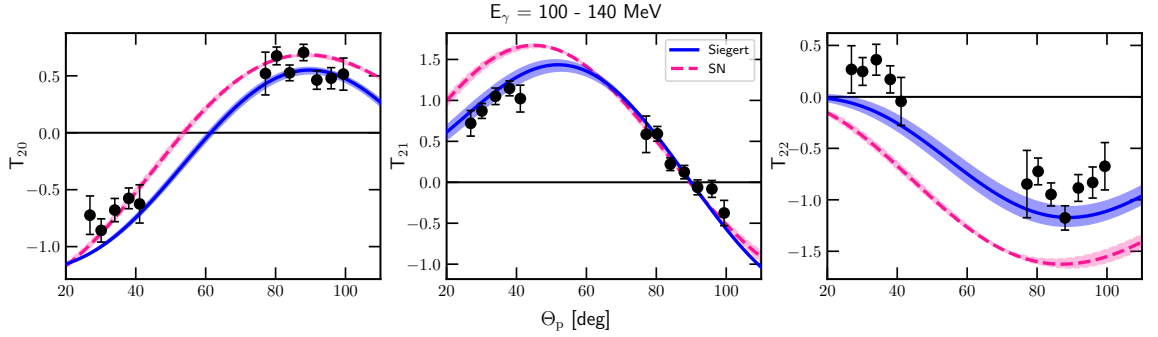


Figure 3.15: The same as in Fig. 3.12 but for energy bin 100 – 140 MeV.

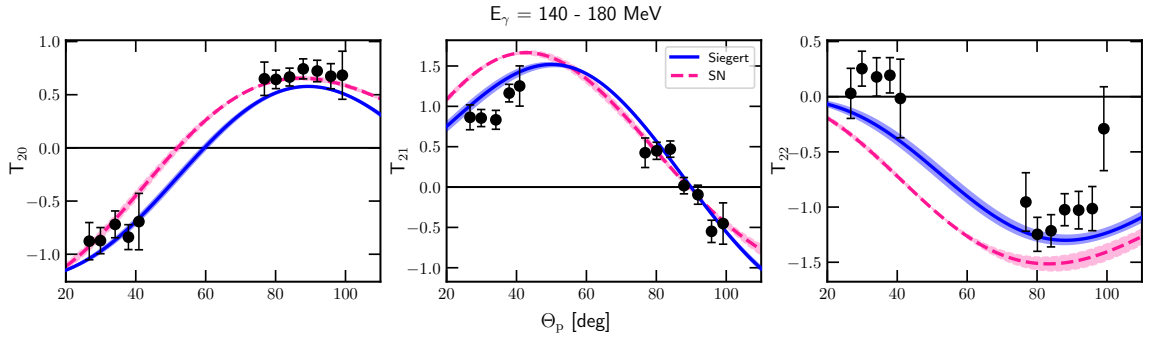


Figure 3.16: The same as in Fig. 3.12 but for energy bin 140 – 180 MeV

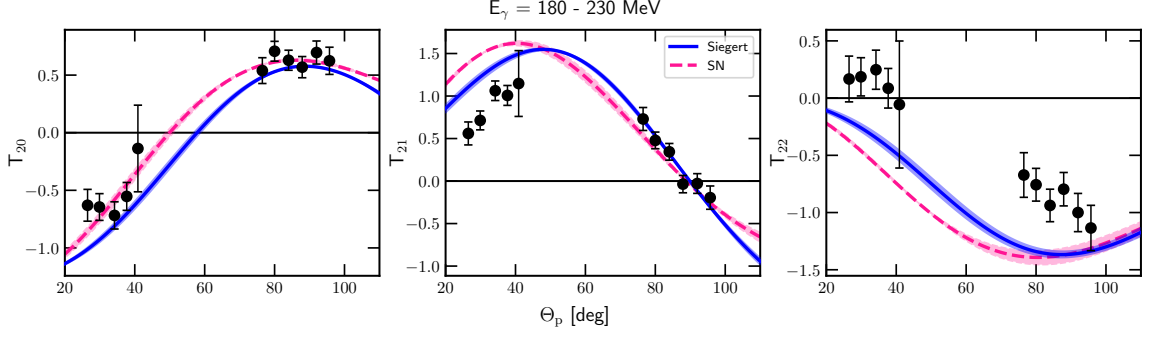


Figure 3.17: The same as in Fig. 3.12 but for energy bin 180 – 230 MeV

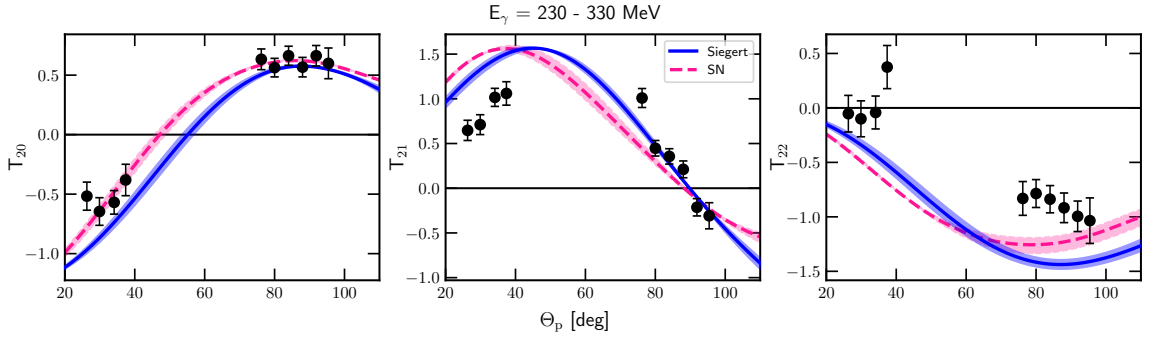


Figure 3.18: The same as in Fig. 3.12 but for energy bin 230 – 330 MeV

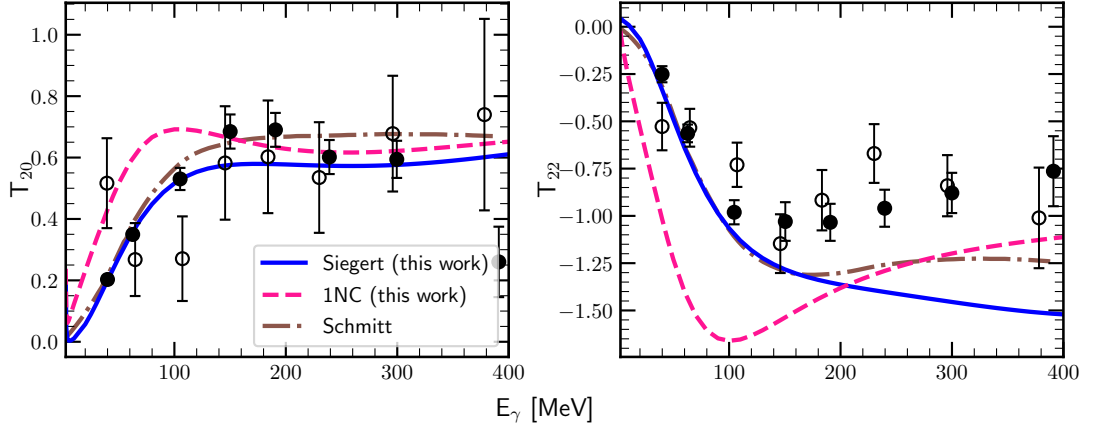


Figure 3.19: The tensor analyzing powers  $T_{20}$  and  $T_{22}$  as a function of the photon energy  $E_\gamma$  at fixed outgoing proton angle  $\theta_p = 88^\circ$  in the center of mass frame. My predictions (blue solid line) are obtained with the SMS potential at the chiral order  $N^4\text{LO}^+$ , with the cutoff parameter  $\Lambda = 450$  MeV and with 2NC contributions included via the Siegert theorem. The dashed pink curve shows predictions obtained with the same interaction, but without 2NC contributions. The dashed-dotted brown curve presents theoretical results from [56]. Experimental data is taken from [52] (filled circles) and [55] (empty circles).

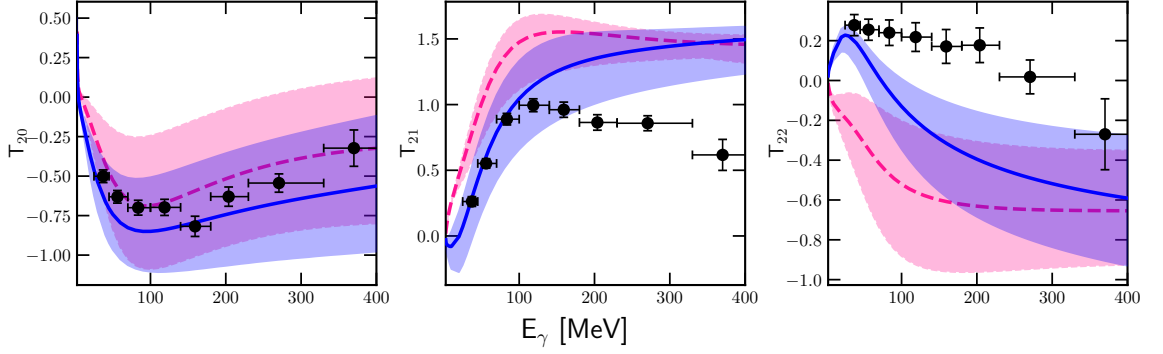


Figure 3.20: The tensor analyzing powers  $T_{20}$ ,  $T_{21}$  and  $T_{22}$  as a function of the photon energy within the outgoing proton momentum polar angle  $\theta_p$  range  $24^\circ - 48^\circ$  in the center of mass frame. The solid blue curve is a mean value of my predictions at energy values from 25 to 45 MeV obtained with the SMS potential at  $N^4\text{LO}^+$  chiral order and with  $\Lambda = 450$  MeV and with SN current used together with the Siegert approach. The pink dashed curve represents similar predictions but with nuclear current reduced to the SN current only. The corresponding bands show predictions at border energies 25 and 45 MeV. The filled circles are experimental data from [52] for the same energy span.

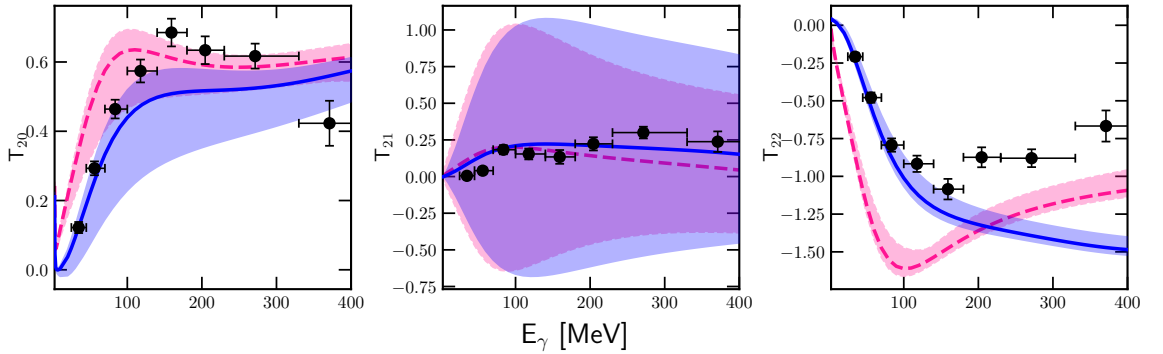


Figure 3.21: The same as in the Fig. 3.20 but for the  $\theta_p$  in range  $70^\circ - 102^\circ$ .

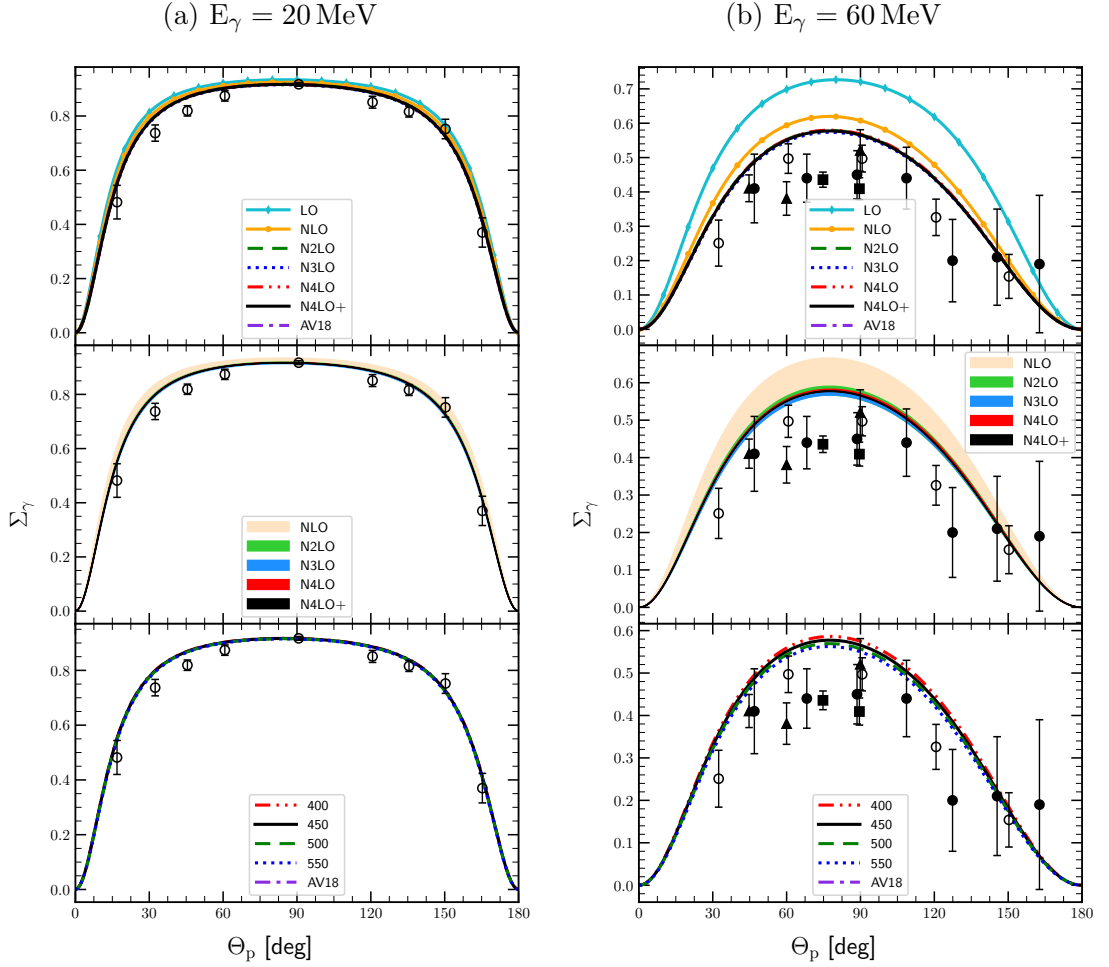


Figure 3.22: The photon asymmetry  $\Sigma_\gamma$  as a function of the outgoing proton angle in the center of mass frame for the photon energy 20 MeV(a) and 60 MeV(b). Top row presents results obtained using the SMS potential with chiral orders from LO to  $N^4\text{LO}^+$  and with the cutoff parameter  $\Lambda = 450$  MeV. The middle row shows truncation errors for each chiral order starting from NLO and the bottom row presents a cutoff dependency for the chiral potential  $N^4\text{LO}^+$ . Filled circles are experimental data from [57], empty circles - from [58], filled squares - from [59] and triangles are from [60]. For the sake of comparison, predictions obtained with the AV18 potential are given by the dashed-dotted curve as well.

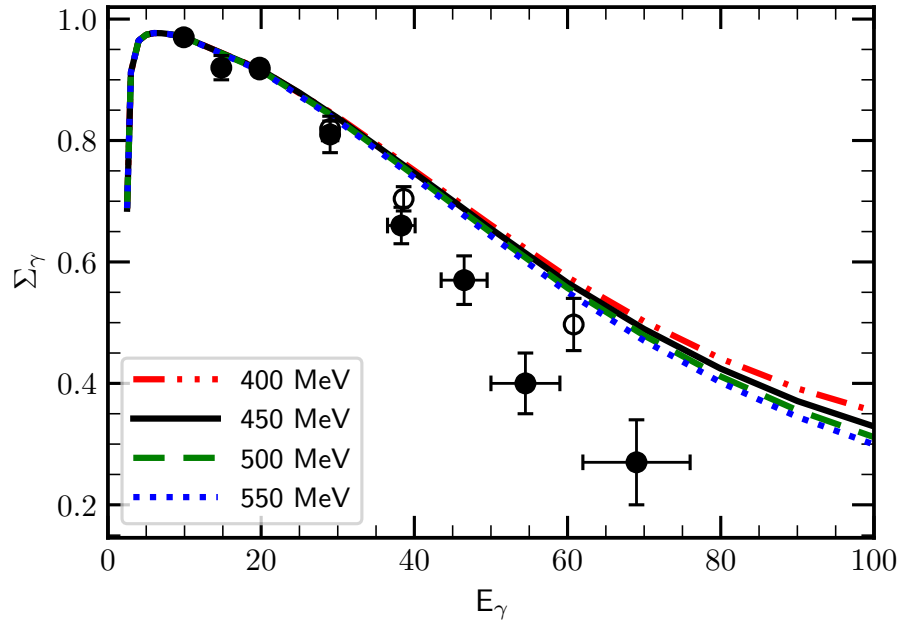


Figure 3.23: The photon asymmetry  $\Sigma_\gamma$  as a function of the photon energy at the fixed outgoing proton's momentum polar angle  $\theta_p = 90^\circ$ . Each curve corresponds to the particular value of the cutoff parameter and chiral potential used here is the  $N^4\text{LO}^+$  one. Filled circles are experimental data from [61], empty circles - from [58].

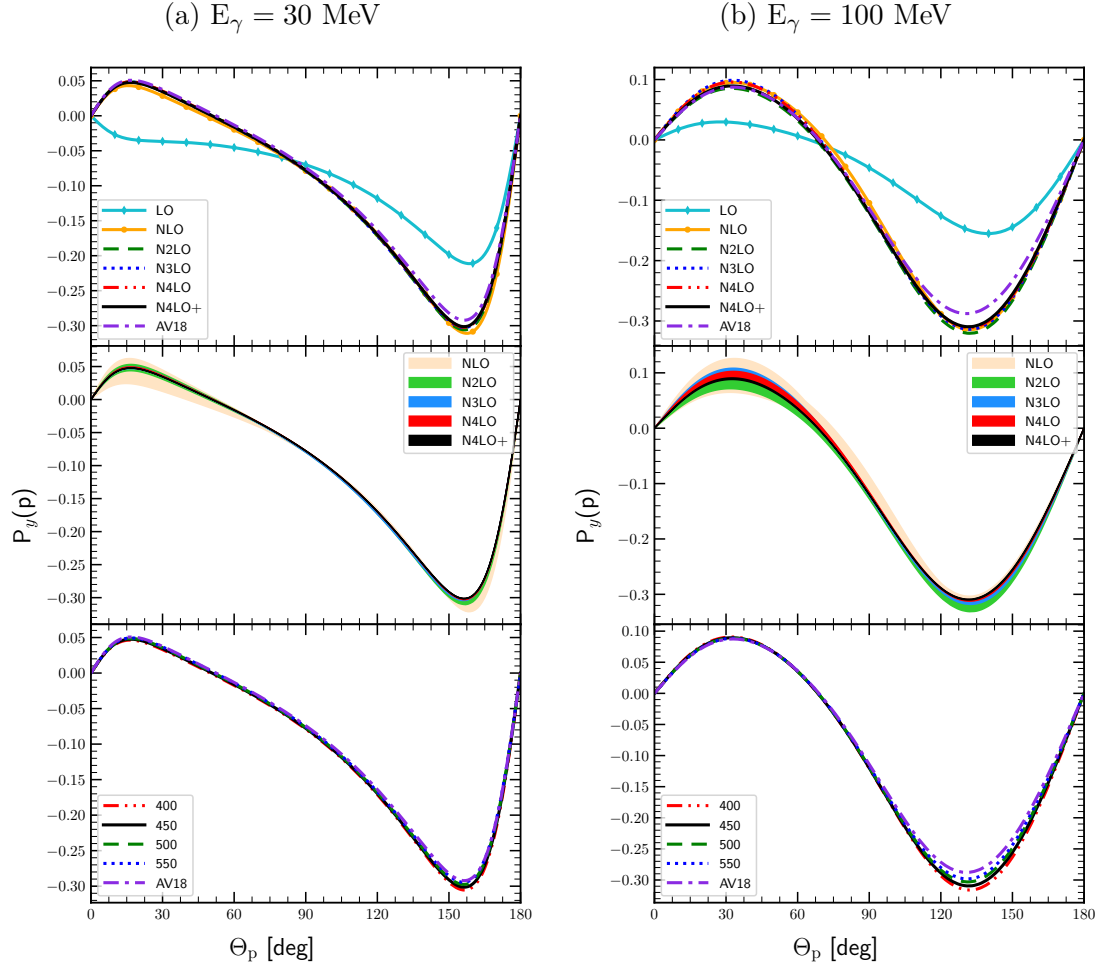


Figure 3.24: Proton polarisation  $P_y(p)$  as a function of the outgoing proton's momentum polar angle in the center of mass frame with the photon energy 30 MeV (a) and 100 MeV (b). Top figures present results obtained using potential with different chiral orders (from LO to  $N^4\text{LO}^+$ ) with cutoff parameter  $\Lambda = 450$  MeV. The middle panel show truncation errors for each chiral order starting from NLO and bottom figures present a cutoff dependency for predictions based on the SMS  $N^4\text{LO}^+$  potential. For the sake of comparison, predictions obtained with the AV18 potential are shown as well.

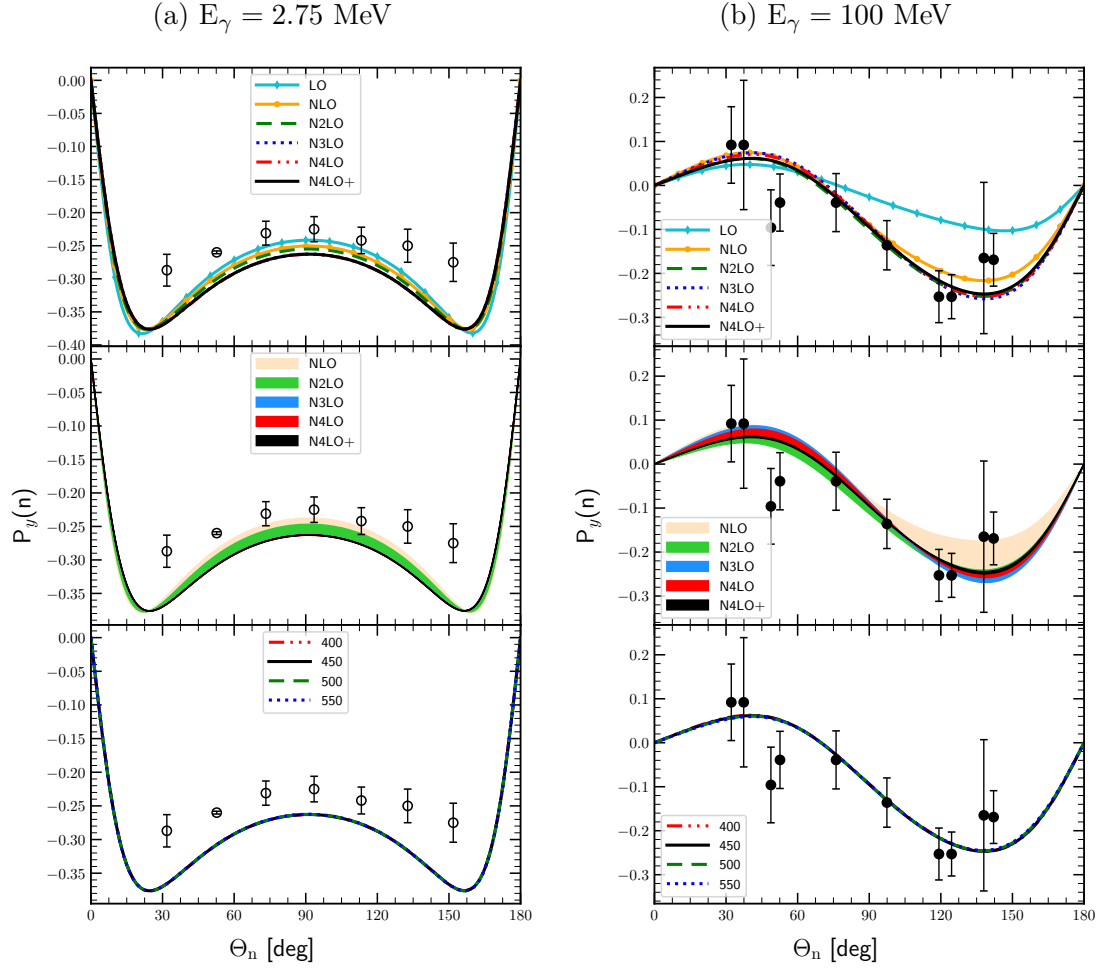


Figure 3.25: The same as in Fig. 3.24 but for the neutron polarisation  $P_y(n)$  and at photon energies 2.75 MeV (a) and 100 MeV (b). Data are from [62] (empty circles) and [63] (filled circles).



## 3.2 Helium photodisintegration

### 3.2.1 3N photodisintegration

In this section I will discuss results for  ${}^3\text{He} \rightarrow p + p + n$  process.

In the Fig. 3.26 I demonstrate a differential cross section  $\frac{d^5\sigma}{d\Omega_1 d\Omega_2 dS}$  as a function of the  $S$  arc length. The photon energy is  $E_\gamma = 30$  MeV and the kinematic configuration  $\theta_1 = 15^\circ$ ,  $\phi_1 = 0^\circ$ ,  $\theta_2 = 15^\circ$ ,  $\phi_2 = 180^\circ$ ; predictions have been obtained without 3NF. We see that only NLO and N<sup>2</sup>LO introduce relatively large truncation error. The maximal width of a band for NLO is 37.6 % at  $S = 10$  MeV, for N<sup>2</sup>LO it is 12.4 % at the same point and it is gradually decreasing coming to 0.13 % at N<sup>4</sup>LO<sup>+</sup>. The cutoff spread around maxima values is less than 3 % and it is 0.78 % at the minimum point ( $S = 10$  MeV).

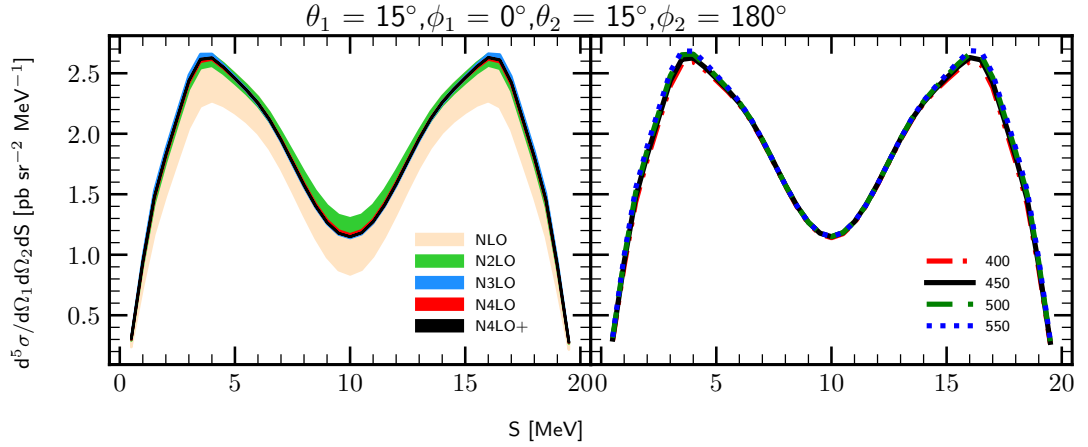


Figure 3.26: The five-fold differential cross section for the photon energy  $E_\gamma = 30$  MeV for the kinematic configuration  $\theta_1 = 15^\circ$ ,  $\phi_1 = 0^\circ$ ,  $\theta_2 = 15^\circ$ ,  $\phi_2 = 180^\circ$ . The left figure presents truncation error bands obtained using potential with chiral orders from NLO to N<sup>4</sup>LO<sup>+</sup>, and with cutoff parameter  $\Lambda = 450$  MeV. The right figure presents a cutoff dependency at N<sup>4</sup>LO<sup>+</sup>. Results are obtained with two-nucleon force only.

With larger energy  $E_\gamma = 100$  MeV demonstrated in the Fig. 3.27, both truncation error and cutoff spread become larger. The truncation band at the maximum point  $S = 10$  MeV for NLO is 55.0 % decreasing to 2.2 % at N<sup>4</sup>LO<sup>+</sup> which is around 3 times larger than it was in predictions with  $E_\gamma = 30$  MeV. The cutoff spread also becomes larger with increasing energy value: 9.0 % at the same (maximum) point which is also  $\sim 3$  times bigger than the one we observed for the lower energy.

Results for other angular configurations at  $\theta_1 = 75^\circ$ ,  $\phi_1 = 75^\circ$ ,  $\theta_2 = 75^\circ$ ,  $\phi_2 = 105^\circ$  are demonstrated in Fig. 3.28. The top row shows results obtained with 2NF only, while predictions obtained with 3NF are shown on the bottom row. It seems that 3NF does not change much the convergence with respect to the chiral order: truncation error band at the point of maximum  $S = 35$  MeV (N<sup>4</sup>LO<sup>+</sup>) is 1.11 % and 1.16 % with and without 3NF, respectively. So it is almost the same, meaning that 3NF contribution arising starting from N<sup>2</sup>LO order does not affect chiral order convergence much.

The cutoff dependence, in turn, is affected by the 3NF presence. Predictions with 2NF only have 13.7 % spread at the same maximum point  $S = 35$  MeV, while predictions with 3NF have only 1.23 % relative spread, so the difference is tremendous.

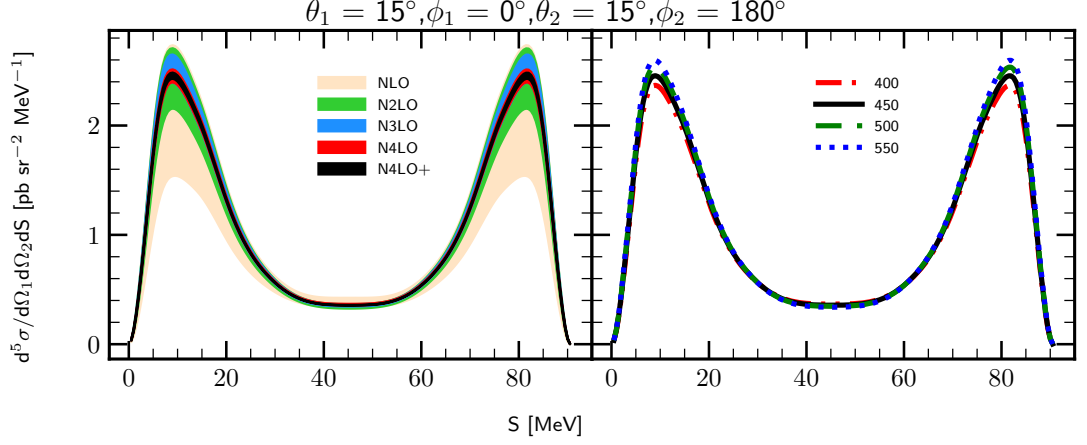


Figure 3.27: The same as in Fig. 3.26 but for the photon energy  $E_\gamma = 100$  MeV

Similar trends are present also in other configurations, demonstrated for the comparison: Figs.3.29, Figs.3.30 and Figs.3.31.

The semi-inclusive differential cross section  $\frac{d^3\sigma}{d\Omega_p dE_p}$  as a function of the outgoing protons energy  $E_p$  is demonstrated on the Fig. 3.32 (for  $E_\gamma = 30$  MeV) and Fig. 3.33 (for  $E_\gamma = 100$  MeV). Each figure consists of subfigures where each row presents results for a proton angles  $\theta_p = 10^\circ, 50^\circ, 90^\circ, 130^\circ$  and  $170^\circ$ . The left part of each subfigure shows a chiral order dependence while the right - cutoff dependence.

At the photon energy 30 MeV the chiral dependence is relatively weak: at the maximum point ( $E_p \simeq 3.8$  MeV) the relative difference varies between 12 % and 28 % at LO for different angles. This difference decreases with each subsequent order resulting in 0.15 % at  $N^4LO+$ . At the energy  $E_\gamma = 100$  MeV truncation errors are larger: at the  $E_p \simeq 1.46$  MeV the discrepancy is around 40 % (NLO), 15 % (N2LO), coming to 1.5 % at  $N^4LO+$ .

The cutoff uncertainty at  $E_\gamma = 30$  MeV is around 2 % and at  $E_\gamma = 100$  MeV is around 8 % for all angles and at the same values of  $E_p$  as regarded above.

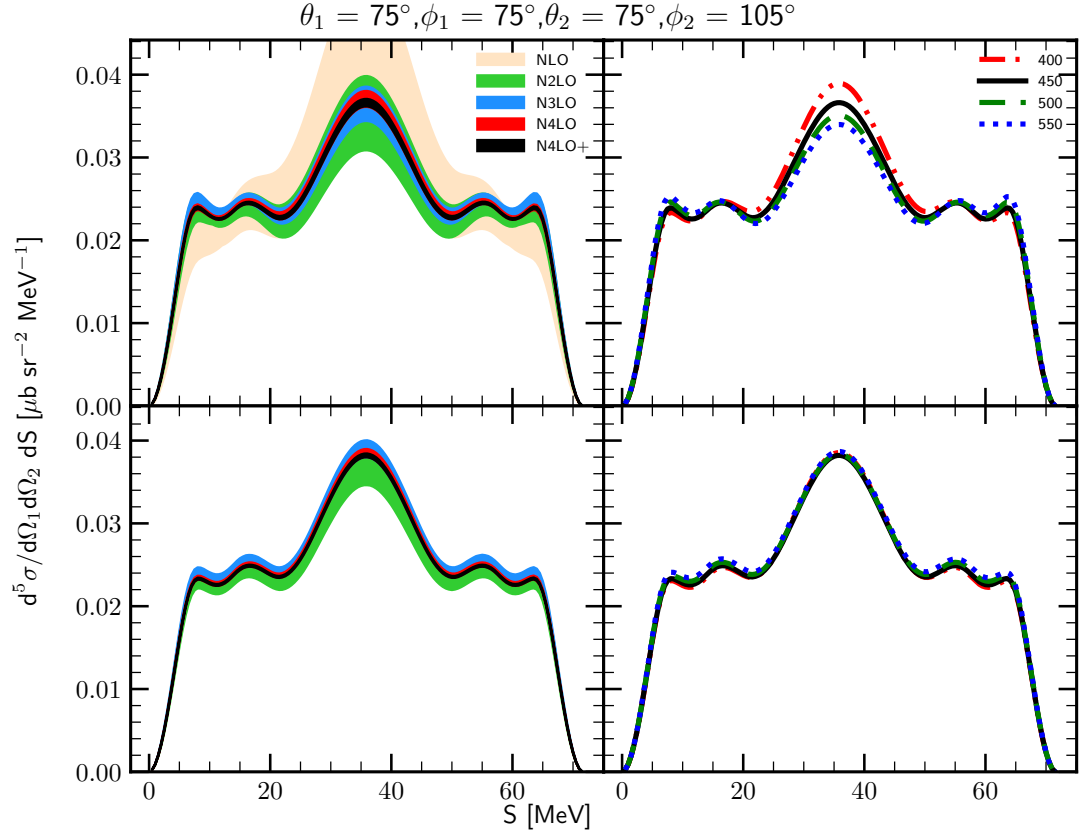


Figure 3.28: The same as in the Fig. 3.27 but for the different kinematic configuration  $\theta_1 = 75^\circ, \phi_1 = 75^\circ, \theta_2 = 75^\circ, \phi_2 = 105^\circ$ . Results obtained with 2NF are presented on the top row. The same, but with 3NF is presented on the bottom row (starting from N<sup>2</sup>LO - where 3NF appears.)

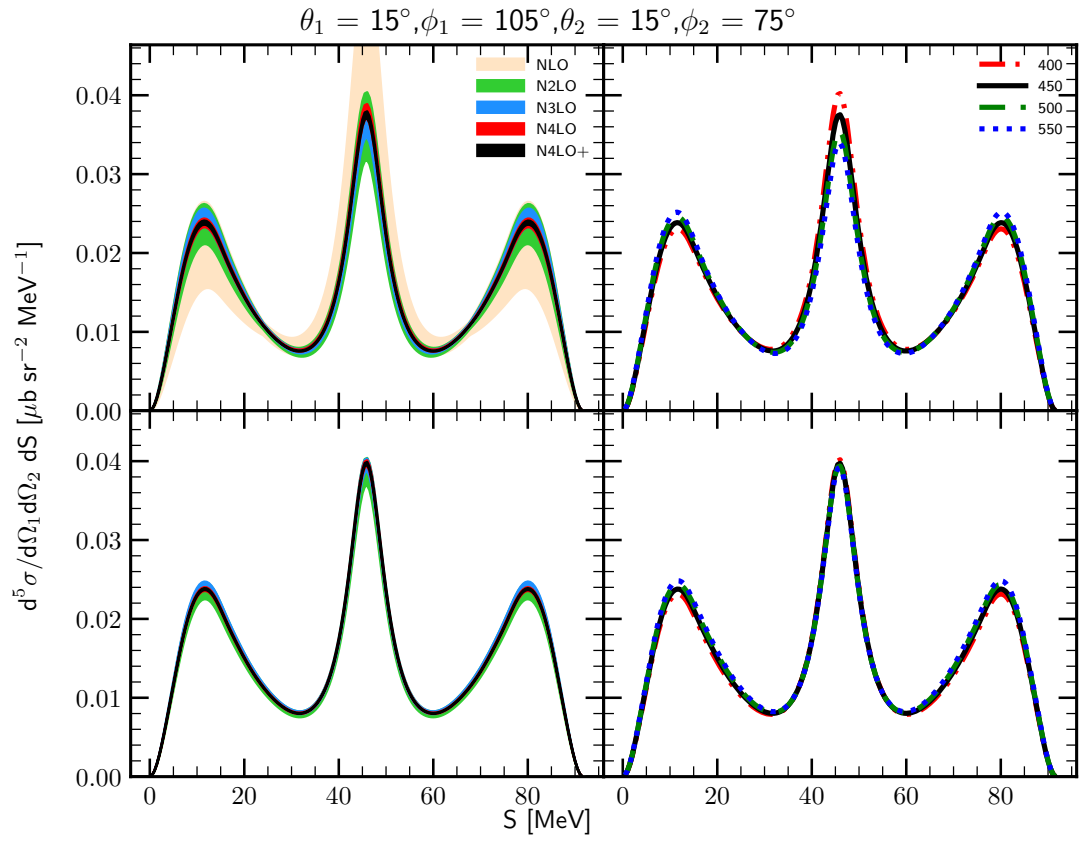


Figure 3.29: The same as in the Fig. 3.28 but for the different kinematic configuration.

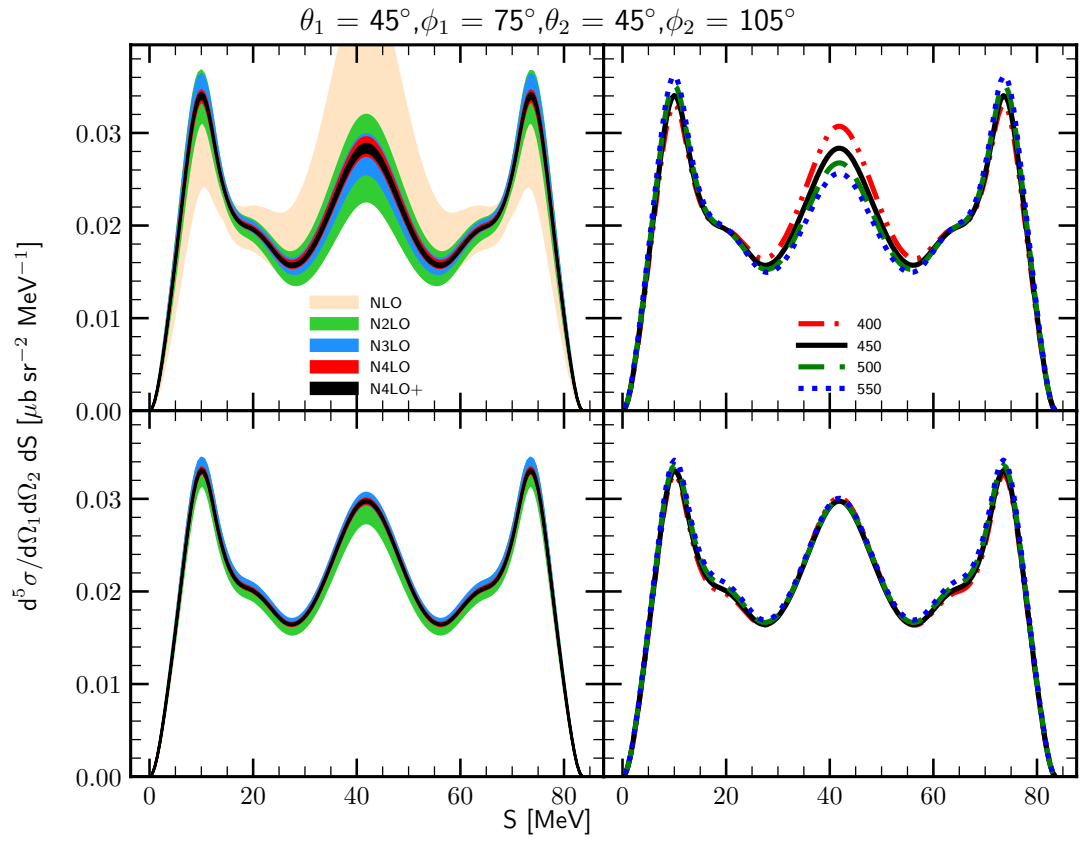


Figure 3.30: The same as in the Fig. 3.29 but for the different kinematic configuration.

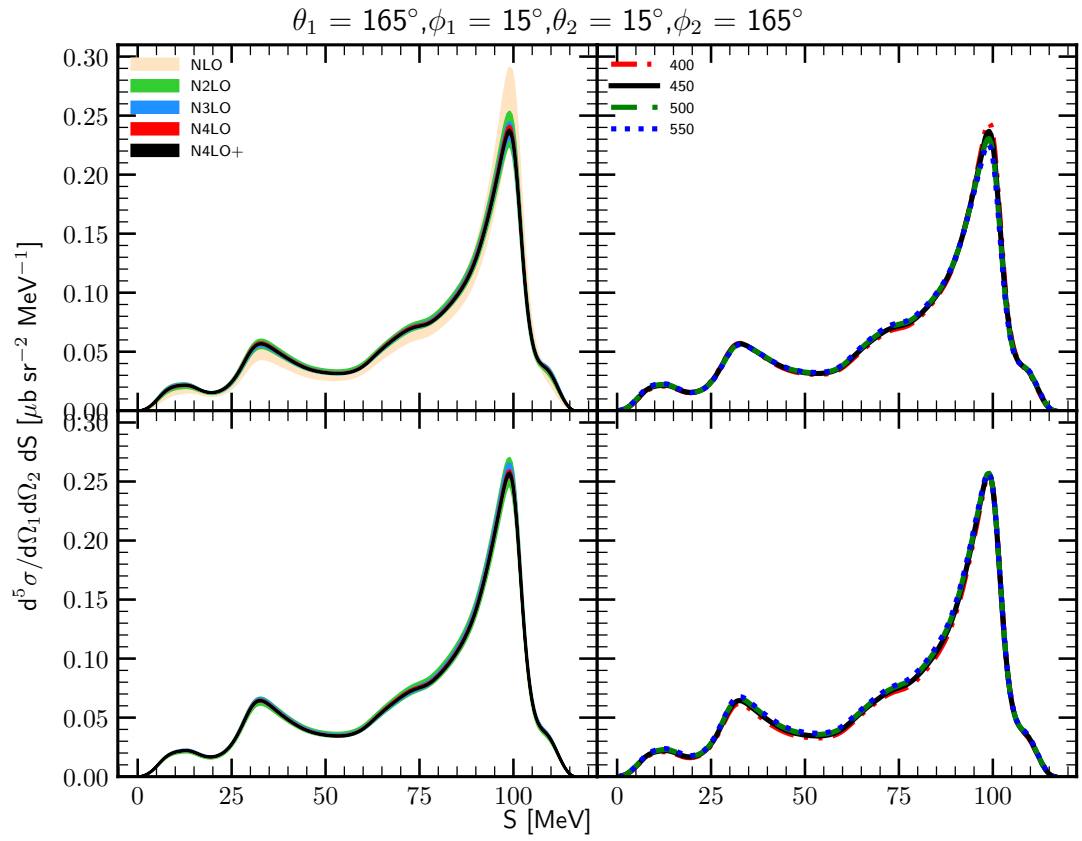


Figure 3.31: The same as in the Fig. 3.30 but for the different kinematic configuration.

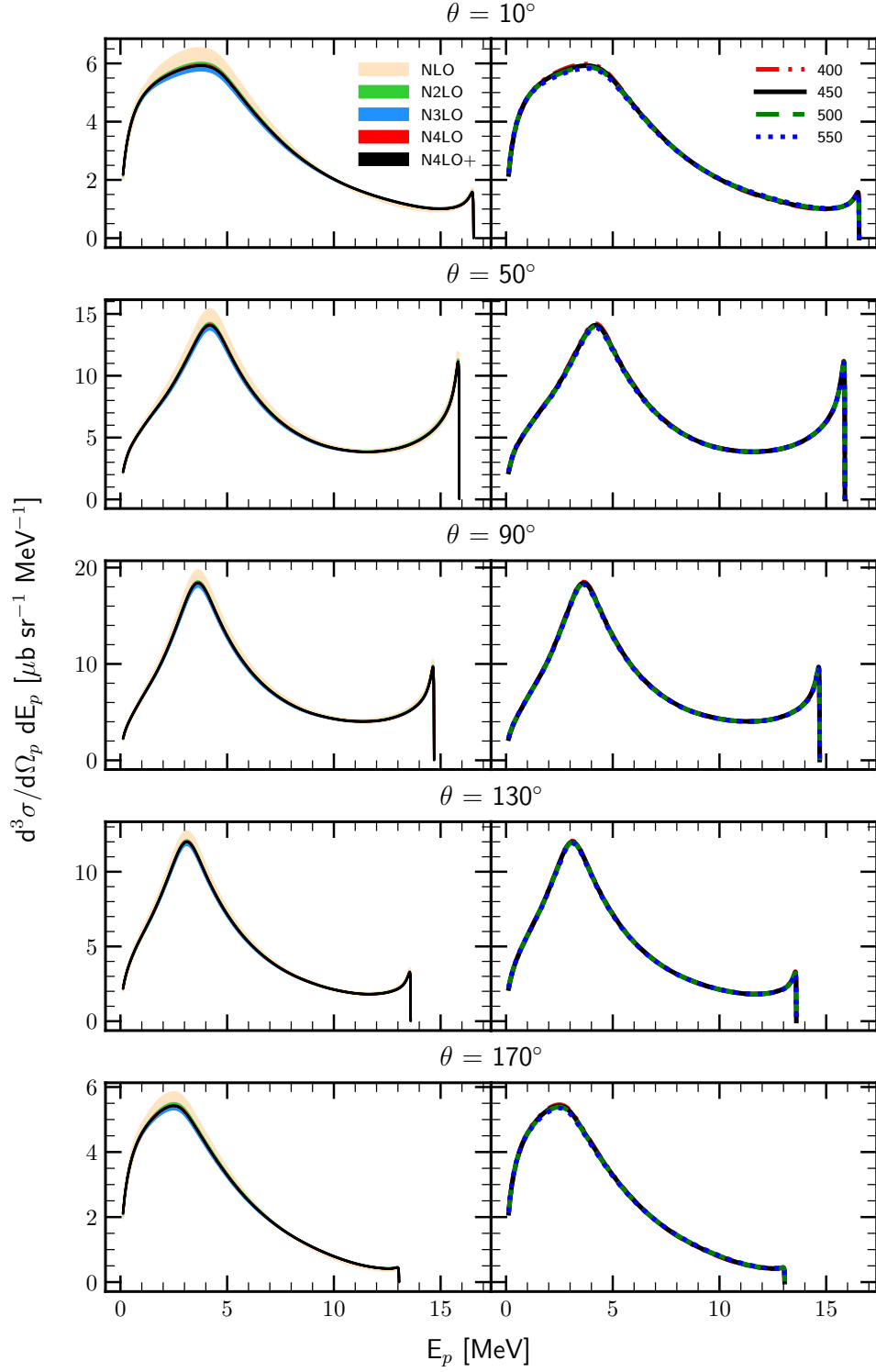
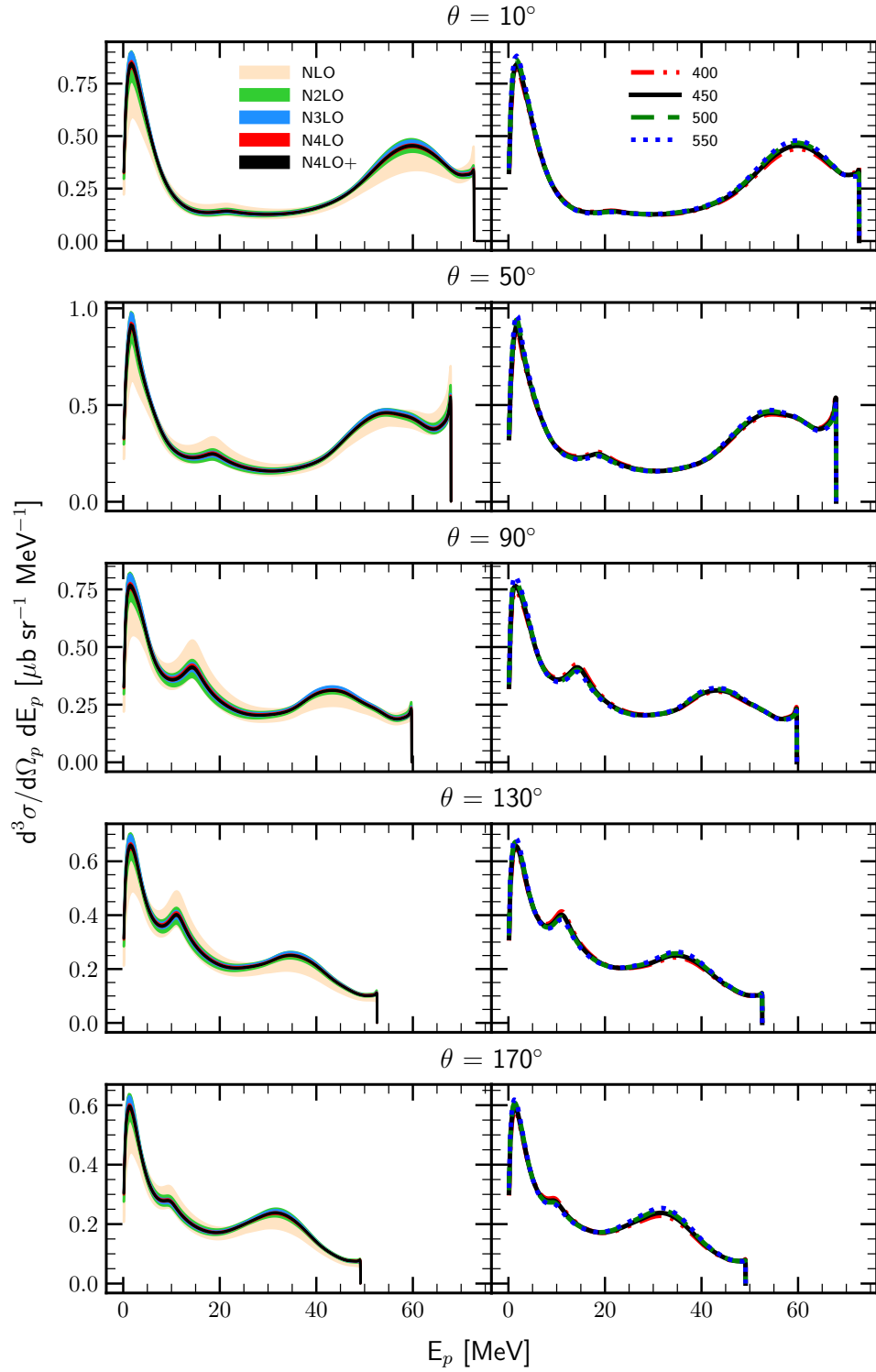


Figure 3.32: The semi-inclusive differential cross section  $\frac{d^3\sigma}{d\Omega_p dE_p}$  at  $E_\gamma = 30$  MeV as a function of outgoing proton energy  $E_p$ . Each row represents predictions for different values of the outgoing proton's momentum polar angle  $\theta_p$ :  $10^\circ$ ,  $50^\circ$ ,  $90^\circ$ ,  $130^\circ$  and  $170^\circ$ . Each column has similar curves and bands definitions as it was for exclusive cross section in Fig. 3.26. Predictions have been obtained with the SMS NN potential but neglecting 3NF.


 Figure 3.33: The same as in Fig. 3.32 but for  $E_\gamma = 100$  MeV



### 3.2.2 D-p photodisintegration

The differential cross section  $d\sigma/d\Omega_d$  for the  ${}^3\text{He} + \gamma \rightarrow d + p$  reaction is presented in the Fig. 3.34 (for the photon energy  $E_\gamma = 30$  MeV) and in the Fig. 3.35 (for the photon energy  $E_\gamma = 100$  MeV). We see that both truncation and cutoff uncertainties are larger with increasing photon energy. The relative spread of the truncation error at the maximum point ( $\theta_p = 105^\circ$ ) for the lower energy is 0.05 % at  $\text{N}^4\text{LO}^+$ , while for the larger energy similar spread is 0.45 % (at  $\text{N}^4\text{LO}^+$ ,  $\theta_p = 120^\circ$ ).

The cutoff dependence is also stronger for the larger energy: it is 1.45 % at 30 MeV and 4.01 % at 100 MeV (at the points of maximum).

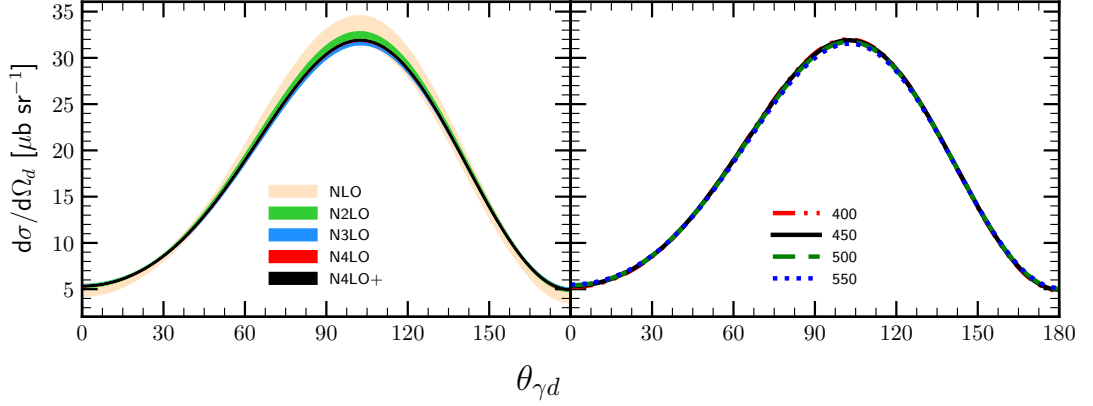


Figure 3.34: Differential cross section for the D- $p$  two-body photodisintegration of  ${}^3\text{He}$  as a function of the  $d\gamma$  angle. The initial photon energy  $E_\gamma = 30$  MeV.

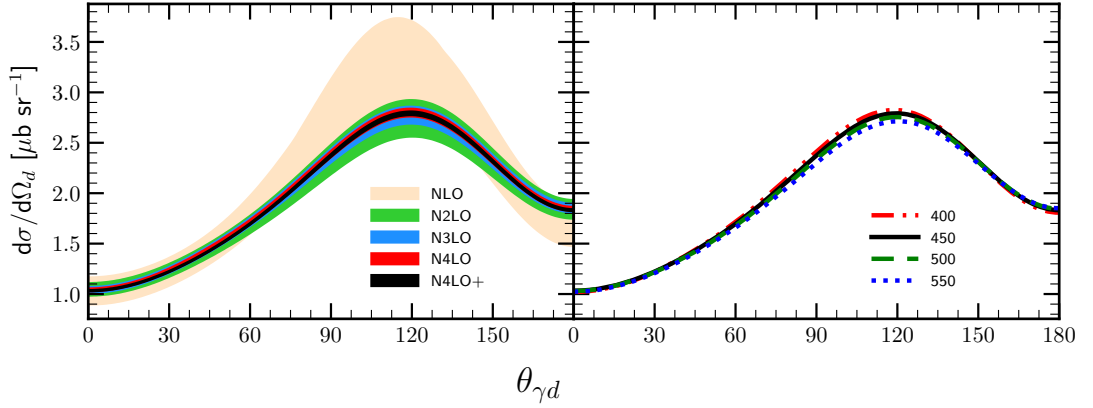


Figure 3.35: The same as on Fig. 3.34 but for the photon energy  $E_\gamma = 100$  MeV

### 3.3 Triton photodisintegration

In this section I will discuss results for  ${}^3\text{H} \rightarrow p + n + n$  process.

In the Fig. 3.36 I demonstrate a differential cross section  $\frac{d^5\sigma}{d\Omega_1 d\Omega_2 dS}$  as a function of the  $S$  arc length. The photon energy is  $E_\gamma = 30$  MeV and the kinematic configuration  $\theta_1 = 15^\circ$ ,  $\phi_1 = 0^\circ$ ,  $\theta_2 = 15^\circ$ ,  $\phi_2 = 180^\circ$ ; predictions have been obtained without 3NF. We see that only NLO and N<sup>2</sup>LO introduce relatively large truncation error. The maximal width of a band for NLO is 30.95 % at  $S = 10$  MeV, for N<sup>2</sup>LO it is 6.79 % at the same point and it is gradually decreasing coming to 0.10 % at N<sup>4</sup>LO<sup>+</sup>. The cutoff spread around maxima values is 6.25 % (at  $S = 4$  MeV) and it is 1.81 % at  $S = 10$  MeV.

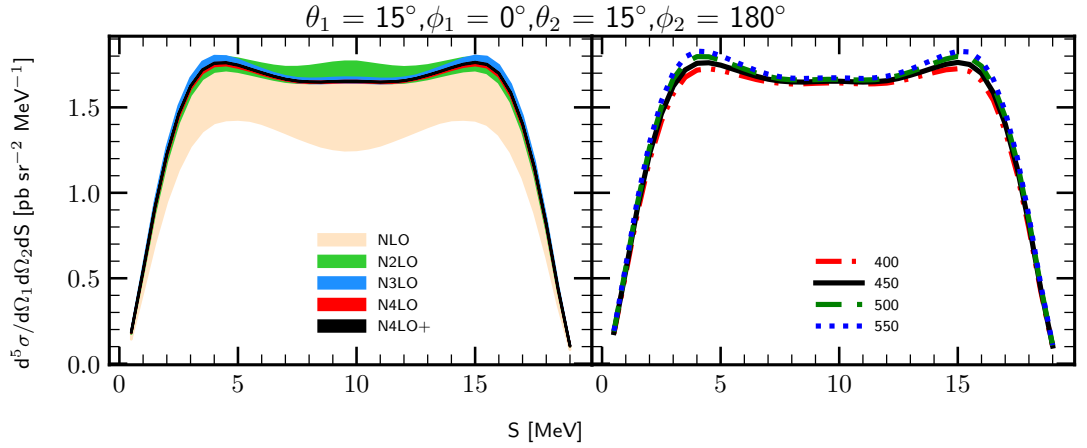


Figure 3.36: The five-fold differential cross section for the photon energy  $E_\gamma = 30$  MeV for the kinematic configuration  $\theta_1 = 15^\circ$ ,  $\phi_1 = 0^\circ$ ,  $\theta_2 = 15^\circ$ ,  $\phi_2 = 180^\circ$ . The left figure presents truncation error bands obtained using potential with chiral orders from NLO to N<sup>4</sup>LO<sup>+</sup>, and with cutoff parameter  $\Lambda = 450$  MeV. The right figure presents a cutoff dependency at N<sup>4</sup>LO<sup>+</sup>. Results are obtained with two-nucleon force only.

With larger energy  $E_\gamma = 100$  MeV demonstrated in the Fig. 3.37, the truncation band at the maximum point  $S = 10$  MeV for NLO is 50.26 % decreasing to 2.00 % at N<sup>4</sup>LO<sup>+</sup>. The cutoff spread also becomes larger with increasing energy value: 9.52 % at the same (maximum).

The truncation error bands and cutoff dependance is very similar as it was for the three-body Helium photodisintegration 3.2.1 and the relative errors have a similar range of values.

Results for other angular configurations at  $\theta_1 = 75^\circ$ ,  $\phi_1 = 75^\circ$ ,  $\theta_2 = 75^\circ$ ,  $\phi_2 = 105^\circ$  are demonstrated in Fig. 3.38 with  $E_\gamma = 30$  MeV. Both truncation errors and cutoff dependance are lower at this configuration: the relative width of the truncation band at NLO is 9.39 % (at the maximum point  $S = 8$  MeV) and drops to only 0.1 % at N<sup>4</sup>LO<sup>+</sup>. The relative cutoff spread is 0.93 % at the same point.

At the larger energy  $E_\gamma = 100$  MeV demonstrated in Fig. 3.39 uncertainties have been increased. The truncation bands are 44.42 % and 2.09 % (at NLO and N<sup>4</sup>LO<sup>+</sup> respectively) and the cutoff spread is 13.04 % (all at  $S = 35$  MeV).

Similar trends are present also in other configurations, demonstrated for the comparison: Figs. 3.40, 3.41, 3.42, 3.43, 3.44 and 3.45.

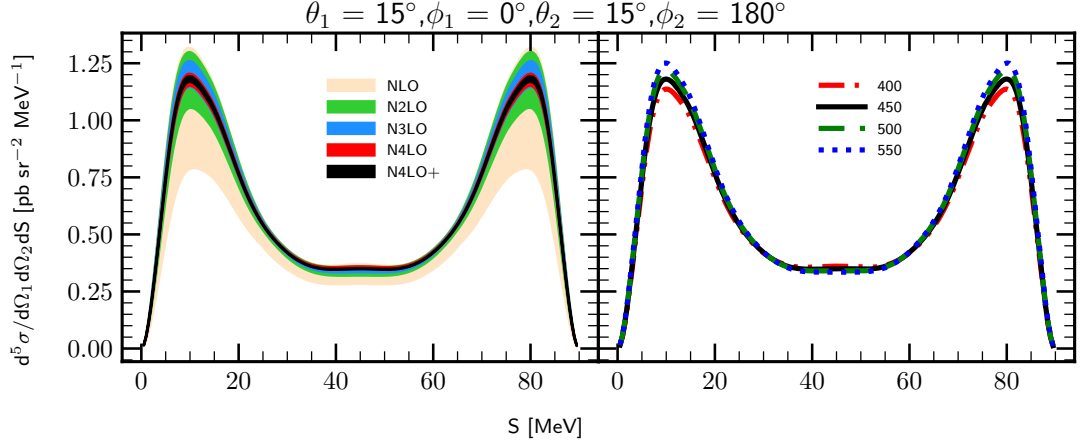


Figure 3.37: The same as in the Fig. 3.36 but for the photon energy  $E_\gamma = 100$  MeV.

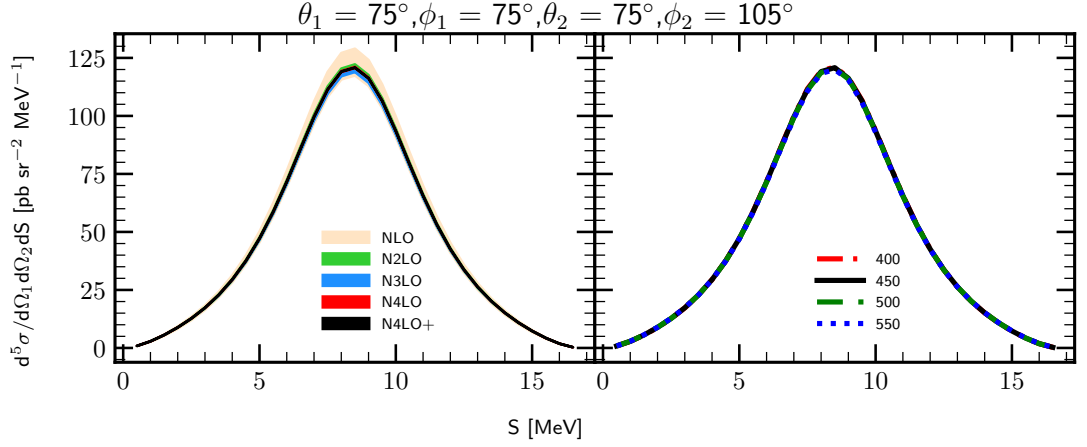


Figure 3.38: The same as in the Fig. 3.36 but for the different kinematic configuration  $\theta_1 = 75^\circ$ ,  $\phi_1 = 75^\circ$ ,  $\theta_2 = 75^\circ$ ,  $\phi_2 = 105^\circ$ . Results obtained with 2NF only.

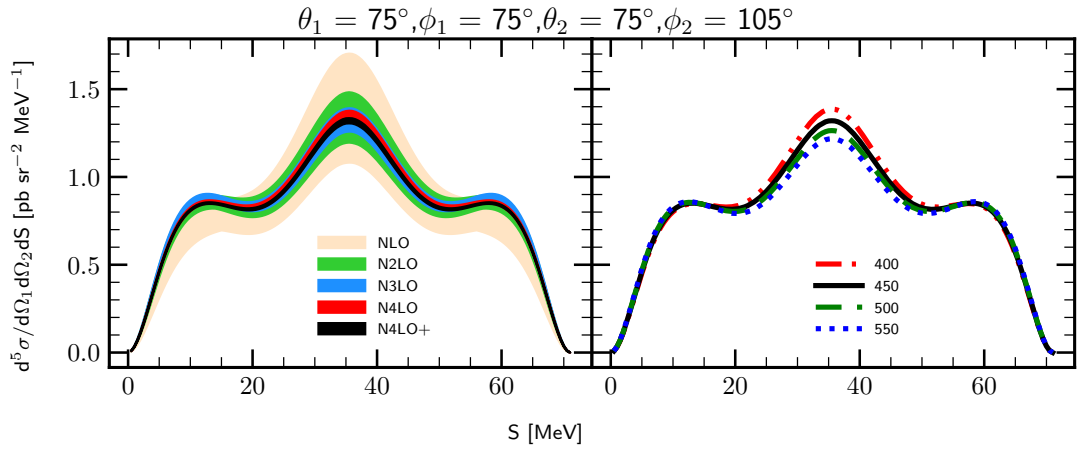


Figure 3.39: The same as in the Fig. 3.38 but for the photon energy  $E_\gamma = 100$  MeV.

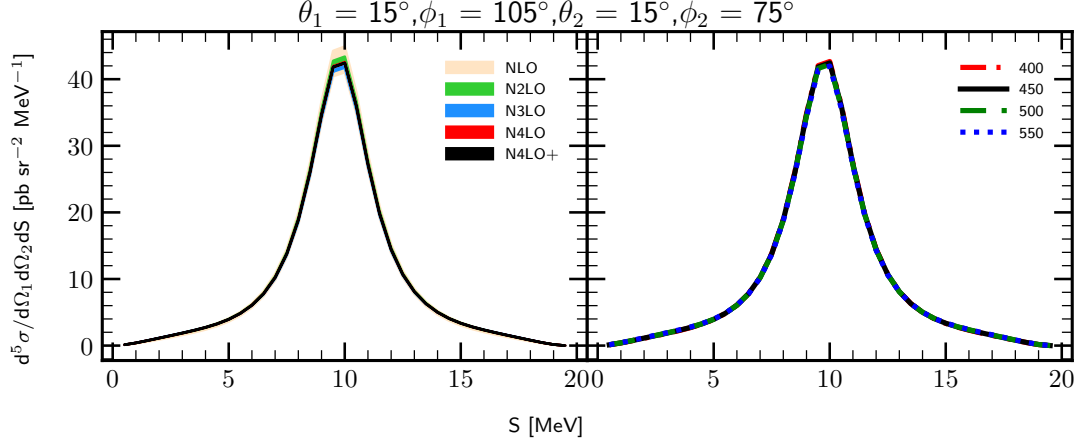


Figure 3.40: The same as in the Fig. 3.38 but for the different kinematic configuration  $\theta_1 = 15^\circ$ ,  $\phi_1 = 105^\circ$ ,  $\theta_2 = 15^\circ$ ,  $\phi_2 = 75^\circ$ . Results obtained with 2NF only.

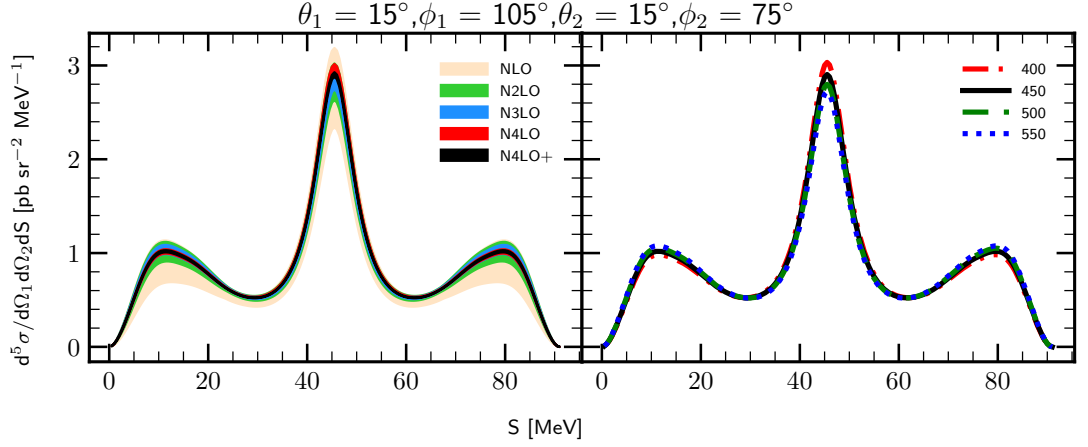


Figure 3.41: The same as in the Fig. 3.40 but for the photon energy  $E_\gamma = 100$  MeV.

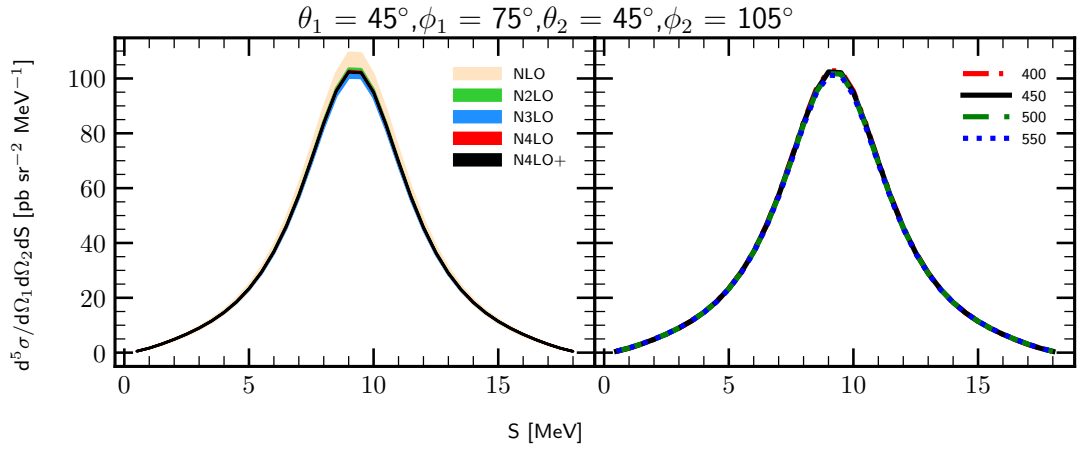
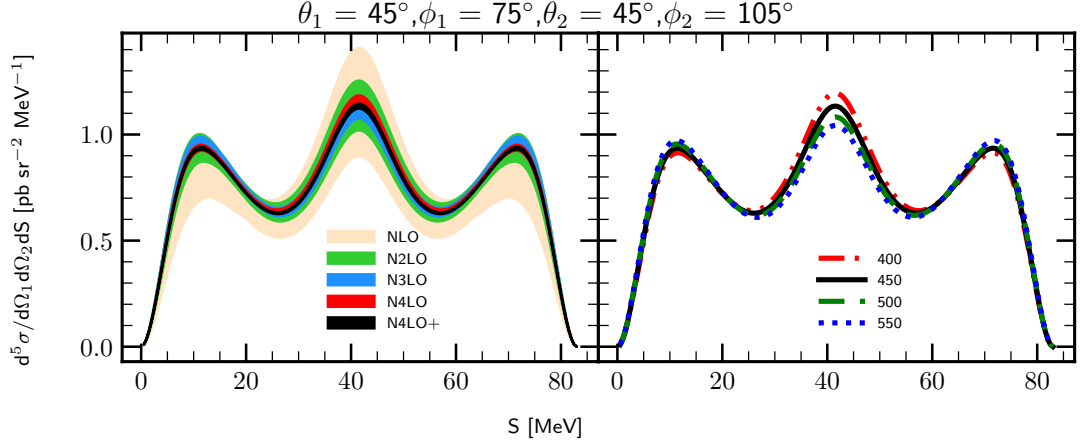
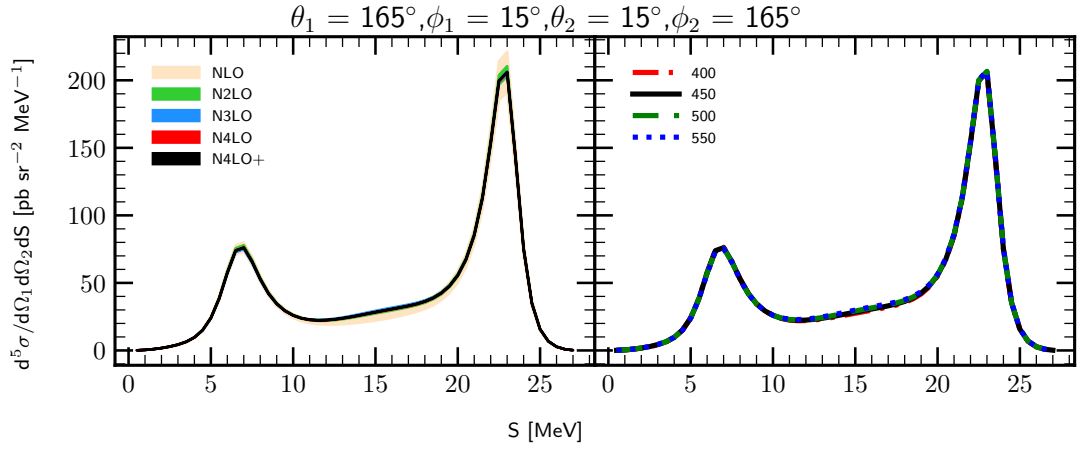
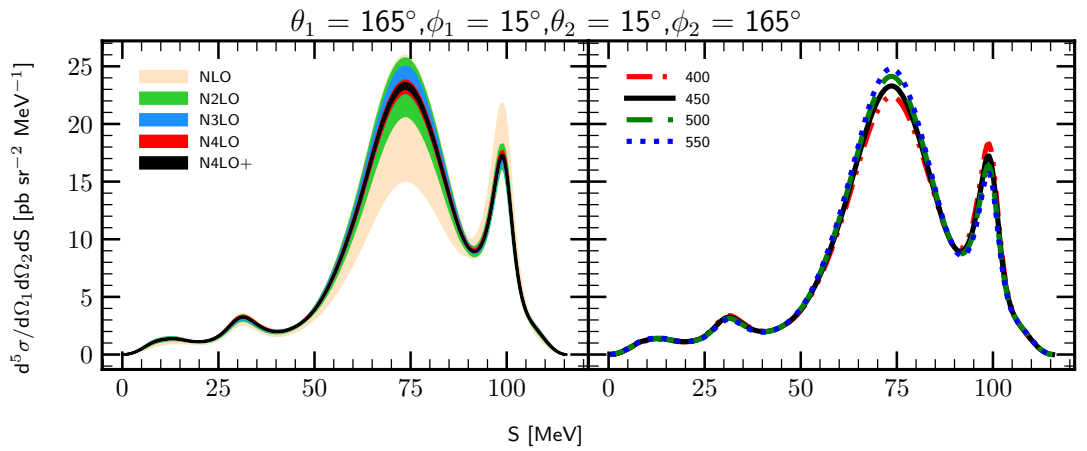


Figure 3.42: The same as in the Fig. 3.40 but for the different kinematic configuration  $\theta_1 = 45^\circ$ ,  $\phi_1 = 75^\circ$ ,  $\theta_2 = 45^\circ$ ,  $\phi_2 = 105^\circ$ . Results obtained with 2NF only.


 Figure 3.43: The same as in the Fig. 3.42 but for the photon energy  $E_\gamma = 100$  MeV.

 Figure 3.44: The same as in the Fig. 3.42 but for the different kinematic configuration  $\theta_1 = 165^\circ$ ,  $\phi_1 = 15^\circ$ ,  $\theta_2 = 15^\circ$ ,  $\phi_2 = 165^\circ$ . Results obtained with 2NF only.

 Figure 3.45: The same as in the Fig. 3.44 but for the photon energy  $E_\gamma = 100$  MeV.

## 3.4 Pion absorption from the lowest atomic orbital

### 3.4.1 Pion absorption in $^3\text{He}$

in Fig. 3.46 and 3.47 the pion absorption rates are presented as a function of the chiral order with different values of the cutoff parameter (for  $\pi^- + ^3\text{He} \rightarrow p + n + n$  and  $\pi^- + ^3\text{He} \rightarrow n + d$  reactions, respectively). Both figures show that with fixed chiral order the arrangement of values with respect of the cutoff parameter remains the same, namely with increasing  $\Lambda$ , absorption rate decreases. The only exception in both cases appears at N<sup>3</sup>LO where prediction with  $\Lambda = 550$  MeV goes above other predictions. At the next order, N<sup>4</sup>LO, it corrects to the normal arrangement. This behavior may be connected to the 3NF used for the calculation and in order to check that I show a similar figure for a proton radius  $r_p$  in Fig. 3.48 calculated with and without 3NF (left and right panels respectively). Results obtained with 3NF show similar deviation at N<sup>3</sup>LO while data obtained without 3NF does not have that. Nevertheless, the spread of predictions with respect to the cutoff values is much smaller with 3NF and deviation seems to be not crucial as total difference between predictions in this case is very small.

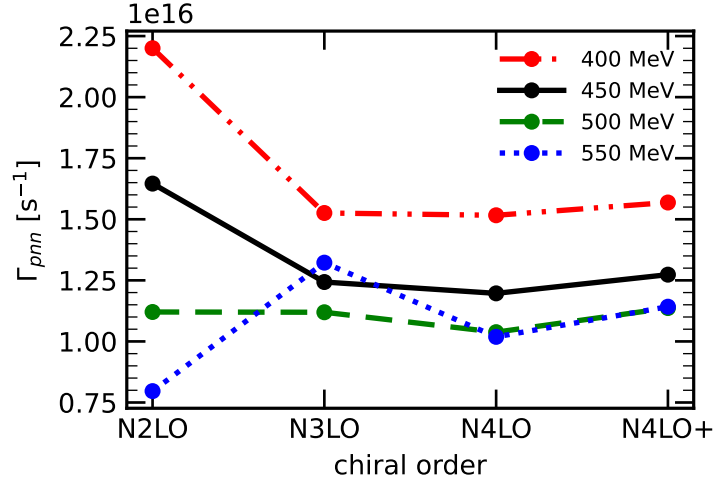


Figure 3.46: Absorption rate for  $\pi^- + ^3\text{He} \rightarrow p + n + n$  reaction as a function of the chiral order with different values of the cutoff parameter  $\Lambda$ . Predictions were obtained with 3NF.

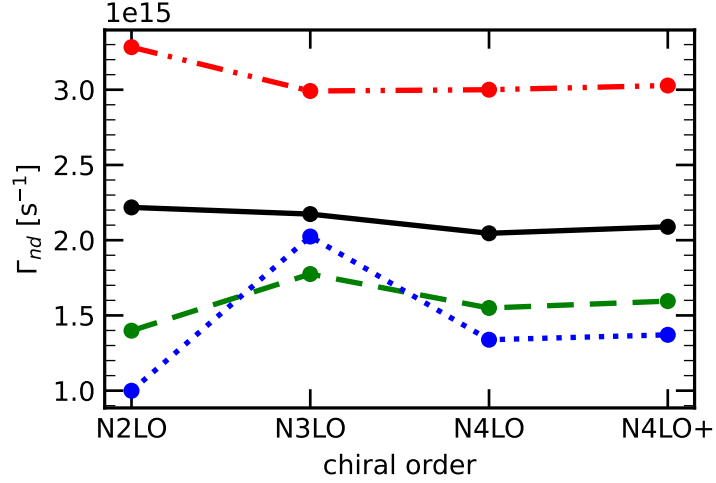
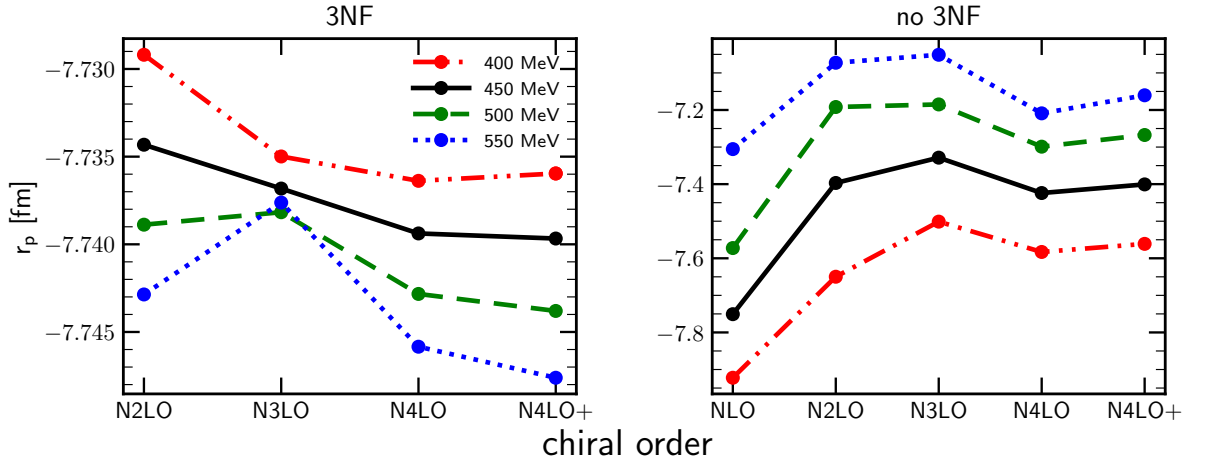
In Figs. 3.49 and 3.50 I show intensity plots for the double differential absorption rates  $d^2\Gamma_{pnn}/dE_1dE_2$  for the  $\pi^- + ^3\text{He} \rightarrow p + n + n$  process as functions of the nucleons energies (first nucleon is proton) and of *correct naming* Dalitz coordinates( $x$  and  $y$ ) respectively.

In Fig. 3.50 coordinates  $x$  and  $y$  are defined as:

$$\begin{aligned} x &= 3(E_1 + 2E_2 - E)/E, \\ y &= (3E_1 - E)/E, \end{aligned} \tag{3.4}$$

taking the region where  $r^2 \equiv x^2 + y^2 \leq 1$ .

Each of two figures consists of four panels representing predictions obtained with different values of the cutoff parameter  $\Lambda$ . The difference between predictions which can be noticed with the naked eye - is that area of the central region (corresponding to


 Figure 3.47: The same as in Fig. 3.46, but for  $\pi^- + {}^3\text{He} \rightarrow n + d$  reaction.

 Figure 3.48: *check mt3* Proton radius  $r_p$  as a function of the chiral order calculated with different values of the cutoff parameter  $\Lambda$ . The radius was calculated with 2NF and 3NF (left panel) and with 2NF only (right panel).

smallest values) becomes larger with increasing  $\Lambda$ . It coheres to what we saw in Fig. 3.46 where total absorption rate was inversely correlated with cutoff parameter. The dominant contribution comes from the region with lowest proton energy values of  $E_1 \rightarrow 0$  where both neutrons have similar large values. This is a situation when proton is a spectator while both neutrons share all energy - quasi-free scattering(QFS).

Another region with high absorption rate is neutron-neutron final state interaction (FSI(nn)). It is located at high  $E_1$  when proton gets one third part of total energy while neutrons both get one sixth.

Next I show similar colormaps but for the predictions obtained with plane wave component only (without rescattering part) in Figs. 3.51 and 3.52. Presented plots show that the difference of predictions obtained without rescattering part with full is very large. Predicted values are few times larger and the distribution is completely different. The FSI(nn) region is not presented here in a sense that there is no peak with respect to other values. The QFS region is, on the contrary, which obviously tells us that one has to take

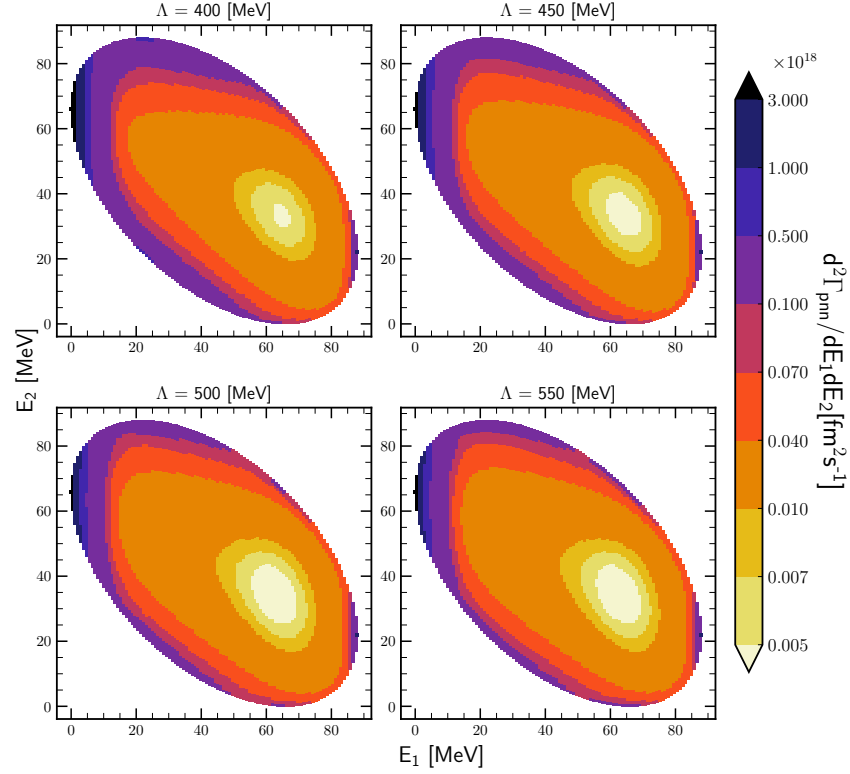


Figure 3.49: Intensity plots for the double differential absorption rates  $d^2\Gamma_{pnn}/dE_1 dE_2$  for the  $\pi^- + {}^3\text{He} \rightarrow p + n + n$  process, obtained using the SMS potential at  $\text{N}^4\text{LO}^+$  with all contributions possible: plane wave + rescattering, SN + 2N, 2NF+3NF. Each panel present predictions obtained with different values of the cutoff parameter  $\Lambda$ : from 400 MeV (upper left) to 550 MeV (lower right). Nucleon 1 is a proton.

into account rescattering part in order to obtain relevant results.

Results obtained with Plane wave plus recattering part and with single nucleon current only are presented in Figs. 3.53 and 3.54. As previously, each panel in figures presents predictions obtained with different values of the cutoff parameter  $\Lambda$ . In contrast to the configurations shown above, the change of the cutoff value has larger impact here: we see that there is a different pattern in each panel. It does not change dramatically, but two peaks inside the figure become more or less clear. On the other hand, the distribution of the absorption rate is very different from the one, obtained with more complete components setup (Figs. 3.49 and 3.50).

Figs. 3.55 and 3.56 show prediction obtained using similar configuration as in Figs. 3.49 and 3.50, but each panel includes predictions obtained with different chiral orders of the SMS potential. We see that predictions are not sensitive to the chiral order and even  $\text{N}^2\text{LO}$  predictions are pretty much similar to ones obtained with the most advanced  $\text{N}^4\text{LO}$  potential.

Following figures demonstrate the same results but from the different perspective. Namely in Fig. 3.57 I show differential absorption rate  $d\Gamma_{pnn}/dE_p$  that is the same as in e.g. Fig. 3.55, but integrated over  $E_n$ . All the results are obtained with the most advanced setup (plane wave + rescattering, SN + 2N, 2NF+3NF). The left panel consists of the results with  $\Lambda = 450$  MeV and each curve correspond to a particular chiral order. Interesting region here is a maximum point which corresponds to a bottom part of the



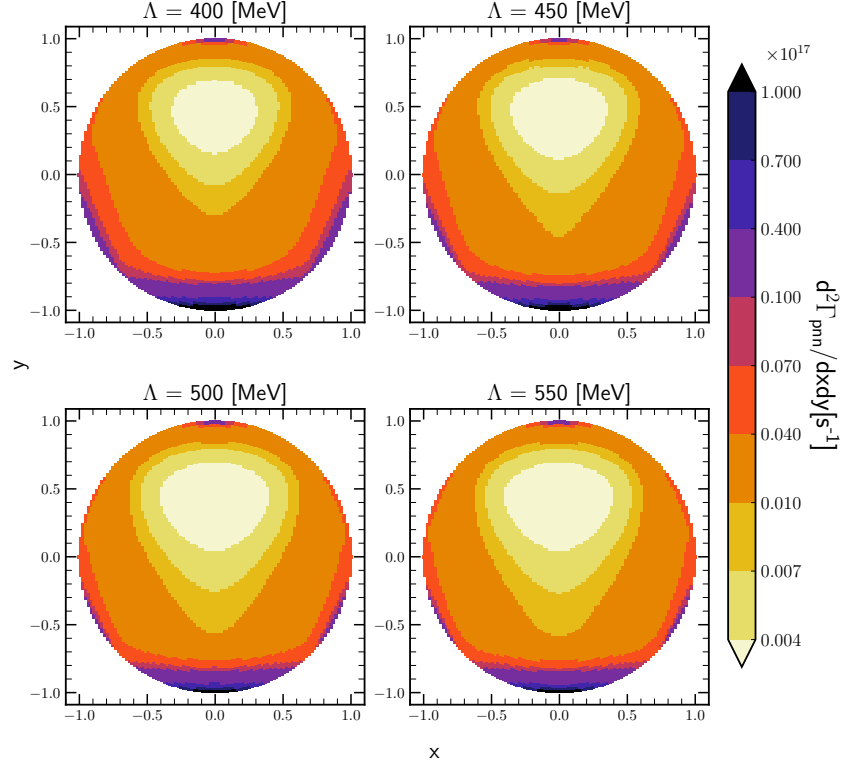


Figure 3.50: The same as in Fig. 3.49 but for the double differential absorption rates  $d^2\Gamma_{pnn}/dx dy$ .

circles from Fig. 3.55. At the point of maximum N<sup>2</sup>LO outstands from other results as its point of maximum is noticeably higher. At  $E_p = 0.92$  MeV (maximum point) the value of N<sup>2</sup>LO is 1.37 times larger than one from N<sup>4</sup>LO<sup>+</sup> ( $3.44 \times 10^{17}$  fm s<sup>-1</sup> vs  $2.52 \times 10^{17}$  fm s<sup>-1</sup>) - the relative difference is 31.1 %. At the same time, the relative difference between all the predictions except for N<sup>2</sup>LO is 8.3 %

The right panel of the Fig. 3.57 shows a cutoff dependance of the predictions obtained with the SMS chiral potential at N<sup>4</sup>LO<sup>+</sup>. In this case maximum point is interesting as well. We see that predictions with  $\Lambda = 500$  MeV and 550 MeV are quite close to each other: the relative difference between them at  $E_p = 0.92$  MeV is only 1.5 %. In turn the spread between  $\Lambda = 400$  MeV, 450 MeV and 500 MeV is 40 % (at the same point). This cutoff dependance is hidden looking at the colormaps Fig. 3.49, but from this prospective it is clearly presented.

Similarly in Fig. 3.58  $d\Gamma_{pnn}/dE_n$  is presented. We observe similar trends which are also shown up at the extremum point which is around  $E_n = 66.9$  MeV now. The difference between N<sup>2</sup>LO and N<sup>4</sup>LO<sup>+</sup> predictions at this point is 29.0 %. The relative difference between all the predictions except for N<sup>2</sup>LO is 7.5 %. The cutoff predictions are also very similar for  $\Lambda = 500$  MeV and 550 MeV (the spread is 1.6 %) while all the rest predictions are quit distinguished - the spread is 39.1 %.

Coming to the next figures Fig. 3.59 and Fig. 3.60 which show 1D dependance of the absorption rate on the Dalitz coordinates  $r = \sqrt{x^2 + y^2}$  and  $\phi = \arctan \frac{y}{x}$ . The similar trend is preserved, namely chiral order figures show that N<sup>2</sup>LO predictions outstand from all other predictions, and noticeable cutoff dependance is observed.

In general we can conclude that predictions are converged starting from the N<sup>3</sup>LO

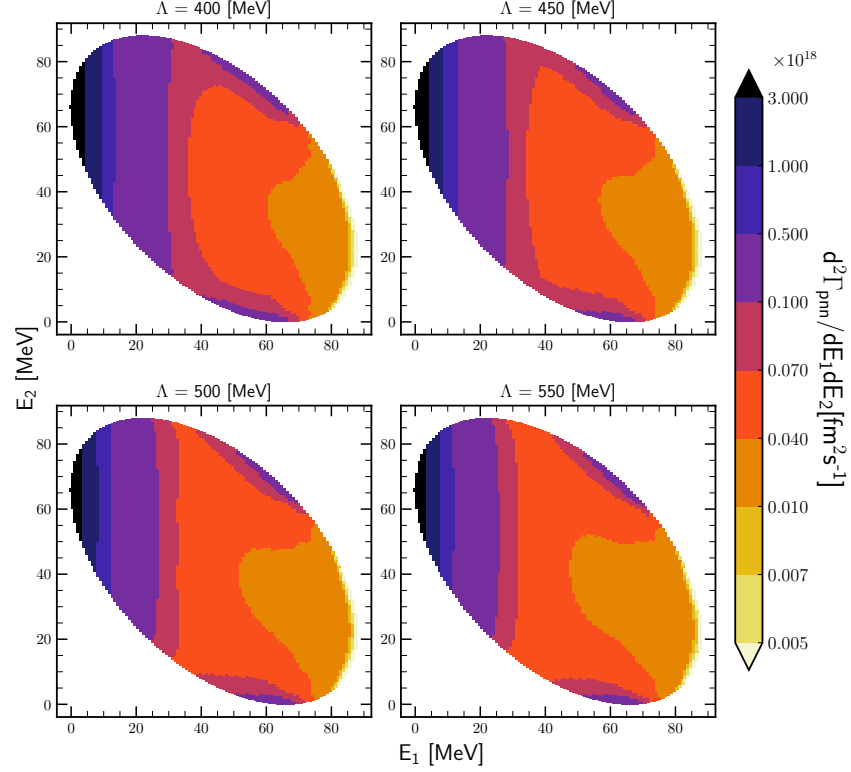


Figure 3.51: Intensity plots for the double differential absorption rates  $d^2\Gamma_{pn}/dE_1 dE_2$  for the  $\pi^- + {}^3\text{He} \rightarrow p + n + n$  process, obtained using the SMS potential at  $\text{N}^4\text{LO}^+$  with plane wave part only (without rescattering). All other contributions are the same as in Fig. 3.49: SN + 2N and 2NF+3NF. Each panel present predictions obtained with different values of the cutoff parameter  $\Lambda$ : from 400 MeV (upper left) to 550 MeV (lower right). Nucleon 1 is a proton.

chiral order as most of the demonstrated results show that the difference between  $\text{N}^3\text{LO}$ ,  $\text{N}^4\text{LO}$  and  $\text{N}^4\text{LO}^+$  is negligible. At the same time we observe a cutoff dependence where predictions obtained with  $\Lambda = 500$  MeV and 550 MeV are very similar, but the spread with all the rest values is there. This nature of the cutoff dependence is also reflected in the total absorption rate, presented in Fig. 3.46.

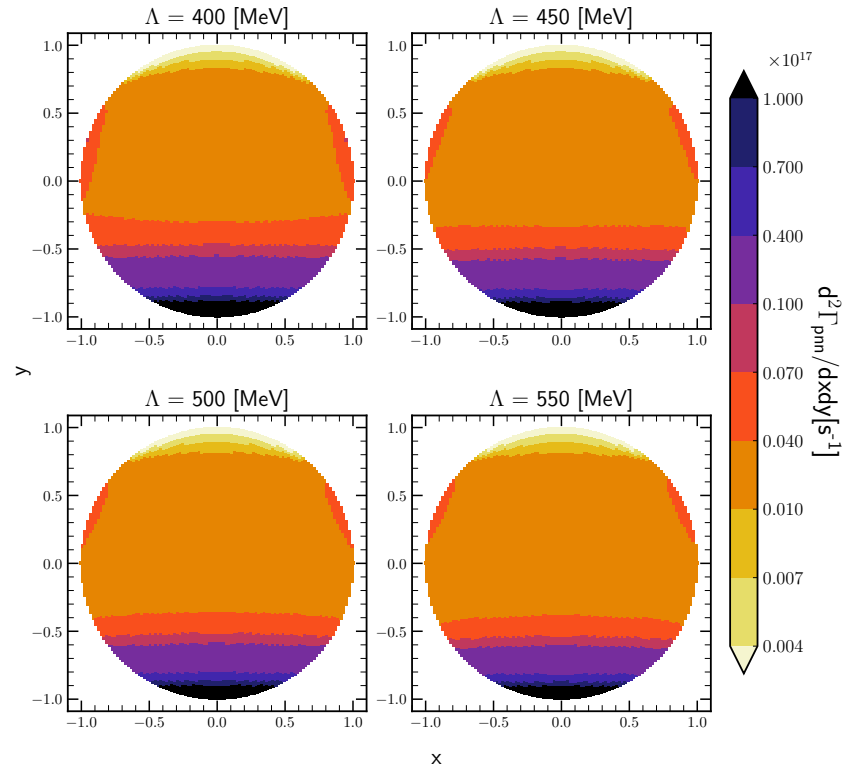


Figure 3.52: The same as in Fig. 3.51 but for the double differential absorption rates  $d^2\Gamma_{pnn}/dx dy$ .

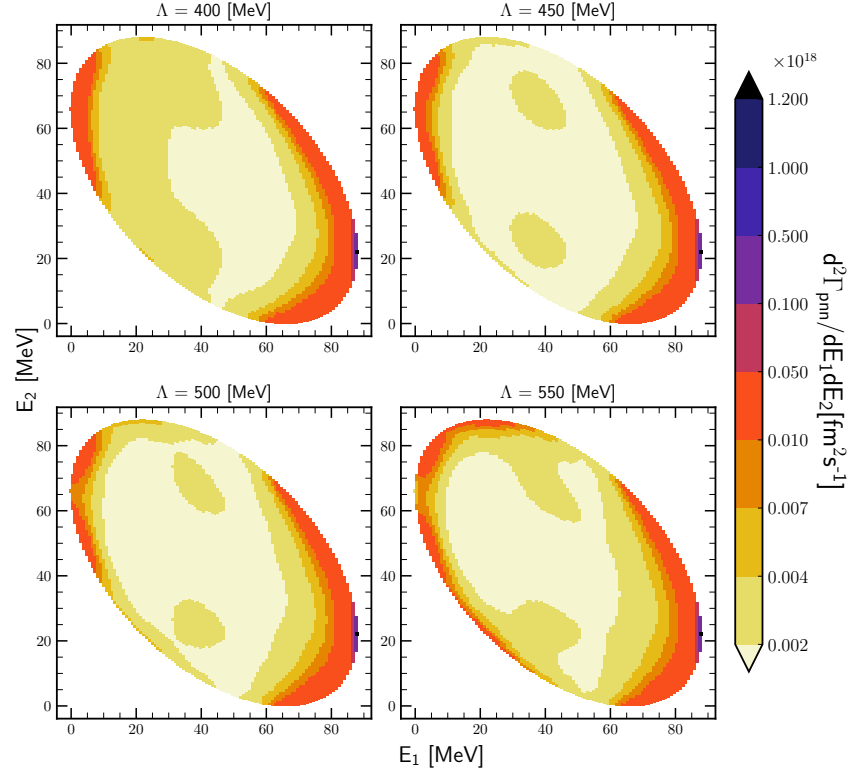


Figure 3.53: Intensity plots for the double differential absorption rates  $d^2\Gamma_{pn}/dE_1 dE_2$  for the  $\pi^- + {}^3\text{He} \rightarrow p + n + n$  process, obtained using the SMS potential at  $\text{N}^4\text{LO}^+$  with SN current only (without 2N). All other contributions are the same as in Fig. 3.49: PWIAS+RESC and 2NF+3NF. Each panel present predictions obtained with different values of the cutoff parameter  $\Lambda$ : from 400 MeV (upper left) to 550 MeV (lower right). Nucleon 1 is a proton.

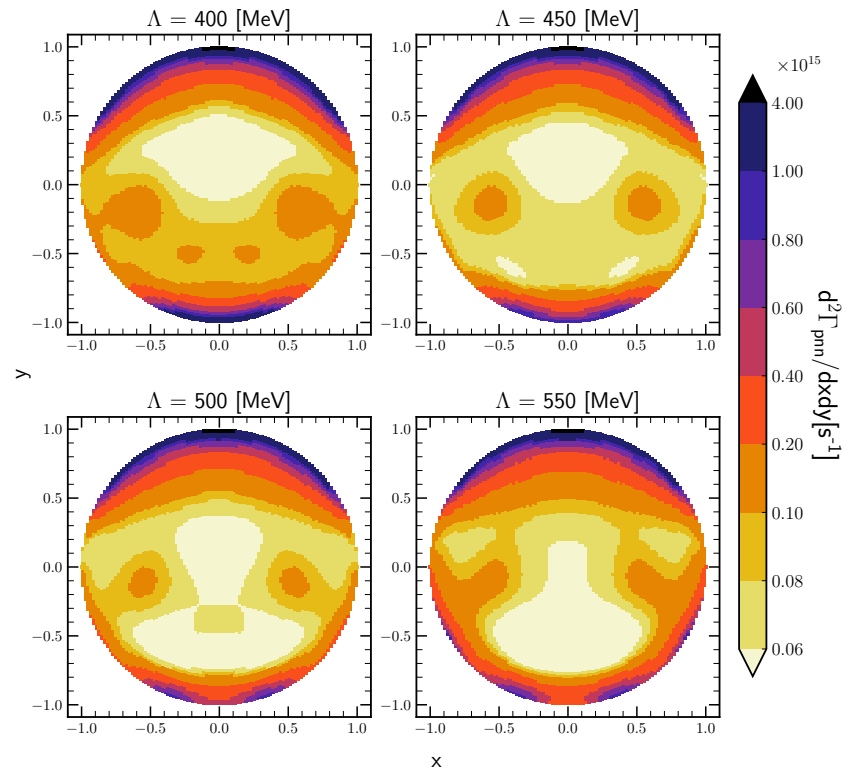


Figure 3.54: The same as in Fig. 3.53 but for the double differential absorption rates  $d^2\Gamma_{pnn}/dx dy$ .

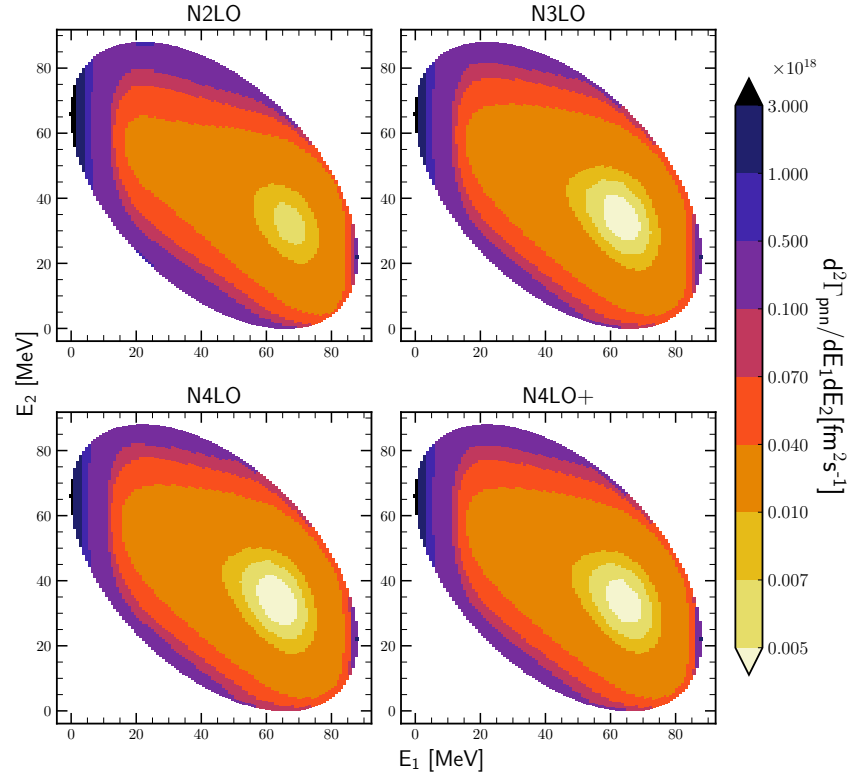


Figure 3.55: Intensity plots for the double differential absorption rates  $d^2\Gamma_{pnn}/dE_1 dE_2$  for the  $\pi^- + {}^3\text{He} \rightarrow p + n + n$  process, obtained using the SMS potential at  $\text{N}^4\text{LO}^+$  with all contributions possible: plane wave + rescattering,  $\text{SN} + 2\text{N}$ ,  $2\text{NF} + 3\text{NF}$ . Each panel present predictions obtained with different chiral orders of the SMS potential: from  $\text{N}^2\text{LO}$  (upper left) to  $\text{N}^4\text{LO}^+$  (lower right) and with  $\Lambda = 450$  MeV. Nucleon 1 is a proton.

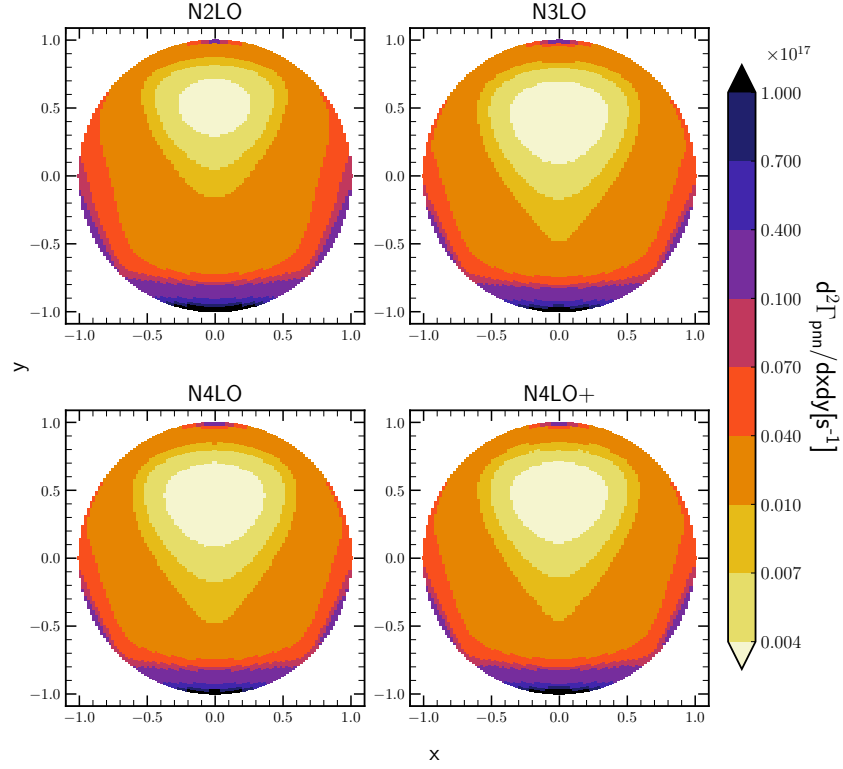


Figure 3.56: The same as in Fig. 3.55 but for the double differential absorption rates  $d^2\Gamma_{pnn}/dx dy$ .

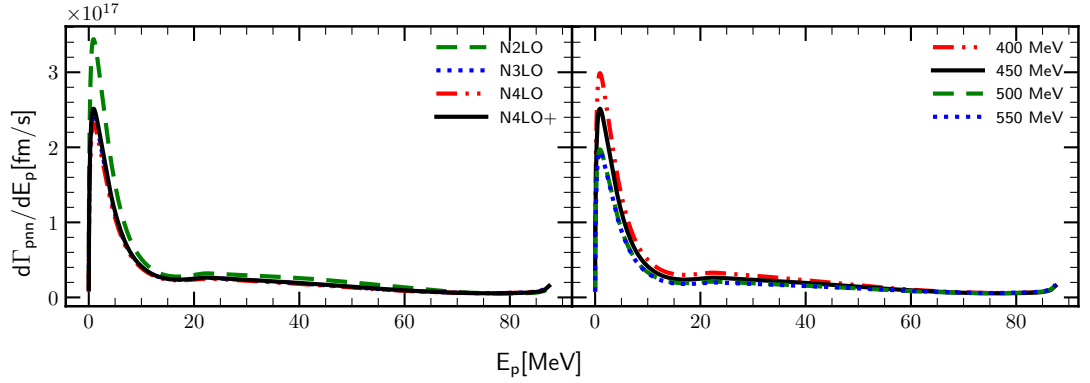


Figure 3.57: Differential absorption rate  $d\Gamma_{pnn}/dE_p$  as a function of the proton energy  $E_p$  for the  $\pi^- + 3\text{He} \rightarrow p + n + n$  process. Left panel shows results obtained with N<sup>2</sup>LO (green dashed line), N<sup>3</sup>LO (blue dotted line), N<sup>4</sup>LO (red dashed-double-dotted line) and N<sup>4</sup>LO<sup>+</sup> (black solid line) chiral orders, and with  $\Lambda = 450$  MeV. The right panel includes results obtained with the N<sup>4</sup>LO<sup>+</sup> SMS potential with different values of the  $\Lambda$ : 400 MeV (red dashed-double-dotted line),  $\Lambda$ : 450 MeV (black solid line),  $\Lambda$ : 500 MeV (green dashed line) and  $\Lambda$ : 550 MeV (blue dotted line). All predictions were obtained with "FULL-(SN+2N)-(2NF+3NF)" setup.

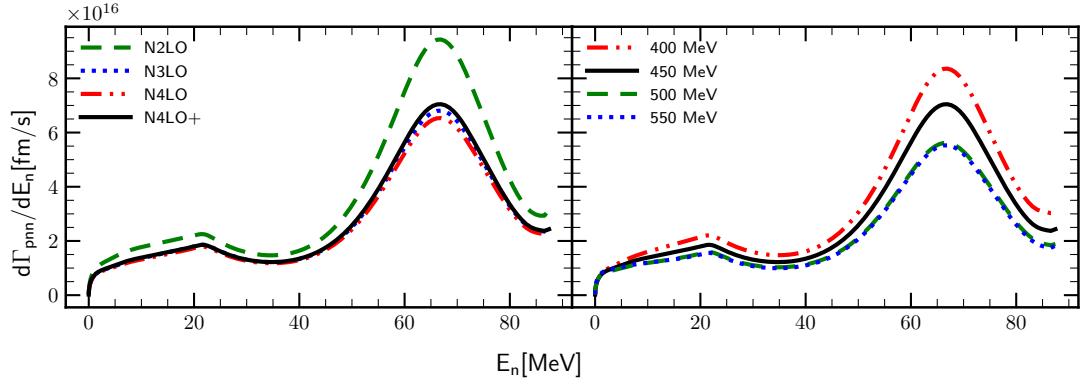


Figure 3.58: The same as in Fig. 3.57 but for the differential absorption rate  $d\Gamma_{pnn}/dE_n$  as a function of the neutron energy  $E_n$ .

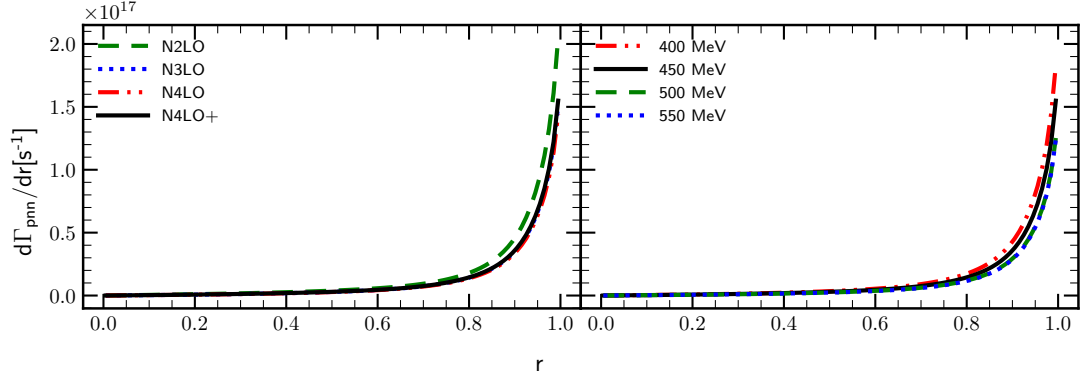


Figure 3.59: The same as in Fig. 3.57 but for the differential absorption rate  $d\Gamma_{pnn}/dr$  as a function of the parameter  $r$  of the Dalitz coordinates:  $r = \sqrt{x^2 + y^2}$ .

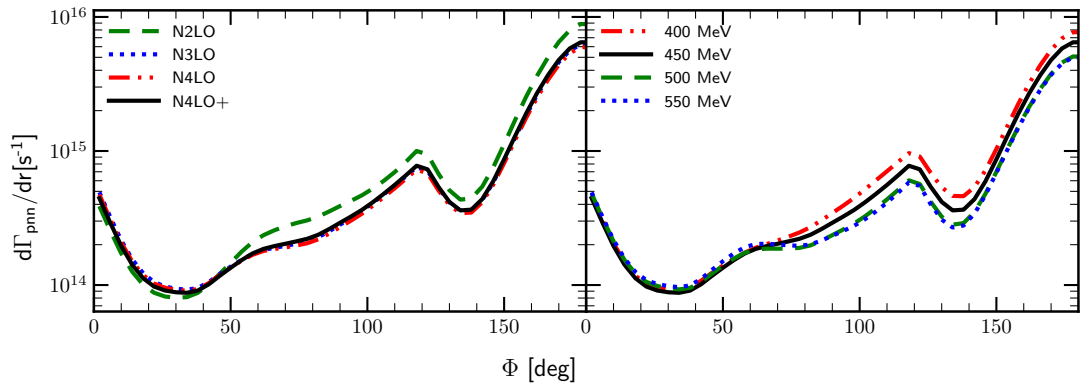


Figure 3.60: The same as in Fig. 3.59 but for the differential absorption rate  $d\Gamma_{pnn}/d\phi$  as a function of the azimuthal angle  $\phi$  of the Dalitz coordinates:  $\phi = \arctan \frac{y}{x}$ .



### 3.4.2 $\pi^- + {}^3\text{H} \rightarrow n + n + n$

In this subsection I will show results of calculations for the  $\pi^- + {}^3\text{H} \rightarrow n + n + n$  process. In this case we have only a three-body breakup as no two-body configuration can be composed out of three neutrons.

The total absorption rate  $\pi^- + {}^3\text{H} \rightarrow n + n + n$  is shown in Fig. 3.61 as a function on the chiral order of the SMS potential while each curve represents different cutoff values used to obtain the prediction. The most advanced configuration was used in this case, namely Plane wave plus rescattering part, both single- and two-nucleon currents and two-nucleon plus three-nucleon forces.

Similarly to the process with  ${}^3\text{He}$ , we see that with each subsequent chiral order predictions become closer to each other, so cutoff dependency gets weaker. Also, the prediction with  $\Lambda = 550\text{ MeV}$  at  $\text{N}^3\text{LO}$  is strangely above the prediction with  $\Lambda = 500\text{ MeV}$ . We can also notice, that at  $\text{N}^4\text{LO}$  predictions with cutoff values  $500\text{ MeV}$  and  $550\text{ MeV}$  are much closer to each other than to other values.

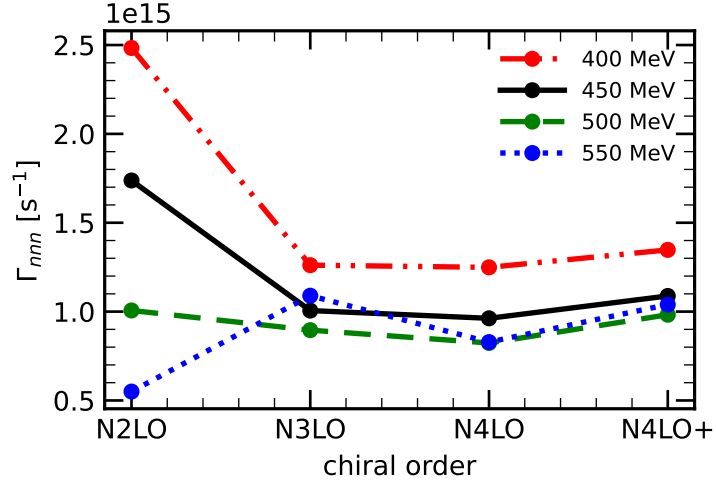


Figure 3.61: Absorption rate for  $\pi^- + {}^3\text{H} \rightarrow n + n + n$  reaction as a function of the chiral order with different values of the cutoff parameter  $\Lambda$ . Predictions were obtained with 3NF.

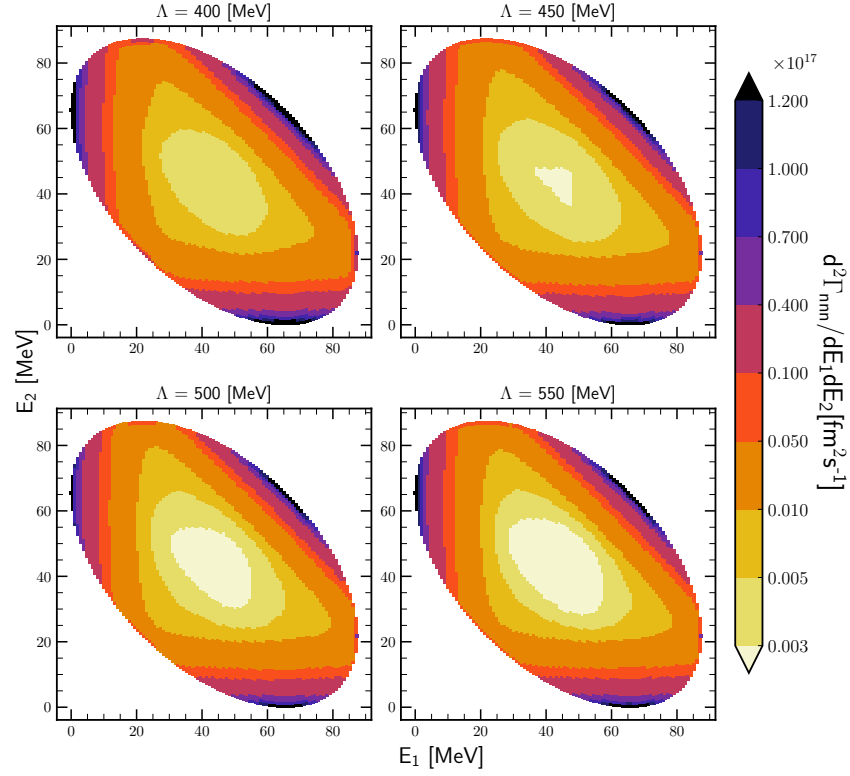


Figure 3.62: Intensity plots for the double differential absorption rates  $d^2\Gamma_{nnn}/dE_1dE_2$  for the  $\pi^- + {}^3\text{H} \rightarrow n + n + n$  process, obtained using the SMS potential at  $\text{N}^4\text{LO}^+$  with all contributions possible: plane wave + rescattering, SN + 2N, 2NF+3NF. Each panel present predictions obtained with different values of the cutoff parameter  $\Lambda$ : from 400 MeV (upper left) to 550 MeV (lower right).

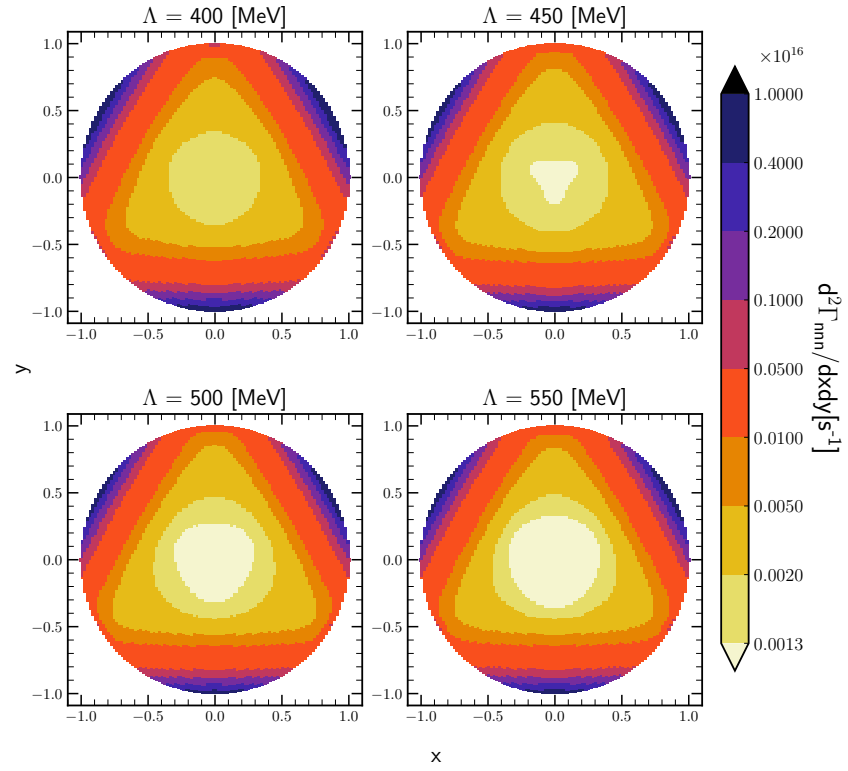


Figure 3.63: The same as in Fig. 3.62 but for the double differential absorption rates  $d^2\Gamma_{nnn}/dx dy$ .

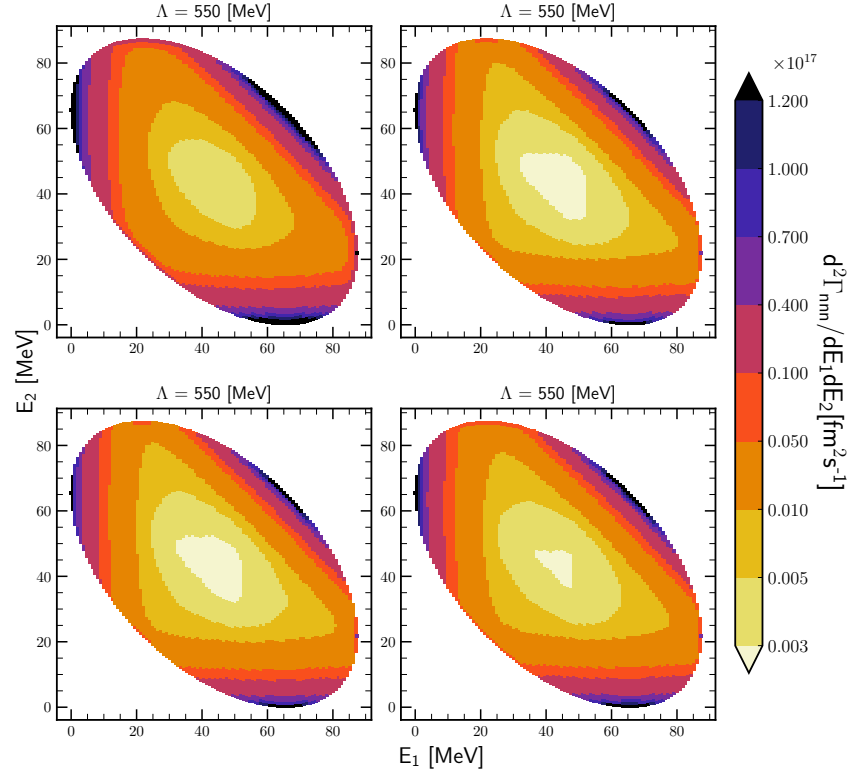


Figure 3.64: Intensity plots for the double differential absorption rates  $d^2\Gamma_{nn}/dE_1 dE_2$  for the  $\pi^- + {}^3\text{H} \rightarrow n + n + n$  process, obtained using the SMS potential at  $\text{N}^4\text{LO}^+$  with all contributions possible: plane wave + rescattering,  $\text{SN} + 2\text{N}$ ,  $2\text{NF} + 3\text{NF}$ . Each panel present predictions obtained with different chiral orders of the SMS potential: from  $\text{N}^2\text{LO}$  (upper left) to  $\text{N}^4\text{LO}^+$  (lower right) and with  $\Lambda = 450$  MeV.

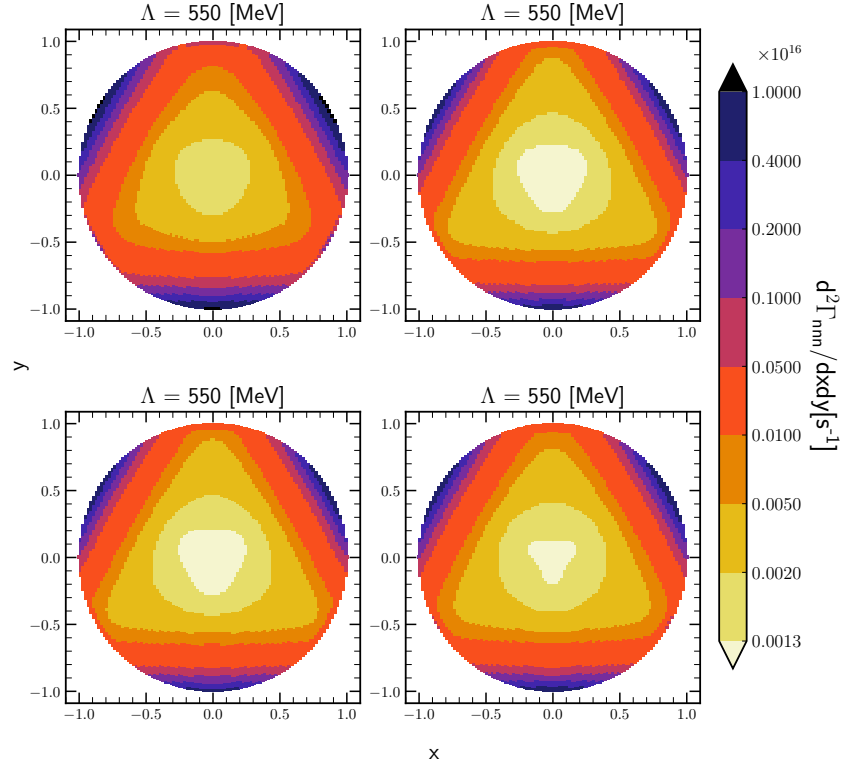


Figure 3.65: The same as in Fig. 3.64 but for the double differential absorption rates  $d^2\Gamma_{nnn}/dx dy$ .

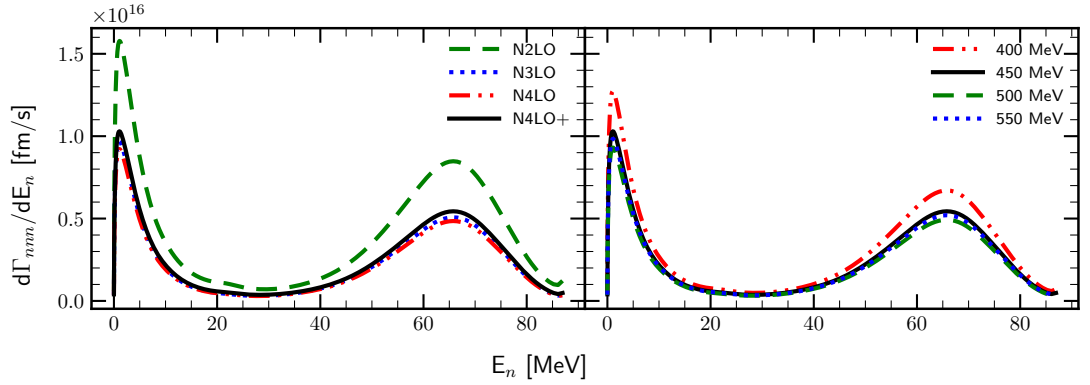


Figure 3.66: Differential absorption rate  $d\Gamma_{nnn}/dE_n$  as a function of the neutron energy  $E_n$  for the  $\pi^- + 3H \rightarrow n + n + n$  process. Left panel shows results obtained with  $N^2\text{LO}$  (green dashed line),  $N^3\text{LO}$  (blue dotted line),  $N^4\text{LO}$  (red dashed-double-dotted line) and  $N^4\text{LO}^+$  (black solid line) chiral orders, and with  $\Lambda = 450$  MeV. The right panel includes results obtained with the  $N^4\text{LO}^+$  SMS potential with different values of the  $\Lambda$ : 400 MeV (red dashed-double-dotted line),  $\Lambda$ : 450 MeV (black solid line),  $\Lambda$ : 500 MeV (green dashed line) and  $\Lambda$ : 550 MeV (blue dotted line). All predictions were obtained with "FULL-(SN+2N)-(2NF+3NF)" setup.

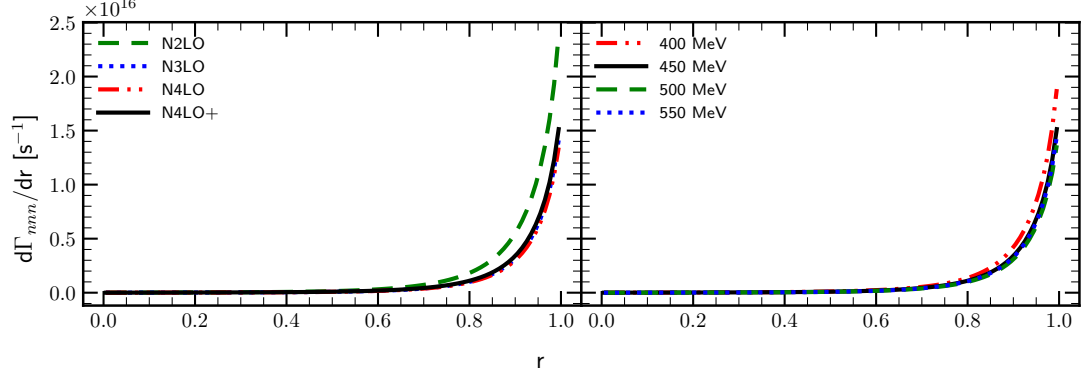


Figure 3.67: The same as in Fig. 3.66 but for the differential absorption rate  $d\Gamma_{nnn}/dr$  as a function of the parameter  $r$  of the Dalitz coordinates:  $r = \sqrt{x^2 + y^2}$ .

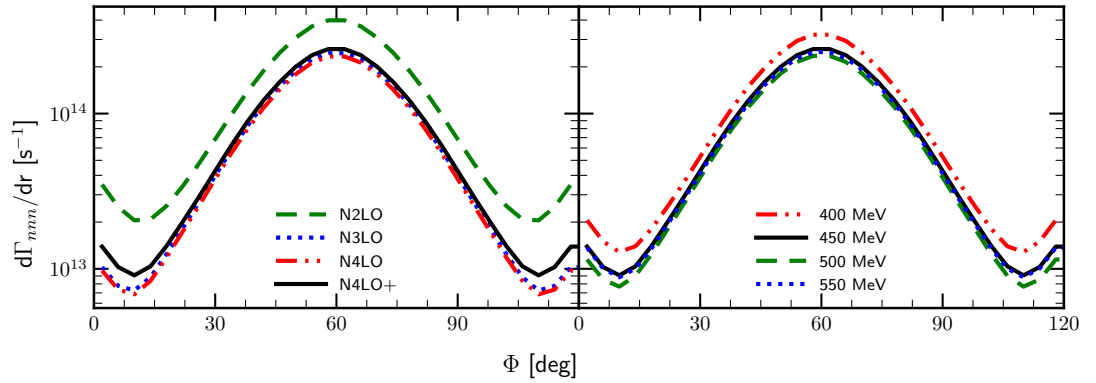


Figure 3.68: The same as in Fig. 3.67 but for the differential absorption rate  $d\Gamma_{nnn}/d\phi$  as a function of the azimuthal angle  $\phi$  of the Dalitz coordinates:  $\phi = \arctan \frac{y}{x}$ .

---

# BIBLIOGRAPHY

- [1] D. M. Skopik, Y. M. Shin, M. C. Phenneger, and J. J. Murphy. Photodisintegration of deuterium determined from the electrodisintegration process. *Phys. Rev. C*, 9:531–536, Feb 1974.
- [2] F. F. Liu, D. E. Lundquist, and B. H. Wiik. Measurements of the polarization of protons from deuteron photodisintegration. *Phys. Rev.*, 165:1478–1482, Jan 1968.
- [3] Reinhold Kose, Bjoern Martin, Rainer Runkel, Helmut Wahlen, and Karl Heinz Kissler. Measurements of the polarization of protons from deuteron photodisintegration for photon energies between 282 and 405 mev. *Zeitschrift für Physik A Hadrons and nuclei*, 220:305–320, 1969.
- [4] T. Kamae, I. Arai, T. Fujii, H. Ikeda, N. Kajiura, S. Kawabata, K. Nakamura, K. Ogawa, H. Takeda, and Y. Watase. Observation of an anomalous structure in proton polarization from deuteron photodisintegration. *Phys. Rev. Lett.*, 38:468–471, Feb 1977.
- [5] Andrew L. Cooper, K. J. Kelly, E. Machado, I. Pogrebnyak, J. Surbrook, C. Tysor, P. Thompson, M. Emamian, B. Walsh, B. Carlin, J. R. Dermigny, A. E. Champagne, and T. B. Clegg. Development of a variable-energy, high-intensity, pulsed-mode ion source for low-energy nuclear astrophysics studies. *Review of Scientific Instruments*, 89(8):083301, 2018.
- [6] A.P. Tonchev, M. Boswell, C.R. Howell, H.J. Karwowski, J.H. Kelley, W. Tornow, and Y.K. Wu. The high intensity  $\gamma$ -ray source (hi $\gamma$ s) and recent results. *Nuclear Instruments and Methods in Physics Research Section B: Beam Interactions with Materials and Atoms*, 241(1):170–175, 2005. The Application of Accelerators in Research and Industry.
- [7] J Bermuth, P Merle, C Carasco, D Baumann, R Böhm, D Bosnar, M Ding, M.O Distler, J Friedrich, J.M Friedrich, J Golak, W Glöckle, M Hauger, W Heil, P Jennewein, J Jourdan, H Kamada, A Klein, M Kohl, B Krusche, K.W Krygier, H Merkel, U Müller, R Neuhausen, A Nogga, Ch Normand, E Otten, Th Pospischil, M Potokar, D Rohe, H Schmieden, J Schmiedeskamp, M Seimetz, I Sick, S Širca, R Skibiński, G Testa, Th Walcher, G Warren, M Weis, H Witała, H Wöhrle, and M Zeier. The

- neutron charge form factor and target analyzing powers from  $^3\text{He}(e\rightarrow,e'n)$  scattering. *Physics Letters B*, 564(3):199–204, 2003.
- [8] D. L. Groep, M. F. van Batenburg, Th. S. Bauer, H. P. Blok, D. J. Boersma, E. Cisbani, R. De Leo, S. Frullani, F. Garibaldi, W. Glöckle, J. Golak, P. Heimberg, W. H. A. Hesselink, M. Iodice, D. G. Ireland, E. Jans, H. Kamada, L. Lapikás, G. J. Lolos, C. J. G. Onderwater, R. Perrino, A. Scott, R. Starink, M. F. M. Steenbakkens, G. M. Urciuoli, H. de Vries, L. B. Weinstein, and H. Witała. Investigation of the exclusive  $^3\text{He}(e,e'pp)n$  reaction. *Phys. Rev. C*, 63:014005, Dec 2000.
  - [9] B.L. Ioffe. QCD (quantum chromodynamics) at low energies. *Progress in Particle and Nuclear Physics*, 56(1):232–277, 2006.
  - [10] S.R. Beane, W. Detmold, K. Orginos, and M.J. Savage. Nuclear physics from lattice qcd. *Progress in Particle and Nuclear Physics*, 66(1):1–40, 2011.
  - [11] R. Machleidt and D. R. Entem. Chiral effective field theory and nuclear forces. *Phys. Rept.*, 503:1–75, 2011.
  - [12] W. Glöckle. Effects of the two-pion exchange three-nucleon force in the triton and  $^3\text{He}$ . *Nuclear Physics A*, 381(3):343–364, 1982.
  - [13] A. Nogga, H. Kamada, W. Glöckle, and B. R. Barrett. The  $\alpha$  particle based on modern nuclear forces. *Phys. Rev. C*, 65:054003, May 2002.
  - [14] S.A. Coon, M.D. Scadron, P.C. McNamee, B.R. Barrett, D.W.E. Blatt, and B.H.J. McKellar. The two-pion-exchange three-nucleon potential and nuclear matter. *Nuclear Physics A*, 317(1):242–278, 1979.
  - [15] B. S. Pudliner, V. R. Pandharipande, J. Carlson, Steven C. Pieper, and R. B. Wiringa. Quantum monte carlo calculations of nuclei with  $A < \sim 197$ . *Phys. Rev. C*, 56:1720–1750, Oct 1997.
  - [16] V. G. J. Stoks, R. A. M. Klomp, C. P. F. Terheggen, and J. J. de Swart. Construction of high-quality nn potential models. *Phys. Rev. C*, 49:2950–2962, Jun 1994.
  - [17] Robert B. Wiringa, V. G. J. Stoks, and R. Schiavilla. An Accurate nucleon-nucleon potential with charge independence breaking. *Phys. Rev.*, C51:38–51, 1995.
  - [18] A. Nogga, H. Kamada, and W. Glöckle. Modern nuclear force predictions for the  $\alpha$  particle. *Phys. Rev. Lett.*, 85:944–947, Jul 2000.
  - [19] H Arenhövel and M. Sanzone. Photodisintegration of the deuteron: A Review of theory and experiment. *Few Body Syst. Suppl.*, 3:1–183, 1991.
  - [20] V. G. J. Stoks, R. A. M. Klomp, M. C. M. Rentmeester, and J. J. de Swart. Partial-wave analysis of all nucleon-nucleon scattering data below 350 MeV. *Phys. Rev. C*, 48:792–815, Aug 1993.
  - [21] S. Weinberg. Nuclear forces from chiral lagrangians. *Physics Letters B*, 251(2):288–292, 1990.
  - [22] S. Weinberg. Effective chiral lagrangians for nucleon-pion interactions and nuclear forces. *Nuclear Physics B*, 363(1):3–18, 1991.



- [23] E. Epelbaum, W. Glöckle, and U.-G. Meißner. Improving the convergence of the chiral expansion for nuclear forces - i: Peripheral phases. *The European Physical Journal A*, 19(1):125–137, January 2004.
- [24] P. Reinert, H. Krebs, and E. Epelbaum. Semilocal momentum-space regularized chiral two-nucleon potentials up to fifth order. *Eur. Phys. J.*, A54(5):86, 2018.
- [25] E. Epelbaum. Few-nucleon forces and systems in chiral effective field theory. *Progress in Particle and Nuclear Physics*, 57(2):654–741, 2006.
- [26] D. R. Entem, R. Machleidt, and Y. Nosyk. High-quality two-nucleon potentials up to fifth order of the chiral expansion. *Phys. Rev. C*, 96:024004, Aug 2017.
- [27] E. Epelbaum, W. Glöckle, and Ulf-G. Meißner. Nuclear forces from chiral lagrangians using the method of unitary transformation (i): Formalism. *Nuclear Physics A*, 637(1):107–134, 1998.
- [28] E. Epelbaum, W. Glöckle, and U. G. Meißner. The two-nucleon system: Nuclear forces from chiral lagrangians using the method of unitary transformation ii. *Nucl. Phys. A*, 671:295–331, 2000.
- [29] Evgeny Epelbaum, Walter Glöckle, and Ulf-G Meißner. The two-nucleon system at next-to-next-to-next-to-leading order. *Nuclear Physics A*, 747(2-4):362–424, 2005.
- [30] E. Epelbaum, H. Krebs, and U. G. Meißner. Precision nucleon-nucleon potential at fifth order in the chiral expansion. *Phys. Rev. Lett.*, 115(12):122301, 2015.
- [31] D. R. Entem and R. Machleidt. Accurate charge-dependent nucleon-nucleon potential at fourth order of chiral perturbation theory. *Phys. Rev. C*, 68:041001, Oct 2003.
- [32] R. Machleidt and D. R. Entem. Towards a consistent approach to nuclear structure: EFT of two- and many-body forces. *Journal of Physics G: Nuclear and Particle Physics*, 31(8):S1235–S1244, July 2005.
- [33] R. Machleidt, P. Liu, D. R. Entem, and E. Ruiz Arriola. Renormalization of the leading-order chiral nucleon-nucleon interaction and bulk properties of nuclear matter. *Phys. Rev. C*, 81:024001, Feb 2010.
- [34] M. Piarulli, L. Girlanda, L. E. Marcucci, S. Pastore, R. Schiavilla, and M. Viviani. Electromagnetic structure of  $A = 2$  and 3 nuclei in chiral effective field theory. *Phys. Rev.*, C87(1):014006, 2013.
- [35] M. Piarulli, L. Girlanda, R. Schiavilla, R. Navarro Pérez, J. E. Amaro, and E. Ruiz Arriola. Minimally nonlocal nucleon-nucleon potentials with chiral two-pion exchange including  $\Delta$  resonances. *Phys. Rev. C*, 91:024003, Feb 2015.
- [36] J. Golak, R. Skibiński, H. Witała, K. Topolnicki, A. E. Elmesheeb, H. Kamada, A. Nogga, and L. E. Marcucci. Break-up channels in muon capture on  $^3\text{He}$ . *Phys. Rev.*, C90(2):024001, 2014. [Addendum: *Phys. Rev. C*90,no.2,029904(2014)].
- [37] J. Golak, H. Kamada, H. Witała, Walter Glöckle, J. Kuroś, R. Skibiński, V. V. Kotlyar, K. Sagara, and H. Akiyoshi. Faddeev calculations of proton deuteron radiative capture with exchange currents. *Phys. Rev.*, C62:054005, 2000.

- [38] J. Golak, R. Skibiński, H. Witała, W. Glöckle, A. Nogga, and H. Kamada. Electron and photon scattering on three-nucleon bound states. *Phys. Rept.*, 415:89–205, 2005.
- [39] C.G.J. Jacobi. Ueber gauss neue methode, die werthe der integrale näherungsweise zu finden. 1826.
- [40] C. Van Der Leun and C. Alderliesten. The deuteron binding energy. *Nuclear Physics A*, 380(2):261–269, 1982.
- [41] E Epelbaum, H Krebs, and Ulf-G Meißner. Precision nucleon-nucleon potential at fifth order in the chiral expansion. *Phys. Rev. Lett.*, 115(12):122301, 2015.
- [42] E Epelbaum, H Krebs, and U-G Meißner. Improved chiral nucleon-nucleon potential up to next-to-next-to-next-to-leading order. *Eur. Phys. J. A*, 51(5), May 2015.
- [43] S. Binder, A. Calci, E. Epelbaum, R. J. Furnstahl, J. Golak, K. Hebeler, H. Kamada, H. Krebs, J. Langhammer, S. Liebig, P. Maris, Ulf-G. Meißner, D. Minossi, A. Nogga, H. Potter, R. Roth, R. Skibiński, K. Topolnicki, J. P. Vary, and H. Witała and. Few-nucleon systems with state-of-the-art chiral nucleon-nucleon forces. *Phys. Rev.*, C93(4):044002, 2016.
- [44] Evgeny Epelbaum. High-precision nuclear forces : Where do we stand? *PoS*, CD2018:006, 2020.
- [45] S. B. S. Miller, A. Ekström, and C. Forssén. Posterior predictive distributions of neutron-deuteron cross sections, 2022.
- [46] J. A. Melendez, S. Wesolowski, and R. J. Furnstahl. Bayesian truncation errors in chiral effective field theory: Nucleon-nucleon observables. *Phys. Rev. C*, 96:024003, Aug 2017.
- [47] M. Bosman, A. Bol, J.F. Gilot, P. Leleux, P. Lipnik, and P. Macq. Measurement of the total cross section for the  $^1\text{H}(n, \gamma) ^2\text{H}$  reaction between 37 and 72 mev. *Physics Letters B*, 82(2):212–215, 1979.
- [48] J. Arends, H.J. Gassen, A. Hegerath, B. Mecking, G. Nöldeke, P. Prenzel, T. Reichelt, A. Voswinkel, and W.W. Sapp. Experimental investigation of deuteron photodisintegration in the  $\delta$ -resonance region. *Nuclear Physics A*, 412(3):509–522, 1984.
- [49] R. Moreh, T. J. Kennett, and W. V. Prestwich.  $^2\text{H}(\gamma, n)$  absolute cross section at 2754 kev. *Phys. Rev. C*, 39:1247–1250, Apr 1989.
- [50] Y. Birenbaum, S. Kahane, and R. Moreh. Absolute cross section for the photodisintegration of deuterium. *Phys. Rev. C*, 32:1825–1829, Dec 1985.
- [51] R. Bernabei, A. Incicchitti, M. Mattioli, P. Picozza, D. Prosperi, L. Casano, S. d’Angelo, M. P. De Pascale, C. Schaerf, G. Giordano, G. Matone, S. Frullani, and B. Girolami. Total cross section for deuteron photodisintegration between 15 and 75 mev. *Phys. Rev. Lett.*, 57:1542–1545, Sep 1986.
- [52] I. A. Rachek, L. M. Barkov, S. L. Belostotsky, V. F. Dmitriev, M. V. Dyug, R. Gilman, R. J. Holt, B. A. Lazarenko, S. I. Mishnev, V. V. Nelyubin, D. M. Nikolenko, A. V. Osipov, D. H. Potterveld, R. Sh. Sadykov, Yu. V. Shestakov, V. N.

- Stibunov, D. K. Toporkov, H. de Vries, and S. A. Zevakov. Measurement of tensor analyzing powers in deuteron photodisintegration. *Phys. Rev. Lett.*, 98:182303, May 2007.
- [53] S. Q. Ying, E. M. Henley, and G. A. Miller. Deuteron photodisintegration. *Phys. Rev.*, C38:1584–1600, 1988. and references therein.
- [54] E. de Sanctis et al. Deuteron Photodisintegration Cross-section Between 100-MeV and 220-MeV. *Phys. Rev. Lett.*, 54:1639, 1985.
- [55] S.I. Mishnev, D.M. Nikolenko, S.G. Popov, I.A. Rachev, A.B. Temnykh, D.K. Toporkov, E.P. Tsentalovich, B.B. Wojtsekhowski, S.L. Belostotsky, V.V. Nelyubin, V.V. Sulimov, and V.N. Stibunov. Measurement of the analyzing power components in photodisintegration of the polarized deuteron. *Physics Letters B*, 302(1):23–28, 1993.
- [56] K M Schmitt and H Arenhövel. Deuteron photodisintegration with the bonn OBE potentials. *Few-body syst.*, 7(3):95–117, 1989.
- [57] K.-H. Krause, J. Sobolewski, J. Ahrens, J.M. Henneberg, and B. Ziegler. Photodisintegration of the deuteron by linearly polarized photons. *Nuclear Physics A*, 549(3):387–406, 1992.
- [58] M. P. De Pascale, G. Giordano, G. Matone, D. Babusci, R. Bernabei, O. M. Bilaniuk, L. Casano, S. d’Angelo, M. Mattioli, P. Picozza, D. Prosperi, C. Schaerf, S. Frullani, and B. Girolami. Polarization asymmetry in the photodisintegration of the deuteron. *Phys. Rev. C*, 32:1830–1841, Dec 1985.
- [59] V P Barannik, V G Gorbenko, V A Gushchin, Y V Zhebrovskii, L Y Kolesnikov, Y V Kulish, A L Rubashkin, and P V Sorokin. Study of the cross-section asymmetry in photodisintegration of the deuteron by polarized. gamma. rays at low energies. *Sov. J. Nucl. Phys. (Engl. Transl.); (United States)*, 38:5, 11 1983.
- [60] I E Vnukov, I V Glavanakov, Y F Krechetov, A P Potylitsyn, G A Saruev, V N Stibunov, and A N Tabachenko. Photodisintegration of the deuteron by linearly polarized photons below the pion-production threshold. *Sov. J. Nucl. Phys. (Engl. Transl.); (United States)*, 47:4, 4 1988.
- [61] W. Del Bianco, L. Federici, G. Giordano, G. Matone, G. Pasquariello, P. Picozza, R. Caloi, L. Casano, M. P. De Pascale, L. Ingrosso, M. Mattioli, E. Poldi, C. Schaerf, P. Pelfer, D. Prosperi, S. Frullani, B. Girolami, and H. Jeremie. Neutron asymmetry measurements in the deuteron photodisintegration between 10 and 70 mev. *Phys. Rev. Lett.*, 47:1118–1120, Oct 1981.
- [62] R. W. Jewell, W. John, J. E. Sherwood, and D. H. White. Polarization of photoneutrons produced from deuterium by 2.75-mev gamma rays. *Phys. Rev.*, 139:B71–B79, Jul 1965.
- [63] J.M. Cameron, C.A. Davis, H. Fielding, P. Kitching, J. Pasos, J. Soukup, J. Uegaki, J. Wesick, H.S. Wilson, R. Abegg, D.A. Hutcheon, C.A. Miller, A.W. Stetz, and I.J. van Heerden. Radiative capture of polarized neutrons by hydrogen below the pion production threshold. *Nuclear Physics A*, 458(4):637–651, 1986.